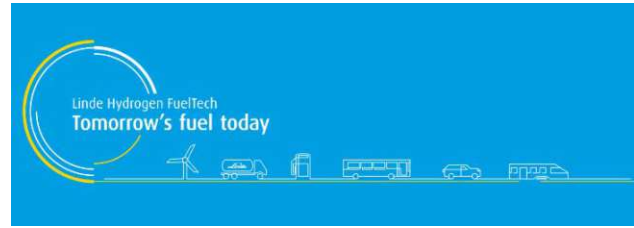




TECHNISCHE
UNIVERSITÄT
WIEN
Vienna | Austria



Master Thesis

Simulation of a Hydrogen Fueling Process

carried out for the purpose of obtaining the academic degree

Diplom-Ingenieur (Dipl.-Ing. or DI),

submitted at TU Wien,

Faculty of Mechanical and Industrial Engineering,

by

Lukas Heinzl, B.Sc.

Matr.-Nr.: 00771132

in collaboration with the

Institute of Energy Systems and Thermodynamics

and

Linde Hydrogen FuelTech GmbH

supervised by

Ao. Univ.Prof. Dipl.-Ing. Dr. techn. Andreas Werner

Sascha Dorner

Vienna, April 23, 2020

Affidavit

I confirm that going to press of this thesis needs the confirmation of the examination committee.

I, Lukas Heinzl, declare in lieu of oath

1. that I wrote this thesis and performed the associated research myself, using only literature cited in this volume. If text passages from sources are used literally, they are marked as such.
2. that this work is original and has not been submitted elsewhere for any examination nor is it currently under consideration for a thesis elsewhere.

Vienna, 23.04.2020

Lukas Heinzl

Abstract

Gaseous hydrogen is one of several alternatives to fossil-based vehicle fuels. In order to establish hydrogen as a competitive alternative, the price-performance ratio of already commercially available hydrogen refueling stations has to improve. At the same time, the customer's further demands, such as convenient overall fueling time or flawless operational behavior, have to be met as well.

Within the scope of this work, a simulation tool is created in MatLab-Simulink. A representative model of the plant is constructed in support of Simscape, an extension of Simulink, and its "gas domain" block components.

The thermodynamic model, once executed, is able to predict a fueling station's performance, which operates in accordance to SAE J2601. The resulting simulation data shall provide information on the plant's overall thermodynamic behavior and its current weak points.

An elaborate overview on basic fueling procedures and technologies is provided in the introductory chapters. The approach of building the model, its functioning and the workflow of the simulation environment are exemplified within the subsequent chapter.

For testing the tool in its overall performance, two representative standard fueling scenarios are simulated. The plotted trends of various thermodynamic fueling parameters then serve as the material for subsequent analysis and discussion. Hence, a major finding is the heat exchanger's improvable thermal conductivity between the "cooling source" and its aluminium layer.

Additionally, two realistic cases of disturbance during operation are mimicked. The corresponding results offer suitable starting points for finding further room of improvement for the simulation tool, and also the superior plant design as well.

Kurzfassung

Gasförmig gespeicherter Wasserstoff ist eine von vielen zukunftssträchtigen Alternativen zu fossilen Fahrzeug-Treibstoffen. Um Wasserstoff als einen kompetitiven Treibstoff zu etablieren, muss das Preis-Leistungsverhältnis von bereits verfügbaren Wasserstoff-Tankstellen verbessert werden. Gleichzeitig dazu müssen auch zeitgemäße Forderungen des Fahrzeuglenkers, wie z.B. kurze Gesamtbetankungszeiten oder ein einwandfreies Betriebsverhalten der Tankstelle, erfüllt werden.

Im Rahmen dieser Arbeit wird ein Simulationstool in MatLab-Simulink® programmiert. Ein Modell einer vorliegenden, bereits international eingesetzten Betankungsanlage wird mithilfe von Simscape – einer Erweiterung von Simulink – und in Simscape verfügbaren „Gas Domain“-Blockkomponenten erstellt.

Das finalisierte und von einem Rechner ausführbare Simulink-Modell ermöglicht Vorhersagen über das Betriebsverhalten der Betankungsanlage, welche auf Basis der internationalen Betankungsnorm SAE J2601 betankt. Die resultierenden Simulationsergebnisse sollen umfassende Aufschlüsse über das thermodynamische Verhalten die aktuellen Schwachpunkte der vorliegenden Anlage ermöglichen.

Ein ausführlicher Überblick über die grundlegenden Betankungsverfahren und Betankungstechnologien wird in den einführenden Kapiteln dargeboten. Die Herangehensweise zur Modellentwicklung, die Arbeitsweise des Modells und der Workflow der Simulationsumgebung MatLab-Simulink® werden in den darauffolgenden Kapiteln erläutert.

Zum Testen der erwarteten Funktionstüchtigkeit des Simulationstools werden zwei repräsentative Standard-Betankungsszenarien simuliert. Die resultierenden Profile verschiedener thermodynamischer Parameter dienen folglich als Daten-Ausgangsmaterial für eine Diskussion und Analyse der Simulationsergebnisse. Eine daraus gewonnene, zentrale Erkenntnis ist die verfeinerbare Wärmeleitfähigkeit des Wärmetauscher-Elementes zwischen der Kühlquelle-Blockkomponente und der Aluminium-Masse.

Zusätzlich wurden zwei realistische Anlagen-Störfälle nachgeahmt. Die entsprechenden Simulationsergebnisse ergeben einen Ausgangspunkt an Daten und Erkenntnissen für mögliche Verbesserungen des Tools, als auch die übergeordnete Anlagenkonzeption.

Acknowledgements

First and foremost, I want to thank my family for the boundless support I was privileged to receive over the entire course of my studies. May it be in form of innumerable encouragements or freeing up the financial and spatial resources to be able to immerse myself fully into the content of my studies - my gratitude to what I've been able to learn and experience through my family's support is unmeasurable.

My special acknowledgements are preserved for my master thesis supervisor, Andreas Werner. Through the course of six months of intensive research time at Linde Hydrogen FuelTech GmbH, I was privileged to experience Andreas' professional expertise and invaluable personal guidance.

Also I would like to give my special acknowledgement to Sascha Dorner, my project supervisor within the R&D department of Linde Hydrogen FuelTech GmbH. My aspiration to conduct an industrial master thesis on hydrogen applications could be realized by Sascha's readiness to supervise me as a full member of the R&D team over the course of six months.

Furthermore, I want to thank the countless colleagues at Linde for their high level of supportiveness, invaluable and innumerable minutes of advice, as well as their encouraging words and personal advice.

Formula symbols and abbreviations

Latin formula symbols

A	area	m^2
C	sonic conductance	-
c_v	specific heat capacity at constant volume	$J/(kg \cdot K)$
C_v	flow coefficient	$m^3/(hr \cdot kPa)$
c_p	specific heat capacity at constant pressure	$J/(kg \cdot K)$
D_h	hydraulic diameter	m
d_i	definitive length of a body	m
E	energy	J
E_{kin}	kinetic energy	J
E_{pot}	potential energy	J
F	Helmholtz free energy	J
f_{Darcy}	Darcy friction factor	-
f_{shape}	shape factor for laminar flow viscous friction	-
G	Gibbs free energy	J
g	gravitational acceleration	m/s^2
H	enthalpy	J
h	Heat transfer coefficient	$W/(m^2 \cdot K)$
h	Specific enthalpy	J/kg
k	thermal conductivity coefficient	$W/(m \cdot K)$
L_{eqv}	aggregate equivalent length of local resistances	-
m	mass	kg
n	amount of substance	mol
p	pressure	MPa
p	momentum	$kg/(m \cdot s)$
Q	heat	J
\dot{Q}	heat flow rate	W
Q	volumetric flow rate	m^3/s
\dot{q}	heat flux	W/m^2
R	ideal gas constant	$J/(kg \cdot K)$
S	entropy	J/K
S	cross-sectional area of a pipe	m^2
t	surface tension	N/m
T	absolute temperature	K
U	internal energy	J
U	thermal transmittance	$W/(m^2 \cdot K)$
u	specific internal energy	J/kg
\dot{V}	volumetric flow rate	m^3/s
v	specific volume	m^3/kg
W	mechanical work	J
W_{diss}	dissipated mechanical work	J
w	velocity	m/s

x,y,z	coordinates of the Cartesian coordinate system	-
Z	compressibility factor	-
z	height	m

Greek formula symbols

α	heat transfer coefficient	W/(m ² *K)
μ_T	Joule-Thomson-coefficient	K/bar
λ	thermal conductivity coefficient	W/(m*K)
μ	dynamic viscosity	kg/(m*s)
ν	kinematic viscosity	m ² /s
ρ	density	kg/m ³
ξ_{Darcy}	Darcy friction factor	-

Acronyms

ACF	aluminium cold fill unit
APRR	average pressure ramp rate
CcH ₂	cryo-compressed hydrogen
CHSS	compressed hydrogen storage system
CGH ₂	compressed gaseous hydrogen
FCEV	fuel cell electric vehicle
GUI	graphical user interface
LH ₂	liquid cryogenic hydrogen
MOP	maximum operating pressure
NWP	nominal working pressure
SAE	Society of Automotive Engineers
SOC	state of charge

Contents

AFFIDAVIT	I
ABSTRACT	I
KURZFASSUNG	III
ACKNOWLEDGEMENTS	IV
FORMULA SYMBOLS AND ABBREVIATIONS	V
CONTENTS	VII
1. THEMATIC CLASSIFICATION	1
1.1 Motivation	1
1.1.1 Population growth, Power demand & resources	1
1.1.2 Climate change, greenhouse effect, emissions	2
1.1.3 Starting points for a hydrogen economy	4
1.2 Aim of work	6
1.2.1 Aims	6
1.2.2 Procedure	8
1.3 Hydrogen as an energy carrier	9
1.3.1 Production	9
1.3.2 Storage	12
3.1.3. Transport	15
2. THERMODYNAMICS	17
2.1 Balance equations	17
2.2 Fundamental thermodynamic relation	17
2.2.1 Equations of state	20
2.2.1.1 Thermal equations of state	20
2.2.1.2 Caloric equation of state	21
2.2.2 Conservation equations	26
2.2.2.1 Mass balance	26
2.2.2.2 Energy balance	26
2.2.2.3 Momentum balance	28
2.3 Fluid mechanics	29
2.4 Heat transfer correlations	33

3. BASIC FUELING PROCEDURES & TECHNOLOGIES	37
3.1 Procedures of fueling	37
3.1.1 Fueling station designs	37
3.1.2 Hydrogen fueling protocols	39
3.1.2.1 Non-communication method	41
3.1.2.2 Communication method	43
3.1.3 Thermodynamics aspects & stop criteria	44
3.1.4 Cascade tank switching	45
3.1.5 Cryotechnology	47
4. MODEL DESCRIPTION	49
4.1 Possibilities of MatLab, Simulink and Simscape	50
4.2. Thermodynamic properties library	51
4.3 Structure of the model	52
4.3.1 Gas flow unit	55
4.3.2 Heat transfer unit	58
4.4 Control unit	60
4.4 Tank switching mechanism unit	62
4.5 Workflow of the simulation	66
4.5.1 Model settings and configurations before simulation start	66
4.5.2 Choice of solver	67
4.5.3 Executing the simulation	68
5. SIMULATION RESULTS	71
5.1 Parameter study	71
5.1.1 Scenario 1	72
5.1.2 Scenario 2	84
5.1.3 State of Charge	94
5.2 Scenario variations	95
5.2.1 Case 1: Outage of Heat Exchanger	95
5.2.2 Case 2: Changing the controller's control parameters	99
6. CONCLUSIONS AND FURTHER WORK	102
6.1 Further work	102
REFERENCES	104
LIST OF FIGURES	108
LIST OF TABLES	111

1. Thematic classification

1.1 Motivation

1.1.1 Population growth, Power demand & resources

As the earth's population has been growing with an annual growth rate between 1 and 2 percent since 1955, so will an obviously inexhaustible progress in technology and medicine, among many other factors, continue the human population growth. [1] Simultaneously with thoroughly positive global developments, such as an improvement in medical standards, overall literacy or an overarching growth in prosperity comes along a great many of environmental and economic challenges. Every human's growing prosperity still needs a growing supply of resources. The global primary energy demand remains covered around 80 to 85 percent through fossil energy carriers since 2014, thereof around 30% mineral oil, 30% coal, 20% natural gas, 5% nuclear power and 15% renewables. [2] Since all fossil resources will reach an unpredictable end in its exploitability, a transition to mostly regenerative resources, such as solar energy, wind energy or hydropower will provide a key global challenge for the next decades. A continuously resilient effort of research and the demand after technological innovation has led to an expansion of possibilities to generate sustainable sources of secondary energy. With solar, wind and hydrogen power technologies leading the way to generate electricity, hydrogen, in its gaseous and liquid form, has become a promising possibility to store excessive electricity, produced through renewables.

In 2014, the global breakdown of secondary energy carriers has been 67% fossil energy carriers, thereof 40% crude oil products, 15% natural gas and 12% coal, 15% renewable energy carriers – mainly biomass – and 18% electrical power. [3] As visible in figure 2, both the total consumption of renewable energy carriers and non-regenerative energy carriers grow in comparable speed.

TOTAL 2014: 9425 Mtoe

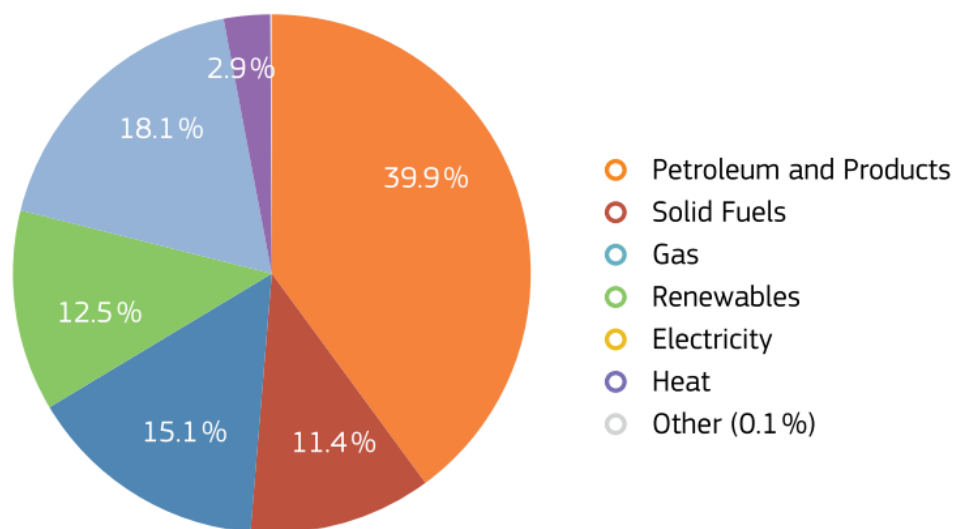


Figure 1: Global secondary energy carriers' stakes in 2014 in Mtoe [3]

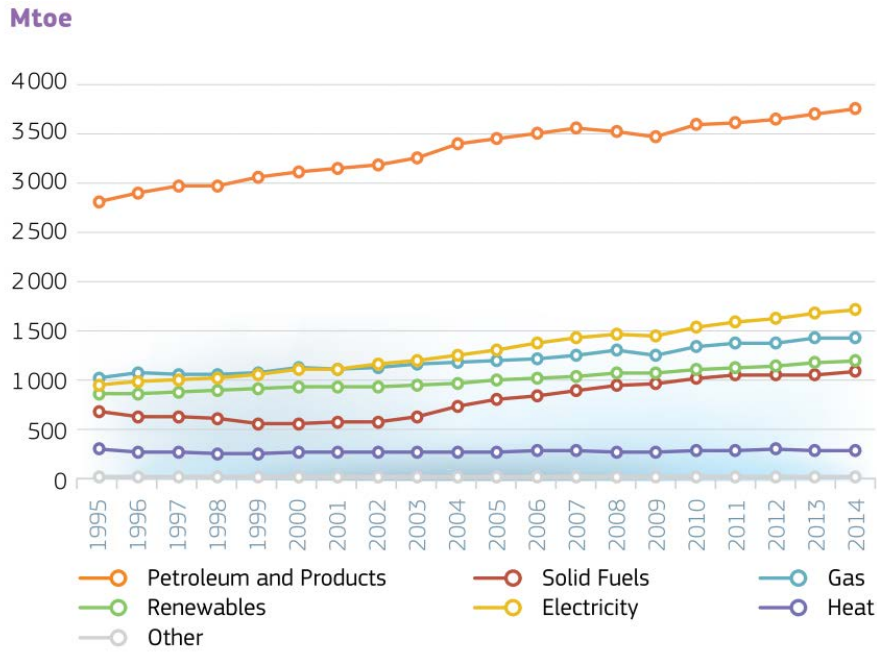


Figure 2: Global secondary energy consumption between 1995 and 2014 in Mtoe [3]

At present, hydrogen has less than 1% share in the global offer of secondary energy. An argument for this circumstance could be that the currently offered technologies for storing and converting hydrogen into electricity are still in its initial phase of becoming acquainted as both reliable and accessible technologies.

1.1.2 Climate change, greenhouse effect, emissions

The concept of overall sustainable development has evolved into a guiding principle of a livable future world where human needs are met while keeping balance with nature. The emergence of a self-improving sustainable global energy system is a gradual long-term process that requires a far-reaching transformation of its current structure. [4]

Before discussing the issue of the transition towards a hydrogen economy, it is useful to first list the key drivers of a hydrogen economy again. Haseldonckx and McDowall list four overarching policy objectives which drive further development of a hydrogen economy [5] [6]. These are:

- Climate change
- Energy security
- Local air quality
- Competitiveness,

whereas the term “energy security” encompasses resources of oil and gas, energy prices of primary energy sources, and vulnerability of centralized energy systems to attack.

Within the following paragraphs, the greenhouse effect and the role of combustion process emissions shall be exemplified. They intertwine as major future policy and energy issues. Also, their unique importance will be noticeable as a central thread that runs through the present and future energy economy.

The earth's naturally occurring *greenhouse effect* provides a partial absorption and reflection of thermal radiation within the earth's atmosphere. Heat radiation, absorbed from molecules of the atmosphere, becomes partially reflected back to the earth's surface. The earth surface temperature therefore averages plus 15°C, instead of minus 18°C. Two thirds water, and one third carbon dioxide plus methane facilitate the molecular base of the natural absorption and reflection effects. [7]

Humans strengthen the natural greenhouse effect through the emissions of both carbon dioxide and methane. Elevated levels of these gases launch the effect of radiative forcing: The earth receives more incoming energy from sunlight than it radiates back to space. A net gain in energy causes globally measurable warming.

According to the Fifth Assessment Report (AR5) of the Intergovernmental Panel on Climate Change (IPCC), this effect, together with other anthropogenic drivers, have been detected throughout the climate system and are extremely likely to have been the dominant cause of the observed warming since the mid-20th century. [8] Figure 1 shows observed changes in the atmospheric concentration of the greenhouse gases concentrations within a period of 1750 to 2016. Data from ice cores –symbols – and direct atmospheric measurements – lines – are overlaid.

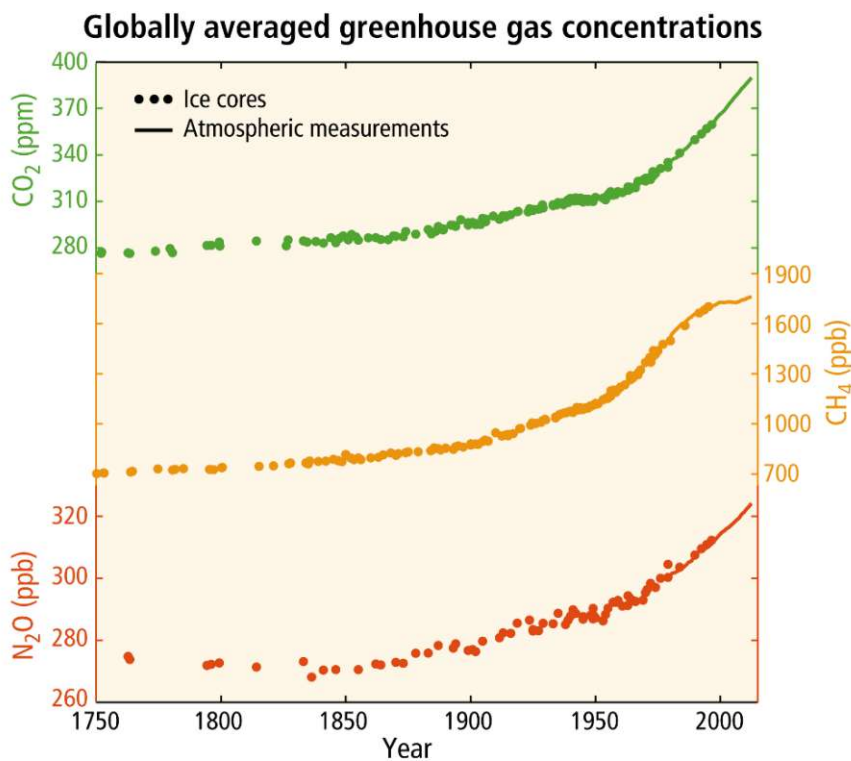


Figure 3: Observed changes in atmospheric greenhouse since 1750 [8]

The impacts of noxious substances on the environment and society's health are central themes of numerous scientific publications. Especially respirable fine dust and nitric oxides cause considerable short- and long-term effects not only on the human respiratory system, though also on the human overall health. [2] The share of emitted particles with a diameter smaller than $2.5 \mu\text{m}$ grows annually within urban regions. While these fine particles are respirable and therefore can damage both the human brain and blood system, public policy efforts introducing yet unavailable threshold values for respirable fine dust have to be introduced in the near future.

Most notably, respirable fine dust and nitric oxides are both byproducts of combustion processes within the industry, as well as public and private transport. This circumstance offers emission reducing power trains, such as battery-electric vehicles (BEVs) or fuel cell electric vehicle (FCEVs), unique chances to get necessary public acceptance. Until today, the market focused more onto the introduction of BEVs, although FCEVs grow interest among all market participants continuously [9].

1.1.3 Starting points for a hydrogen economy

According to Klell et al., it is generally useful to define the realizable possibilities and also limits of hydrogen technologies. [2] Since the umbrella term hydrogen can only offer energy in form of a secondary energy carrier, the transition from fossil-based primary energy production to renewable alternative pathways is a whole another topic. Nonetheless, electrochemical machines such as

- Electrolyzers
- Battery storage power systems, or
- Fuel cell stacks

provide applicable alternatives to heat engines, combustion processes and engines as secondary energy carriers.

One of the central issues of the world's energy policy is the storage of excess energy on a large scale. Because electrical energy is not storable without losses, the chemical compound hydrogen offers a multifaceted chance to store excess secondary energy.

Considerable advantages of hydrogen energy are:

- Energy density:
Hydrogen in its *gaseous* state conveys higher amounts of energy *per mass unit*, when compared to battery storage systems or fossil energy carriers. On a mass basis, hydrogen has nearly three times the energy content of gasoline — 120 MJ/kg for hydrogen versus 44 MJ/kg for gasoline. [10]
On a *volume basis*, though, the effect is reversed: Liquid hydrogen has an energy density of 8 MJ/L, whereas gasoline has an energy density of 32 MJ/L, as shown in Figure 4.
- High overall efficiencies of fuel cells:
To leverage the high energy density of hydrogen, a steam reforming/fuel cell system can reach efficiencies from 35 to 50% (electricity to hydrogen and back to electricity). [11]
- Enables emission-free energy consumption:

If powered directly through zero-emission renewable electricity, fuel cells and power-to-hydrogen plants can operate emission-free within the MW-area. While decentralized applications mostly offer a rather small-scale production of zero-emission hydrogen through solar and wind power, large-scale centralized power-to-hydrogen processes are mainly driven by steam-reforming – a process which uses fossil fuels to generate hydrogen. [12]

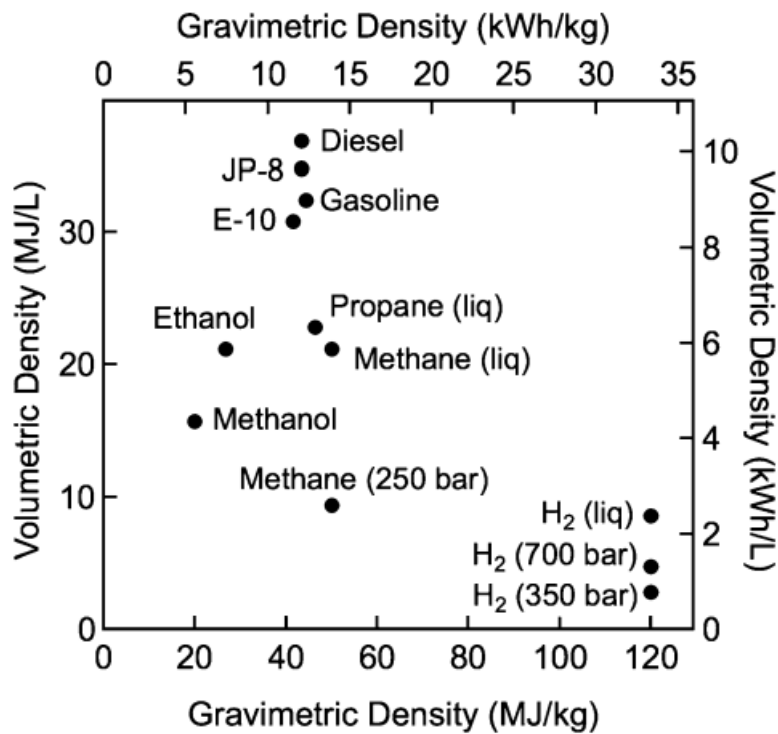


Figure 4: Comparison of specific energy versus volumetric density [10]

As the possibilities and difficulties of hydrogen energy have been exemplified above independently, it becomes obvious that hydrogen energy will take a central part in *sector coupling*. That means, offering both storage and performance capacities within the energy economy, to be able to intertwine the sectors of

- Electricity
- Heat/refrigeration supply
- Traffic, and
- Industry

with each other, and optimize their interaction.

Furthermore, a starting point is obviously the *steel industry*, researching on substituting hydrogen as a green reducing agent, generated by using renewable energy. [13]

The traffic sector is definitely another worth mentioning starting point for hydrogen as a *fuel medium*. This starting point has been outlined already, and will be taken on several more times within the upcoming paragraphs.

1.2 Aim of work

1.2.1 Aims

The aim of the present work is a *thermodynamic analysis* of a hydrogen fuel station by means of a *continuous dynamic simulation*.

The thermodynamic analysis shall provide state and process variables at discrete state points within the observed system borders of the hydrogen fuel station.

These obtained results shall furthermore

- serve the continuous R&D efforts of the plant design, and
- provide necessary data for a more precise and faster routine for the dimensioning of the commercially available fuel station systems.

The aim of work contains the following sub-aims:

- i. Generating a simplified physical model of an examined subsystem of the whole plant system within the simulation software Simscape-Simulink
- ii. Generating pressure and temperature vector fields out of acknowledged chemical property libraries (e.g. RefPROP, ChemPROP, etc. ...), and implementing these vector fields within Simscape-Simulink to be able to utilize real gas behavior
- iii. Validation of the generated simulation results through already available fueling process calculation results. These results have been calculated numerically for the most conservative operation scenarios of a fueling process.

Through the simulation, the following shall be gained:

- A deeper understanding of the physical behaviour of the overall fuelling process
- A software-based possibility to predict the thermodynamic behavior of the fueling system for variable plant sizes

Additionally, the created simulation tool shall be able to display the operating behavior of the fueling station with its corresponding thermodynamic data inside each modeled constructional element.

This data can be enormously helpful and interesting for testing the modeled fueling station close to its designed operating limits. Just close to its operating limits, the design of the plant shows its current weaknesses and discrepancies during operation mode. If equivalent tests were conducted upon a test rig, a possible standstill or even breakdown of the test rig for an unpredictable period of time – due to tests close to its operating limits – would cause considerable amounts of costs.

Through achieving the overall aims of this work, the competitiveness of the fueling plant can be additionally increased.

The following factors have been originally considered and summarized as a second major aim of work, namely the part of a “technical economic analysis”. As it became obvious during elaborating on the simulation task itself, the part of the technical economic analysis did not fit into the available time frame of the master thesis project. Nonetheless, the economic factors – determining the overall attractiveness and competitiveness of the plant – shall be listed here:

- Required amount of space of the whole fueling plant
- Optimal usage of the high pressure storage banks through highly elaborated cascade shift concepts. Due to the decreased pressure losses , this offers
 - saved fuel costs for the fueling station operator, and
 - more available fuel for the final customer
- Sophisticated component dimensioning to reduce manufacturing costs and guarantee highest levels of operation availability and safety

1.2.2 Procedure

At the start of the master thesis project, a distinct scope of work neither was formulated, nor was it the intention to elaborate along a tight and pre-defined procedure. A rather open approach towards the upcoming research efforts was both more constructive and also necessary, because

- ❖ the choice of the used simulation software had to be made within the first couple of weeks of the master thesis project. Therefore, the possible pathways of simulation, given by the considered software environments, offered different approaches of work, although all considered software packages do operate by use of up to date numerical solver algorithms.
- ❖ The company's experience in creating a continuous dynamic simulation tool for the rather young technology of hydrogen fueling was little. Estimations of the possible work progress could be made. Yet because the master thesis project was breaking a new ground for the relatively young company, this situation required resources and time to correct the path of work sometimes.

In hindsight, the chosen approach of work can be structured in six consecutive steps:

1. Formulation and delimitation of the superior project aim, which was *the creation and programming of a simulation tool for a thermodynamic analysis of a hydrogen fueling station*.
2. Discussion and choice of possible software and simulation environments
3. Setting up the simulation software Simscape-Simulink and integrating pressure and temperature vector fields from trusted chemical property libraries to be able to simulate real gas behavior
4. Step-wise setup of a thermodynamic model of a non-steady flow process within Simscape-Simulink.

At once, the validation of the first simulation results of the simulated system, becoming more complex and realistic. Literature, company-internal experience and numerical calculation values for a most conservative plant operation scenario serve as a basis.

5. Adaption of the model to the required degree of complexity to be able to display state variables, such as pressure, temperature, mass flow, density, and the following. At once again, validation of the obtained results with the aid of literature, company-internal experience and numerical calculation values.
6. Optimizing of the working simulation tool in terms of the switch dynamics of the cascade switching mechanism of the high pressure storage tanks

1.3 Hydrogen as an energy carrier

1.3.1 Production

Hydrogen can be produced either from hydrocarbons or directly from water.

Hydrocarbons are available as fossil fuels or biomass. Concurrently, the following processes allow a commercial production of hydrogen, or are in basic research:

- Reforming processes, utilizing either
 - steam - *steam reforming*,
 - *partial oxidation*, or
 - a combination of the two – *autothermic reforming*
- Water splitting through thermal energy - *cracking*
- Water splitting through electric energy – *electrolysis*
- *Gasification* of fossil fuels
- Water splitting through sunlight – *photocatalysis*
- Photobiological generation by photosynthetic organisms, such as algae.

For any source of hydrocarbons – e. g., bio mass, coal, methane, oil residues – and water, energy is required for any chosen separation process, and has to be provided as electric current, heat or light. [14]

The production method is crucial as it impacts the price of one unit of hydrogen as an energy carrier – e. g. one kilogram liquid hydrogen that powers a stationary used PEMFC.

A whole another topic are the emissions and environmental impacts that are caused by the considered upstream process. The possible rates of GHG-emissions and overall environmental impacts differ enormously among the available processes, and are subject of numerous intergovernmental research assignments. [15]

At present, approximately 40% of the worldwide hydrogen demand are generated as a byproduct of industrial processes, such as numerous processes within refinery or the chloralkali process. The residual 60% are generated on individual purpose. Yet, 95% of the worldwide produced hydrogen stems from fossil sources, and the remaining 5% are direct products of electrolysis. Due to the overall yet higher efficiency factors of fossil fuel-dependent processes, these processes remain favored until now. [16]

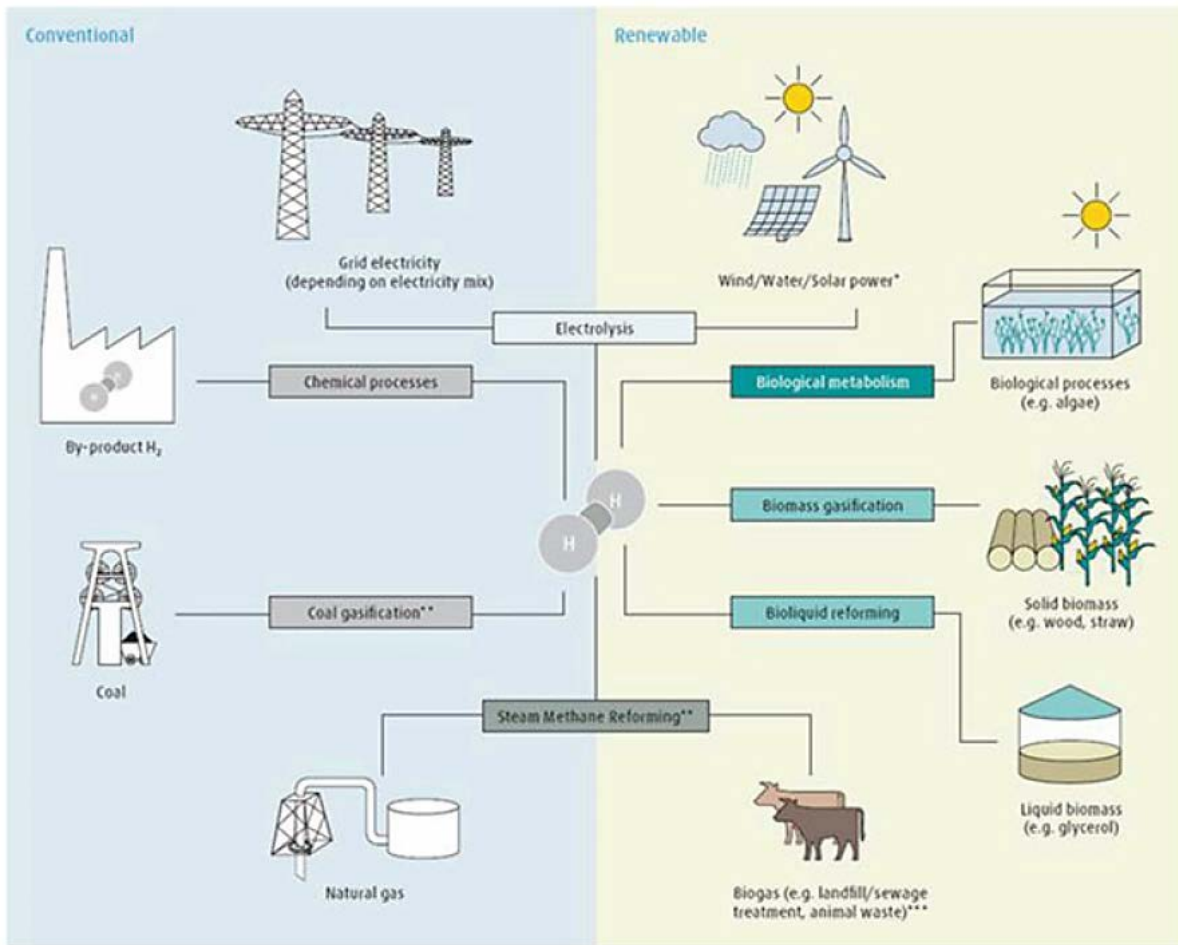


Figure 5: Hydrogen production pathways from fossil and renewable sources [14]

Figure 5 sketches the available production pathways from fossil feedstock or renewable sources.

Reforming

The most widely used production method is the *reforming* of fossil hydrocarbons. Steam reforming offers about 70-80% efficiency rates, with regard to the calorific value of the used natural gas.

The operation costs decrease strongly with an increasing plant size. The plant sizes that

are available today range from $1000 \frac{Nm^3}{h}$ to $120.000 \frac{Nm^3}{h}$. Because fossil hydrocarbon sources constitute the greater part of source material, significant amounts of carbon dioxide are emitted. The usage of synthetic natural gas, produced out of biofuels, can lower the total emission rates of a reforming process. [14]

Gasification

Another production method is the gasification of fossil or substitute natural fuels. Over the past decades, sources of the umbrella term “biomass” – that means wood, waste wood, turf, sewage sludge, organic waste, and many more – gained increased attention within research and the industry

sector of gasification. It is expected that biomass fueled gasification processes are more carbon-neutral than the conventional coal driven gasification. Despite this fact's overall acceptance, studies have been trying to show the opposite. [15]

Electrochemical water splitting - electrolysis

The electrolytic processes differ depending on the electrolyte, the operating pressure and the operating temperature used. Namely, three technologies are in constant research focus:

- Alkaline electrolysis
- Proton exchange membrane electrolysis
- High-pressure electrolysis

whereby alkaline electrolysis has reached a usable state of technological maturity, and is being used in large-scale already.

Alkaline electrolysis plants with a possible capacity of 30.000 Nm³/h are in use for fertilizer production, as in Assuan, Egypt, and have been object of research since the 1940s.

Proton Exchange Membrane Electrolysis plants are expected to be able to significantly lower the overall costs for the produced kilowatt-hour of hydrogen, due to the concurrent intensive research activities.

The *high-pressure electrolysis* is the combination of an electrochemical compression up to a mid-level pressure and a downstream installed mechanical compression of the aimed final pressure.

Precompressed hydrogen at pressures of 30-100 bar is being used for the feed-in into the natural gas grid, at 200-300 bar for the standard storage method of gaseous hydrogen in cylinder bundles, or at 1000 bar for the fueling of fuel cell electric cars.

By pressurizing the hydrogen already within the electrolyser up to 200-300 bar, the need for an external hydrogen compressor is eliminated. This results in significantly lower energy demands.

Another bonus of high-pressure electrolysis are the decreased requirements of periphery components, such as pipes or mid-pressure-range storage tanks, due to high pressure compression units, becoming redundant. [17]

If powered by electricity of 100% renewables, such as wind, hydrogen or solar power, electrolysis can lower carbon emissions the most, compared to the alternative production methods. Through to the continuing cost reductions being made, electrolysis is presumed to be the key technology for the further expansion of renewable power plants and sector coupling. Also, the up-to-date energy storage concepts - namely Power-to-Gas, Power-to-Hydrogen, etc. – gain great potential through electrolysis.

1.3.2 Storage

The up-to-date storage technologies are:

- Compressed gaseous hydrogen (CGH_2), stored and transported at pressures between 300 and 700 bar
- Liquid cryogenic hydrogen (LH_2), stored and transported at temperatures below $-252.8\text{ }^\circ\text{C}$
- Cryo-compressed hydrogen (CcH_2)
- Hydrogen, stored within chemical bondings, mostly within solid bodies or fluids (e.g. ionic bondings, metal hydrides, etc.); presently at experimental stage;

Due to its low density, the storage of hydrogen at reasonable energy densities poses a technical and economic challenge.

Gaseous Storage

The storage of gases in pressure vessels is a proven and tested technology. CGH_2 is commonly available in containers at pressures between 200 and 300 bar, suitable for long-term storage use.

With the aim of reaching maximum volumetric and gravimetric energy densities, heavy-duty and passenger FCEVs fuel CGH_2 at pressures between 350 and 700 bar.

A conventional CHG_2 fueling process uses the pressure difference to make use of an adiabatic throttled flow process. Therefore, mechanical compressors are in use to provide the CGH_2 , stored within bundles of high-pressure buffer flasks, at pressures between 900 and 1000 bar. Within piston compressors, five compression units work serially at energy expenditure rates between 2.5 to 5 kWh/kg CHG_2 , amounting approximately 15% of the calorific value of hydrogen. [16] [2]

In demand of lower pressure targets, diaphragm compressors are being used regularly. Novel compression technologies for special applications are the ionic liquid piston compressor and electrochemical compressors. [18]

Fluid Storage

Together with increased efforts considering the production, storage and infrastructure, liquid cryogenic hydrogen provides higher energy densities, compared to gaseous compressed hydrogen. It is being used if the vehicle range is deciding, or if greater amounts of excess hydrogen have to be stored.

The energy expenditure for the liquefaction amounts to approximately 20-30% of the calorific value of hydrogen. Peripheral technical components, such as pipes, valves or fueling station sockets, must be made of austenitic steel, utilizing vacuum insulation, and therefore are more complex in construction and more expensive. [14]

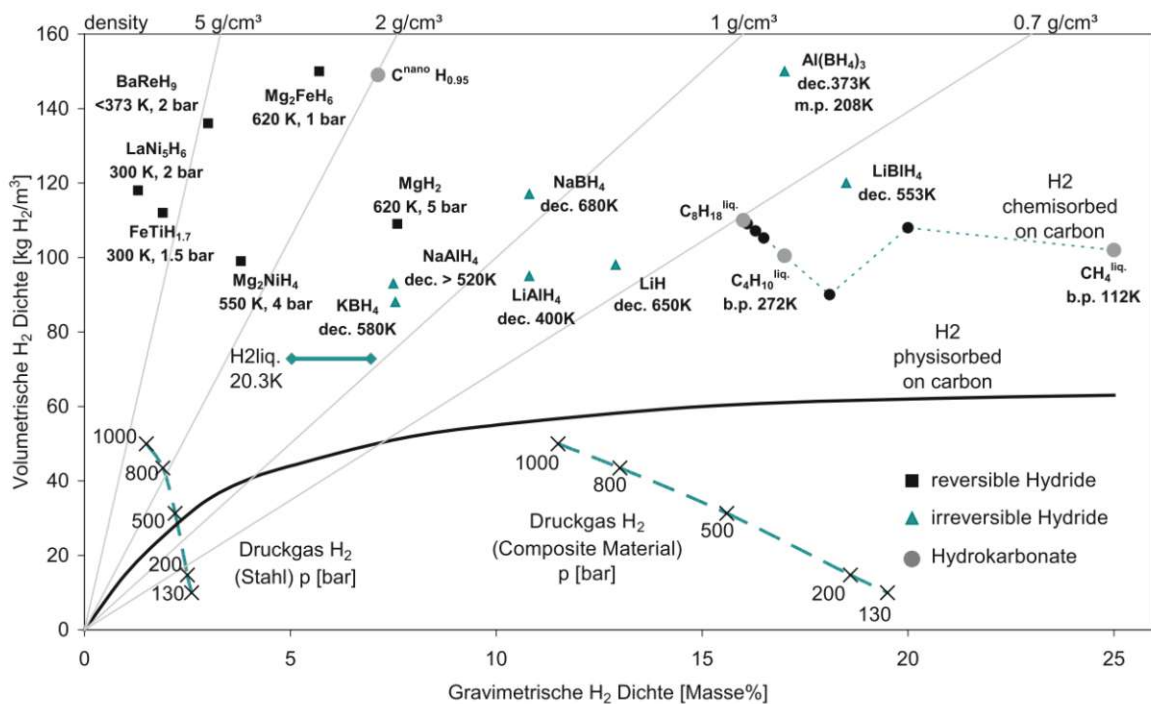


Figure 6: Gravimetric versus volumetric hydrogen densities of potential storage technologies or bonding partners [19]

Figure 6 shows the relations between gravimetric and volumetric hydrogen densities of potential storage technologies or bonding partners. [19]

Cryo-compressed storage

In its so-called cryo-compressed state, hydrogen is stored slightly above 33.2K and at pressures between 31.1 and 350 bar in order to reach even higher energy densities than in its liquid aggregate state, up to 80 kg/cm³. The state of hydrogen within this pressure-temperature zone is being called *super-critical*, taking form as a saturated fluid. [2]

Due to heat input and warming, the pressure will, nevertheless, rise in the tank and eventually reach a limit, where a boil-off valve has to open. Therefore, applying increased pressure on liquid hydrogen decreases evaporation losses.

Demonstrations have shown that a significantly higher driving range could be achieved with a cryo-compressed tank. Up to 1050 km were driven with a full tank mounted on a CcH₂-fueled electric engine. [20]

Figure 7 shows hydrogen's density versus temperature, and the segments of all possible combinations of aggregate states.

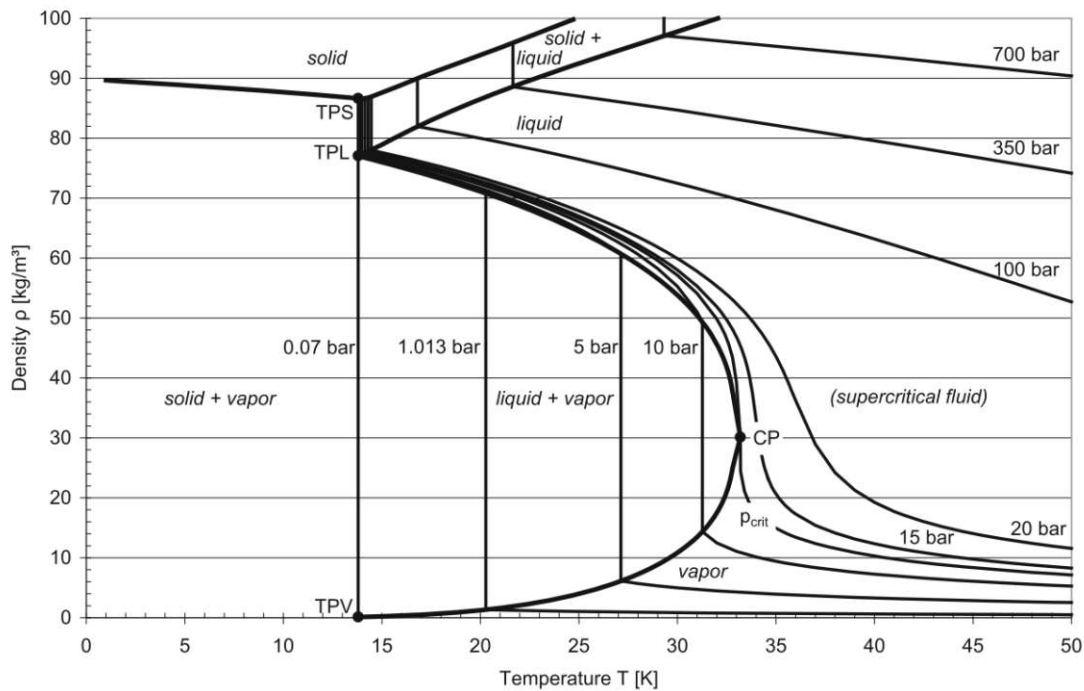


Figure 7: Aggregate states of hydrogen, depending on the relationship between density, temperature and pressure [2]

Yet the increased constructional requirements for the storage tanks concerning the elevated pressure levels at still very low temperatures also increase the overall costs of CcH₂-application respectably. Compressed gaseous CH₂ and liquid storage LH₂ still emerge as the commercially affordable choice of storage, while CcH₂ is still in a development phase. [10] [14]

Tank systems

Presently, four tank types are in permanent global use:

- Typ 1: steel tank
- Typ 2: inner tank is a metal liner, partially wrapped by a carbon fiber net
- Typ 3: metal liner, entirely wrapped by a carbon fiber net
- Typ 4: plastics liner, entirely wrapped by a carbon fiber net

Type 1 steel tanks are mostly composed of chromium molybdenum steels, with volumetric capacities of 2 to 50 liters. They offer high reliability at low costs. Due to their rather high self-weight, the achievable storage densities are limited by 0.4 kWh/kg.

Type 3 and 4 tanks are the standard tank types, being used for vehicle storage tanks, both for heavy goods vehicles and passenger cars. [14]

3.1.3. Transport

The transport and distribution of hydrogen is subject to the following methods and technologies:

- Road transport by trailers
- Transport through pipelines
- Sea transport by cargo ships
- Rail transport by freight trains

Transport by trailers, cargo ships and freight trains is suitable for gaseous and liquid hydrogen, while transport via pipelines is suitable for gaseous hydrogen only.

Road

Transporting CGH_2 and LH_2 on the road via heavy goods trucks and trailers is state of the art. In either state, hydrogen is being transported within cylinder trailers or tube trailers (fewer, but bigger single vessels). The trailers contain 10-36 cluster tanks, varying in length from 6 to 12 meters. In case of transporting gaseous hydrogen, the transport pressure range is from 200 to 500 bar.

Recently, the cluster tanks tend to become replaced by composite material tanks, being fully or partly made of plastic composites. This can improve the ratio between dead weight of the tank and payload remarkably, if costs of composite tanks tend to decrease furthermore.

Transporting hydrogen as cryogenic liquid has an advantage, considering the ratio of dead weight to payload. The transport capacity becomes as far as 9 times higher compared to compressed gaseous hydrogen, [14]. Yet, the advantage of higher density is partly offset by the high energy demand for liquefaction.

Whether the transport of LH_2 is profitable depends on the particular conditions, especially on the distance from distributor to customer, since fuel, vehicle fleet and personnel costs are decisive for the distributor's action.

Pipelines

For the large-scale transport of hydrogen, pipelines are the most economical solution among the abovementioned alternatives. Pipelines allow a distribution without building up traffic or greenhouse gases. [18]

Presently, pipeline systems transporting H₂ - such as in the German Ruhr area or in the industry area of German Leuna-Bitterfeld-Wolfen – are being operated with pressures between 20 and 100 bar.

Technological similarities and synergies occur through the mixture of natural gas and compressed hydrogen within pipelines. For example, although hydrogen has a lower energy density than methane it also is lower in viscosity. Thereby, assuming any given pipe diameter and pressure drop, about 75% of an equivalent energy flux of methane can be transported.

Currently, the global realized share of injected gaseous hydrogen averages within the percentile range. Various research projects in Europe estimate that concentrations between 10 and 20% are feasible within the next years. [22] [23]

Other traffic ways

Hydrogen can also be transported via rail, inland waterways or sea-going vessels within suitable, so-called *liquid hydrogen tanktainers*. However, the transport of hydrogen over large distances increases the ratio total costs to delivered energy content, and is currently not considered as sustainable under economic aspects. [14]

2. Thermodynamics

Fundamentally, the formulation of models for thermodynamic systems rests upon the fundamental thermodynamic relation and the thereof derivable balance equations, as well as upon the determination of the system states and the change of states. [24] [25] The first subchapter will therefore dwell upon the derivation of the fundamental thermodynamic relation and the underlying laws of thermodynamics.

Subsequently, the fundamental equations of heat transfer will be explained, as they are essential for the creation of real gas modelling and all consecutive calculations.

Within a third subchapter, the basic correlations of fluid dynamics, and the model's utilized material properties, dimensionless numbers and its correlations shall be explained, providing an overview on the underlying calculation approaches and assumptions of the fuel station's model.

2.1 Balance equations

The general structure of a balance equation for the balancing of a variable X is

$$dX = \sum_{k=1}^n dX_k^{sb} + dX^S \quad (3.1)$$

with k as the number of transport processes dX_k^{sb} transcending the system boundaries (sb), and dX^S as the source term, describing the created or annihilated value of the state variable. A sign convention for future uses becomes declared at this point:

- Transport variables dX_k^{sb} , entering the system boundaries, do have a positive sign
- Transport variables dX_k^{sb} , leaving the system boundaries, do have a negative sign

2.2 Fundamental thermodynamic relation

The **fundamental thermodynamic relation** is generally expressed as a microscopic change in internal energy in terms of microscopic changes in entropy, and volume for a closed system in thermal equilibrium in the following formulation of

$$dU = TdS - pdV + \mu dN \quad (3.2)$$

This form may be formulated in other variations, using the differentials of other fundamental state variables – e.g. U for internal energy, T for absolute temperature, S for entropy, P for pressure, V for volume, μ for the chemical potential, and N for the particle number, all of which shall be explained in the subsequent subchapters in detail.

Within this scope of analysis, the state variables can also be called *thermodynamic potentials* or characteristic functions. These are furthermore three of the possible eight calculable *Legendre transformations* of the internal energy U. [26] It shall be mentioned here that the denotation of the state variables is not uniform within literature.

The differentials can be formulated in terms of the enthalpy as

$$dH = TdS + Vdp + \mu dN \quad (3.3)$$

or in terms of the Helmholtz free energy F as

$$dF = -SdT - pdV + \mu dN \quad (3.4)$$

and in terms of the Gibbs free energy G as

$$dG = -SdT + Vdp + \mu dN. \quad (3.5)$$

Equation (3.2) states that the so-called **equations of state** – fundamental correlations between thermodynamic state variables– are the first-order derivations of the fundamental thermodynamic relation (3.2).

The *state variable of total enthalpy H* describes the heat which is absorbed or emitted by an observed thermodynamic system. Its meaningfulness builds upon a difference of two objected states, and not a single value. Therefore, system changes that provide an excess of heat are labelled as *exothermal* and are assigned with a negative algebraic sign by convention. System changes that require heat for their succession are called *endothermal* and hold a positive algebraic sign by convention.

The total enthalpy H is nothing more than a Legendre transformation of the internal energy U.

The state variable of internal energy U is the amount of energy stored by the sum of molecules of an objected thermodynamic system.

The *Helmholtz free energy* or simply **free energy F** is the Legendre transformation of the internal energy U in regard to entropy S. It measures the useful work obtainable from a closed thermodynamic system at a constant temperature and volume. The difference of the change in the Helmholtz energy during a process is equal to the maximum amount of work that the system can perform in a thermodynamic process in which volume is held constant.

The *Gibbs free energy* or **free enthalpy** G is another thermodynamic potential that can be used to calculate the maximum amount of reversible work that may be performed by a system, constant in temperature and pressure. In other words, it is the maximum amount of non-expansion work that can be measured within a thermodynamically closed system. This maximum can be attained only in a completely reversible process.

Within stoichiometry, the Gibbs energy is also the thermodynamic potential that is minimized when a system reaches chemical equilibrium at constant pressure and temperature. Its derivative therefore vanishes at the equilibrium point of a reaction system.

Its second-order derivations are the basis of further fundamental thermodynamic relations: The so-called *Maxwell correlations*. They allow the description of a change of state variables – e.g. temperature T or entropy s – through using the derivations of other state variables, such as pressure p or volume V .

The four most common Maxwell relations are the equalities of the second (mixed) derivatives of each of the four thermodynamic potentials, with respect to their *thermal natural variable* (Temperature T , or entropy S) and their *mechanical natural variable* (pressure p , or volume V), and can be formulated as:

$$\left(\frac{\partial T}{\partial V}\right)_S = -\left(\frac{\partial p}{\partial S}\right)_V = \frac{\partial^2 U}{\partial S \partial V} \quad (3.6)$$

$$\left(\frac{\partial T}{\partial p}\right)_S = -\left(\frac{\partial V}{\partial S}\right)_p = \frac{\partial^2 H}{\partial S \partial p} \quad (3.7)$$

$$\left(\frac{\partial S}{\partial V}\right)_T = -\left(\frac{\partial p}{\partial T}\right)_V = -\frac{\partial^2 F}{\partial T \partial V} \quad (3.8)$$

$$-\left(\frac{\partial S}{\partial p}\right)_T = -\left(\frac{\partial V}{\partial T}\right)_p = \frac{\partial^2 G}{\partial T \partial p} \quad (3.9)$$

2.2.1 Equations of state

An equation of state is the correlation between at least two thermodynamic state variables. It describes the properties of fluids, mixtures of fluids or solids under a given set of physical conditions, such as pressure, volume, temperature or internal energy.

A state function describes the equilibrium state of a system and does not depend of the path by which the system arrived at its present state. The state function makes use of the so-called state variables, e.g. pressure, volume, temperature or internal energy, which depend solely on the current equilibrium state of a system.

Currently, the number of applicable equations of state for distinct conditions is extensive. In the following, the equations of state which are most relevant, with regard of history and our distinct project scenario, shall be explained.

2.2.1.1 Thermal equations of state

The **ideal gas law**, also called the **general gas equation**, is the equation of state of a hypothetical ideal gas. It is a good approximation of the behavior of many gases under many conditions, although it has several limitations. The ideal gas law can be written e.g. in its empirical form as:

$$pV = nRT \quad (3.10)$$

where n is the amount of substance, and R is the ideal gas constant. Fluids at low density and high temperature approximate the behavior of a classical ideal gas.

At higher pressures, lower temperatures or phase changes, the so-called real gas behavior comes into play and has to be considered categorically. For real gases and fluids, the ideal gas law becomes expanded by the substance-specific compressibility factor or real gas factor Z , and reads

$$pv = RTZ \quad (3.11)$$

The trend of the hydrogen-specific real gas factor Z is displayed in Figure 8. One can realize that the real gas factor increases significantly with increasing pressure.

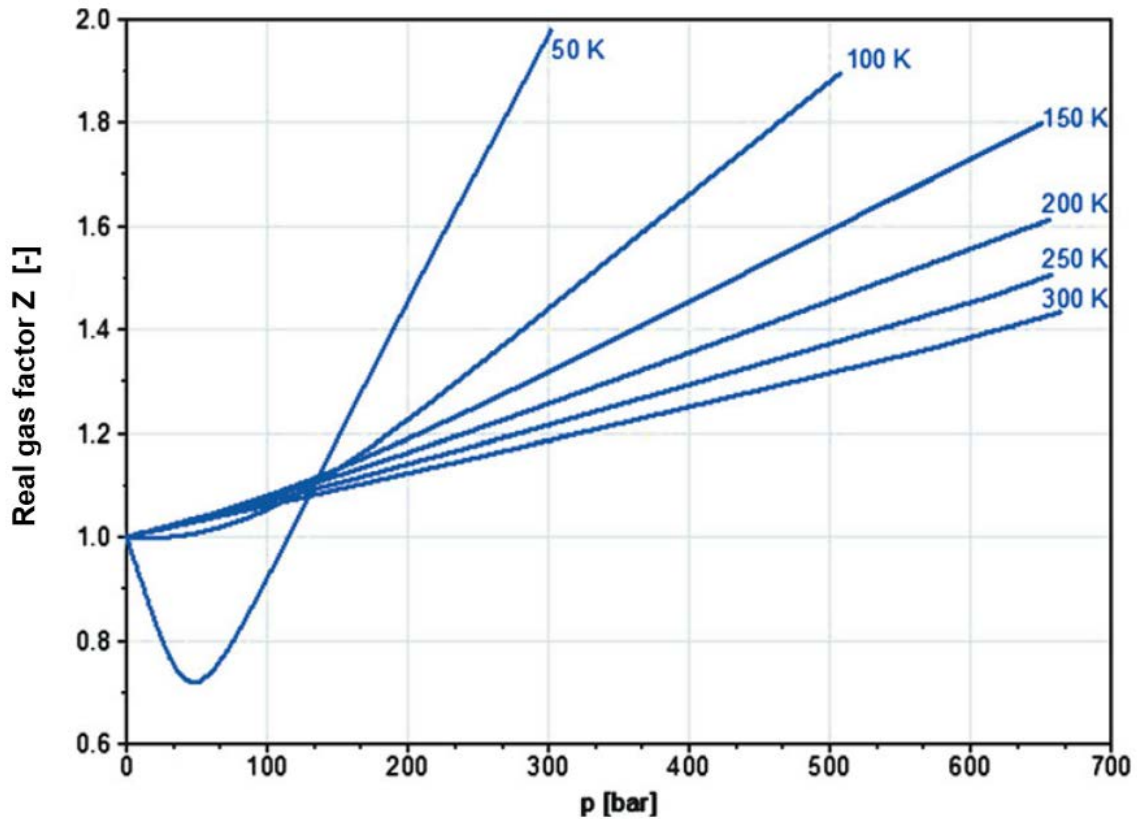


Figure 8: Real gas factor Z of hydrogen, depending on pressure and temperature [2]

A more comprehensive and up to date approach towards calculating real gas behavior is the Van der Waals equation. This cubic equation shall only be mentioned here, and becomes very well elaborated on by Silbey et al. [27].

Sakoda et al. provides a comprehensive exemplification of the present-day equations of state for real gas calculations on hydrogen; [28]. They propose the state equation of Leachman 2009 for its versatility and accuracy in application and predict that the well-established state-equation of Younglove will be displaced thereby within the next years, [29], [30].

2.2.1.2 Caloric equation of state

Substance-specific correlations between any state variables cannot be entirely described by a thermal equation of state. Another state variable, only being dependent on temperature, is necessary therefore.

The **caloric equation of state** describes the inner energetic state of a thermodynamic system. The equation can be formulated in regard to the internal energy u , being

$$u = u(v, T) \tag{3.12}$$

and in regard to the specific enthalpy h , being

$$h = h(p, T) \tag{3.13}$$

Equation (3.12) is namely the *caloric equation of state of internal energy*, and (3.13) the *caloric equation of state of enthalpy*.

The total differential of (3.12) and (3.13) equals

$$du = \left(\frac{\partial u}{\partial v}\right)_T dv + \left(\frac{\partial u}{\partial T}\right)_v dT \quad (3.14)$$

and

$$dh = \left(\frac{\partial h}{\partial p}\right)_T dp + \left(\frac{\partial h}{\partial T}\right)_v dT. \quad (3.15)$$

The second differential term of (3.14) provides the **specific heat capacity at constant volume c_v** ,

$$c_v = \left(\frac{\partial u}{\partial T}\right)_v \quad (3.16)$$

and the second differential term of (3.15) **the specific heat capacity at constant pressure c_p**

$$c_p = \left(\frac{\partial h}{\partial T}\right)_p. \quad (3.17)$$

These specific heat capacities declare the necessary quantity of heat to be able to heat up 1 kg of a substance by 1 K. In other words, a system can take up more heat, the greater its heat capacity is.

c_v and c_p are tabulated regarding various physical conditions, though commonly tabulated in reference to the normal pressure $p_0 = 1.10325$ bar, dependent on temperature.

The **state variable entropy S** is a fundamental state variable, quantified in J/Kkmol as an extensive state property. It enables conclusions and predictions on the direction and absolute value of flow processes, changes of state and the convertibility of forms of energy into related forms of it.

Assuming an open system together with only reversible changes of state, the specific entropy s reads

$$ds = \frac{dQ}{T} + dm_{in}s_{in} - dm_{out}s_{out}. \quad (3.18)$$

For thermodynamic analysis, the **temperature-entropy diagram** with temperature T and entropy s on axes and lines of constant pressure, density and enthalpy has proven as very useful. Changes of

states, or exchange of work or heat – can be visualized clearly. Also, basic thermodynamic effects, such as the **Joule-Thomson effect**, can be displayed vividly.

Assuming a reversible change of state, equation (3.16) becomes

$$ds = \frac{dq_{rev}}{T}. \quad (3.19)$$

The reversible heat transfer therefore corresponds to the area below the curve of the corresponding process in the T-s diagram:

$$q_{rev} = \int T ds \quad (3.20)$$

With the definition of reversible heat

$$dq_{rev} = du + pdv = dh - vdp \quad (3.21)$$

it follows that the amount of transferred heat – thus the area underneath the process curve within the T, s-diagram – corresponds to the change of internal energy u or enthalpy h , given an isobaric or isochoric process. Furthermore, the specific heat capacity c corresponds to the subtangent of the process curve in the diagram:

$$c = \frac{dq_{rev}}{dT} = T \frac{ds}{dT} \quad (3.22)$$

A T, s-diagram for hydrogen for temperatures between 85 K and 330 K is shown in Figure 9, [31].

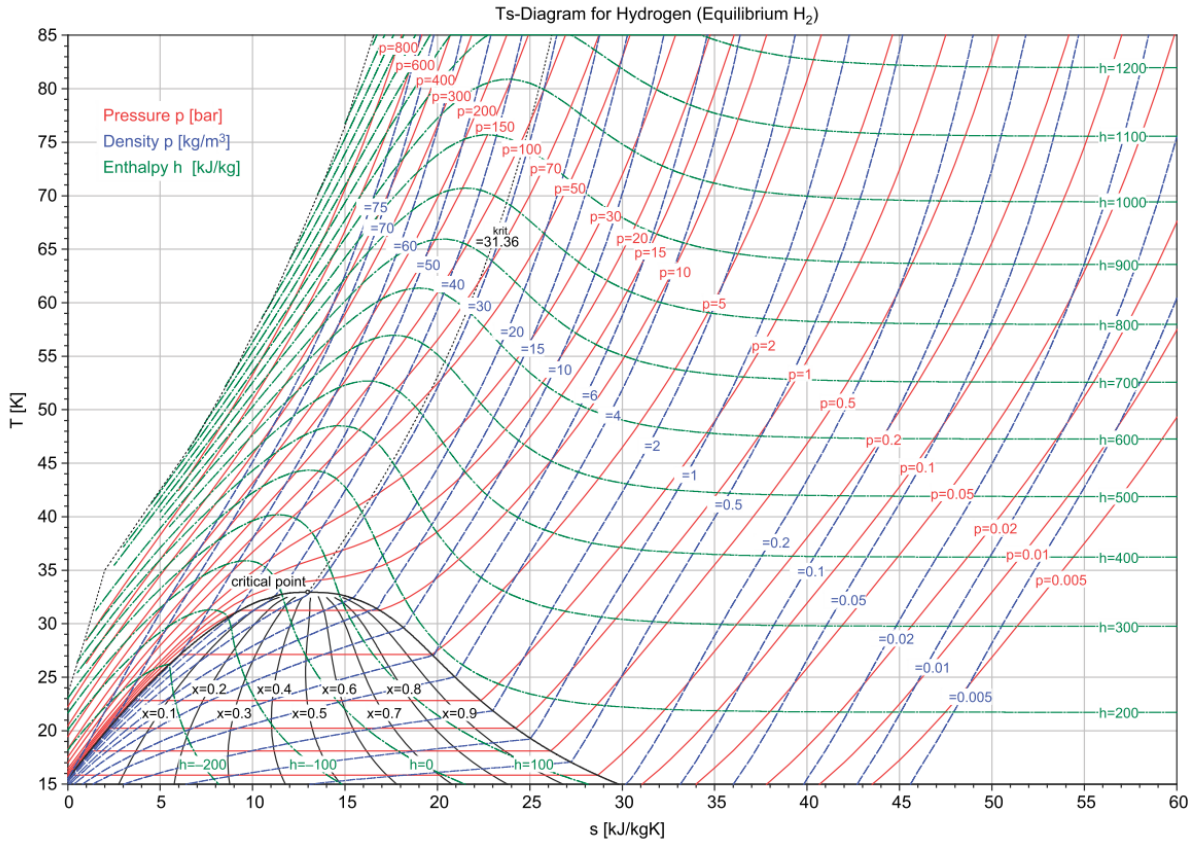


Figure 9: T,s -diagram for equilibrium hydrogen for temperatures from 15 to 85 K [2]

The Joule-Thomson coefficient μ_{JT} describes the extent and direction of temperature change for an isenthalpic change of state, being:

$$\mu_{JT} = \left(\frac{\partial T}{\partial p} \right)_h \quad (3.23)$$

A positive Joule-Thomson coefficient means that a decrease in a system's temperature takes place along the curve of an isenthalpic pressure decrease. In a figurative T,s -diagram, as in Figure 10, this can be noticed as a falling isenthalpic curve with a congruent pressure decrease.

An applied industrial example of liquefying hydrogen through the Joule-Thomson effect is the well-established Linde-Hampson cycle. Through applying compression onto the system, work is introduced into the system. This furthermore heightens the system's pressure, and lowers its internal temperature. A simple process flow diagram of the Linde-Hampson cycle is shown in Figure 10.

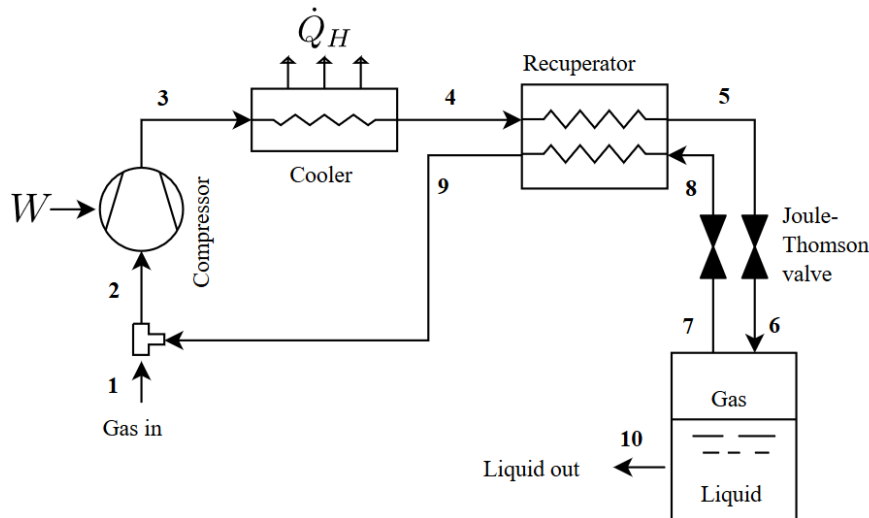


Figure 10: Process flow diagram of a basic Linde-Hampson cycle, used e.g. for hydrogen liquefaction [32]

A negative Joule-Thomson coefficient means that an increase in temperature takes place along an isenthalpic pressure decrease. In a T, s -diagram, this can be recognized as a rising isenthalpic line with pressure decrease.

This variant of the Joule-Thomson is a key-factor within this scope of work, as it can be observed while filling a vessel with gaseous hydrogen by using a non-steady flow process (throttling process).

The Joule-Thomson effect occurs only when a gas or gas mixture experiences change in temperature during an isenthalpic pressure change. Furthermore, an ideal gases doesn't experience a change in temperature if its enthalpy remains constant, e.g. flowing through a restriction. Thus, it can be reasoned from the T, s -diagram that a gas can be considered as an ideal gas within the area where isenthalpic lines are oriented horizontally.

2.2.2 Conservation equations

The aim of work, as described in subchapter 1.2.1, requires the calculation of state variables, such as pressure, temperature, mass and mass flows, and different measures of transported energy, amongst other things. The so-called **conservation equations** allow the calculation of most state variables *for a closed system at constant time*, being just as essential as the fundamental correlations described in 2.2.

Instead of using their continuous form, the conservation equations used will be furtherly expressed in integral form within our scope of work. The advantage of the integral form is that it requires less smoothness of the solution, extending the class of admissible solutions, e.g. becoming applicable for movable, non-steady control systems.

Among various other, these are the four *exact* equations that are most relevant in our scope of work:

- Conservation of mass and energy
- Conservation of momentum,
- Conservation of angular momentum, and
- Conservation of electric charge.

The practical utilization of a conservation equation is formulating a balance equation for the corresponding variable.

2.2.2.1 Mass balance

Within an open thermodynamic system, the change of total mass equals the difference between supplied and discharged mass. The **mass balance** of an open single-component system reads

$$dm = dm_{in} - dm_{out} \quad (3.24)$$

For discharged masses, an exception applies, whereby dm_{out} must be greater than zero, $dm_{out} > 0$. For the stationary case, meaning no mass is being stored within the system boundaries, $dm_{out} = 0$, so that $dm_{in} = dm_{out}$.

2.2.2.2 Energy balance

The extensive state variable energy E of a thermodynamic System consists of the kinetic energy E_{kin} , the potential energy E_{pot} and the internal energy U :

$$E = U + E_{kin} + E_{pot} = m\left(u + \frac{w^2}{2} + gz\right) \quad (3.25)$$

The law of energy conservation, a central statement of the first law of thermodynamics, reads as follows:

A system's energy can only change by supply or discharge of energy through the system borders. [33]

Within thermodynamics, the abovementioned energy change can happen through heat, work or the transport of matter-bound energy. Including heat and work supply, an energy balance of a single-component system can be sketched as follows:

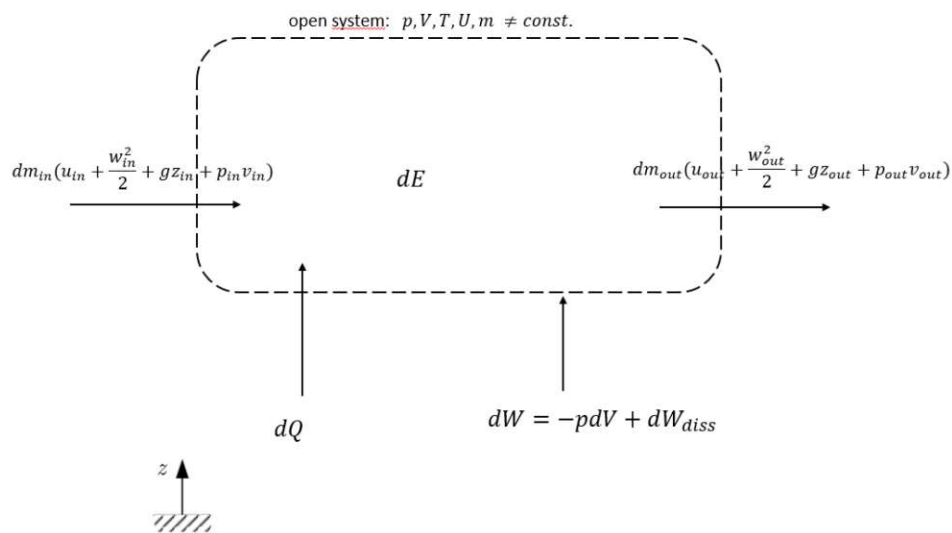


Figure 11: Open non-steady system with heat and work supply and discharge [25]

Out of the law of conservation of energy, the following equation can be formulated for energy E, and provides a differential notation of the **energy balance** as well:

$$dE = dQ + dW + dm_{in} \left(u_{in} + \frac{w_{in}^2}{2} + gz_{in} + p_{in} v_{in} \right) - dm_{out} \left(u_{out} + \frac{w_{out}^2}{2} + gz_{out} + p_{out} v_{out} \right) \quad (3.26)$$

In the scenario of the project's non-steady flow process, the terms of kinetic and potential energy can be neglected. The system's energy change can therefore be simplified to

$$dE = dQ + dW + dm_{in}(u_{in} + p_{in}v_{in}) - dm_{out}(u_{out} + p_{out}v_{out}) \quad (3.27)$$

Other modes of work, such as magnetic, electric or wave work, are not relevant within our system's scope. The work dW feeded into the system shall only comprehend volume work and dissipated work:

$$dW = -pdV + dW_{diss} \quad (3.28)$$

2.2.2.3 Momentum balance

In Newtonian mechanics, **momentum** \mathbf{p} is the product of the mass m and velocity \mathbf{v} of a particle, a sum of particles, or an object, reading

$$\mathbf{p} = m\mathbf{v} \quad (3.29)$$

It is measured in $\frac{kg \cdot m}{s}$, and is classified as a vector quantity, having both magnitude and direction.

The momentum balance states that a change of momentum within an open system equals the change of forces, acting on the outside of the same system. In its Eulerian form, it reads

$$\frac{d}{dt} \int_v \rho \vec{v} dv = \int_v \rho \vec{g} dv + \int_A \vec{t} dA \quad (3.30)$$

where \vec{g} meaning the gravitational acceleration, and \vec{t} meaning the surface tension on top of surface A .

If formulated in a global continuous form, such as in e.g. (3.30), the momentum balance serves as an essential element for the derivation and formulation of the Navier-Stokes equation.

The Navier-Stokes equation serves for nearly all subsequent fluid mechanics calculations within the source code structure of the physical model.

2.3 Fluid mechanics

For obtaining basic measurements and knowledge of the model's flow behavior, the **volumetric flow rate** can serve as a starting point for further calculations. It measures the volume of a fluid which passes the observed system per unit time. A basic formulation reads

$$Q = \dot{V} = u * A \quad (3.29)$$

Whereby u is the flow velocity in $\frac{m}{s}$, and A is the cross-sectional flow area in m^2 . When the mass flow rate is known, and the density can be assumed to be constant, the volumetric flow rate becomes

$$Q = \frac{\dot{m}}{\rho} \quad (3.29)$$

Since the change in velocity within a pipe is of primary interest, and also a basic measure for further fluid mechanical calculations, a basic formula – suitable for numeric iteration – has to be found. In a simple and yet used form of the simulation's solver engine, it reads

$$\Delta u = \left(\frac{1}{\rho_I} - \frac{1}{\rho} \right) * \frac{\dot{m}}{A} \quad (3.29)$$

Whereby

- ρ_I is the density at the internal node I , and
- ρ is the density at the reference point within the flow regime, e.g. the entrance or exit of a pipe section.

If the velocity of a fluid inside the pipe is small, streamlines will be in straight parallel lines. As the velocity of fluid inside the pipe gradually increases, streamlines will continue to be straight and parallel in accordance the pipe wall, until velocity is reached when the streamlines will waver and suddenly break into diffused patterns. The velocity at which this occurs is called *critical velocity*. At velocities higher than "critical", the streamlines are dispersed at random throughout the pipe.

The regime of flow when velocity is lower than critical is called *laminar flow*. At a laminar regime of flow, the flow velocity is highest at the pipe axis. Very close to the wall, velocity is equal to zero.

When the velocity is greater than critical, the regime of flow is called *turbulent*. Within turbulent regime of flow, there is irregular random motion of fluid particles in directions transverse to the direction on main flow. Velocity changes within a turbulent flow regime are more uniform than within a laminar one.

Within the turbulent flow regime of flow, there is always a thin layer of fluid at pipe wall which is moving in laminar flow. That layer is known as the *boundary layer* or laminar sub-layer. To be able to determine the state of flow regime, the Reynolds number is the key-parameter, being defined as

$$Re = \frac{\rho u L}{\mu} = \frac{u L}{\nu}, \quad (3.31)$$

Whereby

- μ is the dynamic viscosity in $\frac{kg}{m*s}$
- u is the flow speed in $\frac{m}{s}$,
- L is the characteristic linear dimension in m ,
- and ν the kinematic viscosity in $\frac{m^2}{s}$. [27]

Of great interest within the scope of this work are also the pressure losses Δp within the model's components. They heavily depend on the state of flow regime, due to viscous friction. Therefore, the pressure loss calculations of the model make use of the Reynolds number.

Within a laminar flow regime, the pressure losses due to viscous friction are:

$$\Delta p_{lam} = f_{shape} \frac{\dot{m} * \mu_I}{2 \rho_I * D_h^2 * S} * \frac{L + L_{eqv}}{2}, \quad (3.32)$$

where

- f_{shape} is the *shape factor for laminar flow viscous friction*, being dimensionless
- L_{eqv} is the *aggregate equivalent length of local resistances*, being dimensionless
- ρ_I is the density at the internal node in $\frac{kg}{m^3}$
- S is the cross-sectional area of the pipe in m^2
- D_h is the hydraulic diameter of the pipe in m
- μ_I is the dynamic viscosity at internal node in $\frac{kg}{m*s}$

Within a turbulent flow regime, the pressure losses due to viscous friction are:

$$\Delta p_{tur} = f_{Darcy} \frac{\dot{m} * \mu_I}{2 \rho_I * D_h^2 * S} * \frac{L + L_{eqv}}{2}, \quad (3.33)$$

whereby f_{Darcy} is the Darcy friction factor, computed through the Haaland correlation.

The Haaland equation is furthermore used to solve directly for the Darcy–Weisbach friction factor f_{Darcy} for a full-flowing circular pipe, [34].

A further elaboration on the correlation between (3.32), (3.33) and the Darcy-Weisbach equation is provided by the simulation software developer’s online documentation, as well other well-established literature resources, [35], [36].

When a fluid flow becomes choked within a constriction component, e.g. a gate valve or a pressure controller, the mass flow rate can be calculated most precisely by incorporating the value of sonic conductance into its function. In reference to the source code of the model’s gate valve, the function for the mass flow rate of a choked flow is

$$\dot{m}_{ch} = C \rho_0 p_{in} \sqrt{\frac{T_0}{T_{in}}} \quad (3.34)$$

whereby

- C is the sonic conductance inside the valve
- ρ is the reference gas density
- p is the absolute gas pressure at the component’s inlet
- T is the gas temperature at the inlet (in) or at standard conditions (0).

In 1989, the International Organization for Standardization published ISO 6358. **Sonic Conductance**, as defined by ISO 6358 is a valve-rating standard. It allows to determine the exact volumetric flow rate Q of a pneumatic component at any given differential pressure between input and output. Furthermore, *it provides the maximum achievable flow capacity* of the component and tells at what pressure ratio this happens. It is defined as

$$C(S) = \frac{S}{S_{max}} C_{max} \quad (3.35)$$

whereby

- C is sonic conductance
- C_{max} denotes the specified maximum value, provided by the manufacturer
- S is the effective flow area at constant choked flow
- S_{max} is the maximum effective flow area at constant choked flow

If a pneumatic equipment manufacturer provides the relevant data, it is possible to find the most suitable valve component for an application. Related approaches to parametrize the flow capacities of components are offered by using the flow capacity c_v .

The coefficient of flow c_v is a standard applied to determine the flow capacity of components *using water as the test fluid*. It reads

$$c_v = Q \sqrt{\frac{SG}{\Delta p}} \quad (3.35)$$

whereby

- Q is the volumetric flow rate in $\frac{gal}{min}$
- SG is the specific gravity of the fluid (for water = 1)
- Δp is the pressure drop across the constriction component in psi

Based on the water's substantially inherent properties, it is apparent that this method will not provide an accurate result for gases.

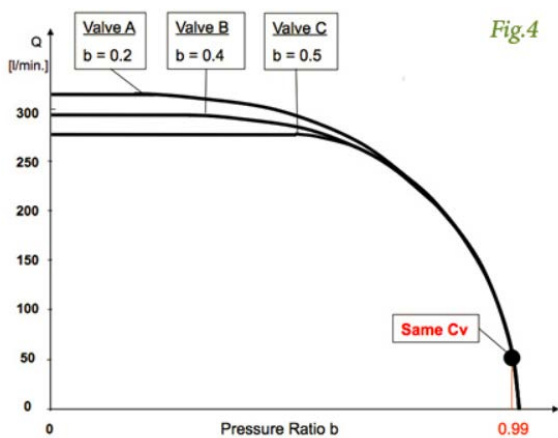


Figure 12: Influence of various critical pressure ratios on c_v at constant volumetric flow rates [37]

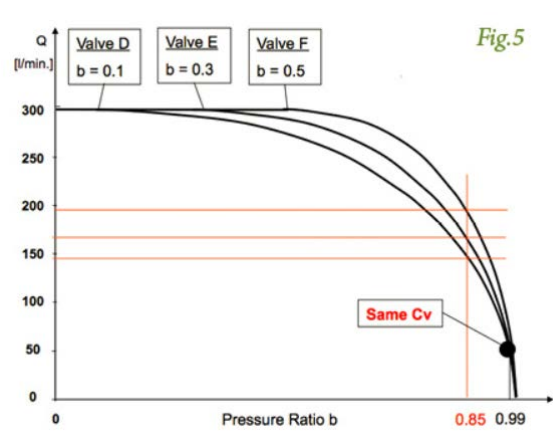


Figure 13: Influence of various critical pressure ratios on c_v at decreasing volumetric flow rates [37]

Figure 12 and 13 display the case of c_v , equaling three different numerical values for three different critical pressure ratios b within a certain range of volumetric flow rate Q .

The heat transfer throughout the fuel station model and all of its single components is of uttermost relevance as well. In the following subchapter, the central correlations of heat transfer and their application within the model's calculation methods shall be explained.

2.4 Heat transfer correlations

Fundamentally, heat transfer can be classified into four different mechanisms, which are

- Advection: The transport mechanism of any conserved quantity or material via bulk motion from one location to another, being dependent on motion and momentum of the fluid. This could be e.g. the transport of silt in a river, or energy or enthalpy within any fluid.
- Conduction: The transfer of energy between objects of solid matter which are in physical contact
- Convection: The heat transfer between a surface and either a liquid or a gas, being in motion.
- Radiation: The transfer of energy through the emission of electromagnetic radiation [38]

For our application of modelling heat transfer phenomena within a hydrogen fueling process, heat convection and conduction have to be analyzed to earn the desired model's level of explanatory power, while advection and radiation can be neglected without losing accuracy.

CONDUCTION CONVECTION RADIATION

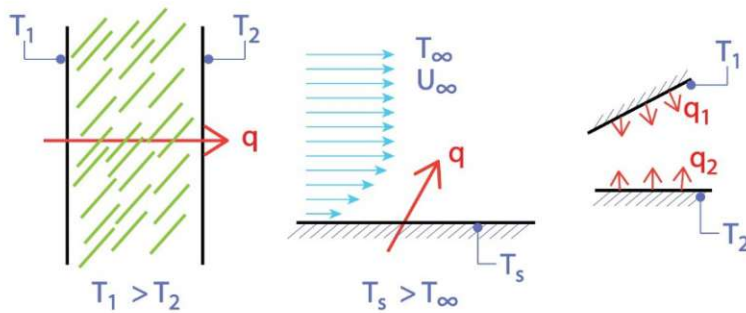


Figure 14: Overview of the three major modes of heat transfer, [39]

Heat conduction happens when adjacent atoms vibrate against one another, or as electrons move from one atom to another. Therefore, it is the most significant mechanism of heat transfer within a solid, or between solid objects in thermal contact.

The thermal output, delivered through heat conduction, is described by the correlation of **Fourier's law**. For a steady-state scenario with parallel wall areas of a solid body, it reads

$$Q = \lambda * A * \frac{T_{W1} - T_{W2}}{d} \quad (3.36)$$

whereby

- \dot{Q} is the transferred thermal output in W
- T_{W_1} is the temperature of the warmer wall area or surface in K
- T_{W_2} is the temperature of the cooler wall area or surface in K
- A is the area which is perfused by heat in m^2
- λ is the thermal conductivity coefficient in $\frac{W}{mK}$
- d is the thickness of the body, measured from wall to wall

For a one-dimensional case, Fourier's law reads

$$\dot{q}_x = -\lambda \frac{dT}{dx} \quad (3.37)$$

The thermal conductivity coefficient, commonly denoted by k or λ , is a measure of a material's ability to conduct heat. Although often treated as a material constant, its value can vary over a distinct range of temperatures for some common materials. At changes of phase or aggregate state, the value of the coefficients change significantly in most cases.

Thermal transmittance U is the rate of transfer of heat through matter, measured in $\frac{W}{m^2K}$.

Oftentimes also expressed as the U-value within civil engineering, it is primarily dependent on the heat transfer coefficient α between solid body and fluid, as well as the thermal conductivity λ and the geometry of the solid body.

In our model's exemplary case of heat transfer from flowing hydrogen through the different material layers of a cylindrical pipe wall, the thermal conductivity coefficient becomes [40]

$$k_a = \frac{1}{\frac{1}{\alpha_{out}} + \frac{d_{out}}{2\lambda} \ln \frac{d_{out}}{d_{in}} + \frac{d_{out}}{d_{in}} \frac{1}{\alpha_i}} \quad (3.38)$$

Whereby the indices of out and in refer to the outer and inner diameter of one of several pipe layers, as in Figure 15.

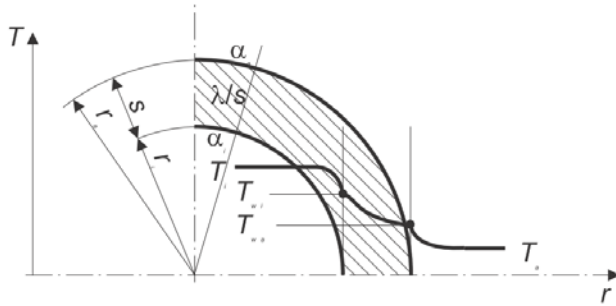


Figure 15: temperature profile of the heat transfer through a pipe wall [40]

A basic formulation for **convective heat transfer** is

$$\dot{Q} = \alpha A (T_f - T) \quad (3.39)$$

where

- \dot{Q} is the heat transferred per unit time in W
- A is the area of the object in m^2
- α is the heat transfer coefficient in $\frac{W}{m^2K}$, also denoted by h
- T is the object's surface temperature in K , and
- T_f is the fluid temperature in K .

Through the findings of Nußelt, heat transfer by contact of resting bodies and heat transfer between moving bodies are not distinct from each other. According to the Newton's law of cooling, the

heat flux is defined as [41]

$$\dot{q} = \alpha (T_1 - T_2) \quad (3.40)$$

Through integration of (3.37), it becomes evident that heat transfer by convection and conduction do not differ fundamentally, as integration delivers

$$\dot{q} = \frac{\lambda}{s} (T_1 - T_2) \quad (3.41)$$

Hence, for the case of heat transfer between resting bodies, the heat transfer coefficient α can be simplified to

$$\alpha = \frac{\lambda}{s} \quad (3.42)$$

In the case of heat transfer through convection, α can be formulated as

$$\alpha = \frac{Nu * \lambda}{d_i} \quad (3.43)$$

The Nußelt number Nu describes the influence of the state and the thermophysical properties of fluids on the heat transfer coefficient. The parameter d_i describes the definitive length of the body.

For forced, single phase turbulent flows, the correlation of Gnielinski delivers highly accurate results for the Nußelt number, and reads, [36]:

$$Nu = \frac{\frac{\xi}{8} * Re * Pr}{1 + 12.7 \sqrt{\frac{\xi}{8}} (Pr^{\frac{2}{3}} - 1)} \quad (3.44)$$

where

- $\xi = (1.8 \log_{10} Re - 1.5)^{-2}$, being equal to the Darcy factor f_{Darcy} in case of a forced single phase turbulent flow regime
- Pr is the Prandtl number

This correlation will be applied within the model's calculation code to approximate the heat transfer coefficient h_{coeff} for the convective heat transfer between the innermost pipe wall layer and the internal hydrogen flow. Its Simulink-integrated formula reads:

$$h_{coeff} = \frac{Nu * \lambda_{average}}{d_i} \quad (3.45)$$

3. Basic fueling procedures & technologies

3.1 Procedures of fueling

Fueling of compressed gaseous hydrogen into a vessel can be achieved by two basic procedures:

- The direct compression from a lower pressure tank into a high pressure vehicle tank
- The use of a feedback controlled non-steady flow process, letting hydrogen flow from a higher pressure storage tank into the vehicle tank

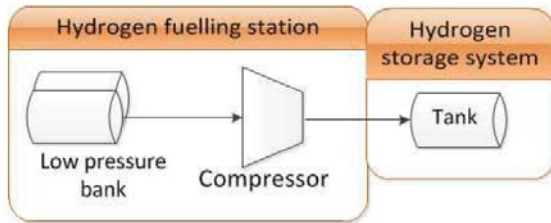


Figure 16: Simple sketch of direct compression fueling [42]

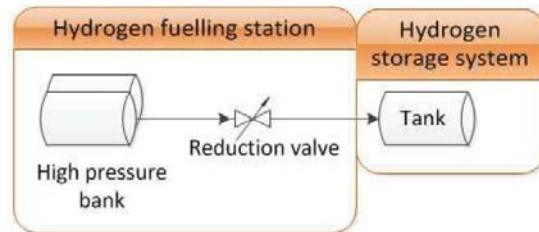


Figure 17: Simple sketch of fueling through the usage of a pressure gradient [42]

Because the pressure-gradient fueling method is the central technology of the manufacturer's product range, this method will be explained in depth.

The alternative procedure of fueling cryogenic liquid hydrogen into a vessel shall be outlined separately in subchapter 3.1.5.

3.1.1 Fueling station designs

Among fueling plants, using the pressure-gradient method, two variants of plant designs do exist:

- Single-stack system – also denoted as single tank storage design
- Multiple-stack Cascade – also denoted as cascade tank storage design

The variant of single tank-to-tank fueling has the single difference in using one high pressure storage bank for the whole fueling station, while the cascade design uses between at least three to nine, or even more high pressure storage banks.

Among several thermodynamic minor advantages, storing the hydrogen at a high pressure in only one tank requires a significantly large high-pressure storage tank. These high-pressure hydrogen storage tanks become more expensive and therefore unrealizable at a certain demand of fueling procedures per time measurement.

An improvement of the single-tank storage system is the multiple-stack storage system, as will be explained in 3.1.3. Figure 18 shows the basic scheme of a multiple-stack fueling station design. Exemplifying the central plant components, as well as their interconnection within the plant design, this scheme can be classified as the most established process scheme of today's commercial design efforts.

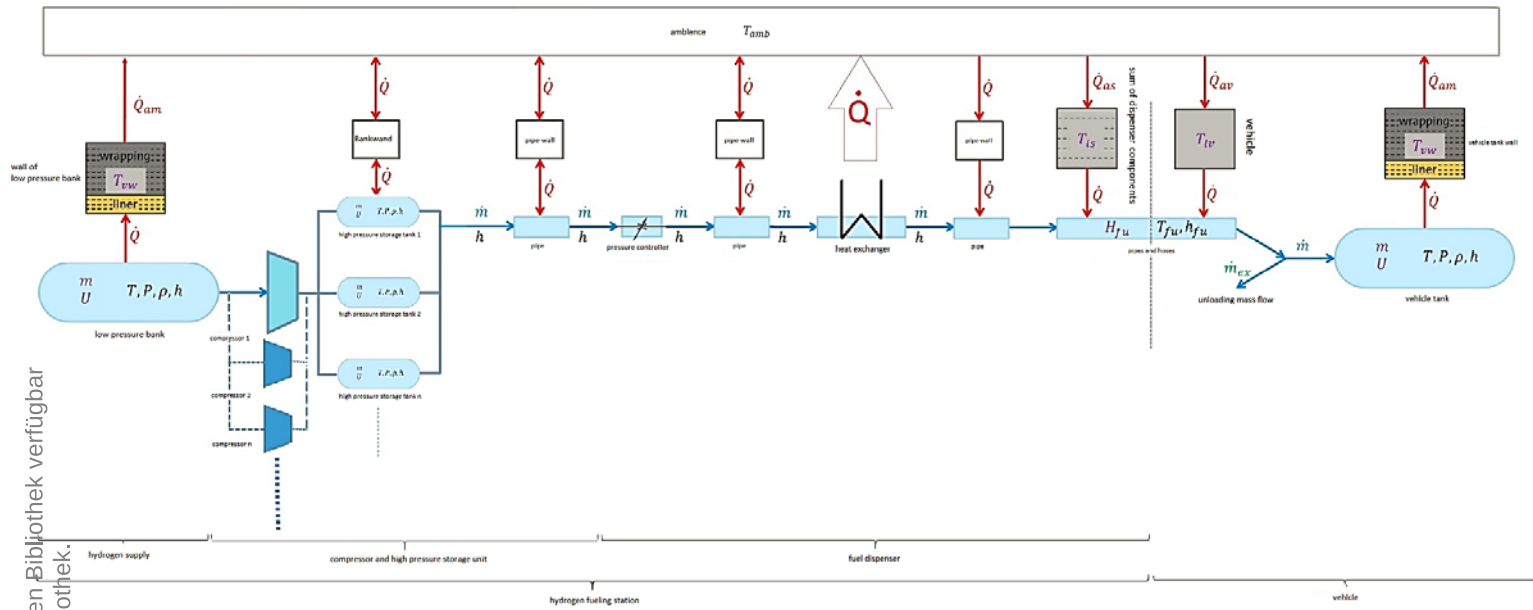


Figure 18: Basic process scheme of the commercially established multiple-stack system

As shown in figure 18, the following plant components cannot be ignored, and fulfill central functions within a standard commercial hydrogen fueling procedure:

- High pressure storage tanks – also being referenced as “Compressed Hydrogen Storage System”, CHSS, together with appendant safety valves
- Pressure controller
- Heat exchanger
- Dispenser
- Vehicle tank
- Pipes, connecting all above mentioned components

An explanation of the underlying fueling standard shall be undertaken, together with the functions of every single component.

3.1.2 Hydrogen fueling protocols

Within the last 40 years, several independent technical standards have been elaborated for the application of gas fueling processes. Certain standards have to be fulfilled, in order to fulfill the legal and safety requirements for a hydrogen fueling process. These are the European pressure Norm EC79/2009 and ISO 26262 for functional safety, [14].

As the result of 12 years of work, the Society of Automotive Engineers SAE published the most comprehensive hydrogen fueling standard for light duty vehicles, denoted as SAE J2601. When following the fueling protocol SAE J2601, all safety demands of a fueling process are met, and the expected time frame of one fueling procedure can be met, [43].

It is most reasonable to begin explaining the content of SAE J2601 by firstly explaining the demands of the vehicle which shall be refueled. These are the demands of the car, approaching a hydrogen fueling station:

- Achieving an expectable fueling time of 3 minutes or less.
- Achieving a target state of charge, SOC, very close to 100%, which is defined as

$$SOC = \frac{\rho(p, T)}{\rho(NWP, 15^{\circ}C)} * 100\% \quad (3.46)$$

Whereby NWP is the *nominal working pressure*. By definition, NWP is the vehicle tank pressure at a uniform gas temperature of 15 °C and 100% SOC, specified by the tank manufacturer.

Within SAE J2601, only two categories of NWP are used, being 35 MPa and 70 MPa, as explained in more detail in the paragraph below.

- Executing the fueling process without overrunning the five universal safety limits, which are

- ❖ A *maximum target density*, according to the pre-determined dispenser precooling temperature, and the NWP. Being acknowledged by the SAE as the reference parameter setup (as explained below), the target density would be $40.2 \frac{g}{cm^3}$.
- ❖ A lower and an upper temperature limit of -40 °C and 85 °C, measured close to the socket of the vehicle tank, for avoiding thermal stress damage to the vehicle tank.
- ❖ A maximum mass flow rate of $0.06 \frac{kg}{s}$, measured close to the the socket of the vehicle tank.
- ❖ A maximum operating pressure MOP, determined as $1.25 \cdot NWP$. It is the highest gauge pressure of a component or system that is expected during normal operation including starts, stops, and tank switching.
- ❖ Deviating from the determined pressure ramp rate by intersecting with either the upper or lower boundaries of the pressure tolerance corridor (explained in subchapter 3.1.4).

The station's *fueling protocol category* will be defined by the vehicle's nominal working pressure NWP and the station's fuel delivery temperature category. The category is denoted by the letter H, followed by the value of nominal working pressure in MPa, and the letter T, followed by the absolute value of the fuel delivery temperature category in °C. For example, H70-T40 is the station category for a hydrogen fueling protocol with a NWP of 70 MPa and a fuel delivery temperature category of -40 °C.

Table 1 illustrates the fuel delivery temperature categories per pressure classes.

Fueling delivery temperature category		$-33^{\circ}\text{C} \leq T_{\text{fuel}} \leq -26^{\circ}\text{C}$	$-26^{\circ}\text{C} \leq T_{\text{fuel}} \leq -17.5^{\circ}\text{C}$	$-17.5^{\circ}\text{C} \leq T_{\text{fuel}} \leq -2.5^{\circ}\text{C}$
Station designator	35 MPa NWP	H35-T40	H35-T30	H35-T20
	70 MPa NWP	H70-T40	H70-T30	H70-T20

Table 1: Fuel delivery temperature categories per pressure classes

The fueling time can vary widely, depending on ambient temperature, initial pressure levels and volumes of the high-pressure storage unit, final SOC and other conditions. In order to establish a fueling time goal for a frequently appearing fueling scenario, the SAE agreed to define the parameters of a "reference" fueling:

- Dispenser Category = H70-T40
- Ambient Temperature = 20°C
- Initial CHSS Pressure = 10 MPa
- Final SOC = 95%

All limits combined constitute an operating range for the fueling process, as exemplified in figure 19 for the reference parameter scenario.

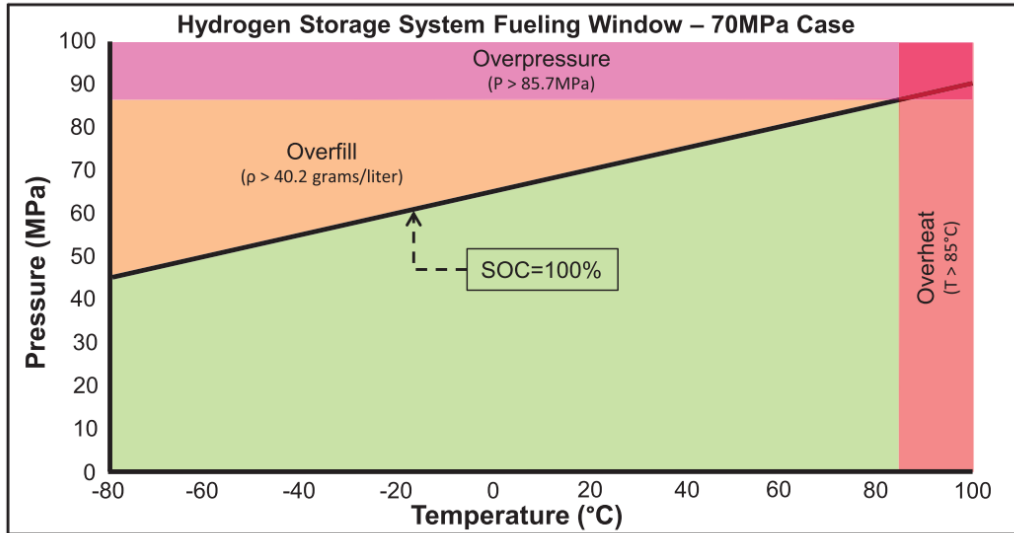


Figure 19: Operating range of an H70-T40 reference parameter scenario [43]

Depending on the vehicle and the station, the fueling can proceed either with or without communication between the station and the vehicle, being denoted as *communication method* or *non-communication method*.

3.1.2.1 Non-communication method

The **non-communication method** works as follows:

1. The initial vehicle tank temperature is assumed equaling the ambient station temperature, unless measurable directly inside the vehicle tank
2. An impulse of a known amount of hydrogen is sent into the vehicle tank
3. The subsequent pressure increase is measured
4. Vehicle tank volume and maximum mass capacity of the vehicle tank are calculated through basic thermodynamic approaches, as introduced in chapter 3.1.2.
5. At this point, all necessary parameters are known for using the SAE **look-up tables**. These are:
 - Maximum mass capacity of the vehicle
 - “Fuel delivery temperature” or initial tank temperature, assumed being equal to the ambient station temperature
 - The appropriate dispenser category, being dependent on maximum mass capacity of the vehicle tank, and fuel delivery temperature

- These tables provide the appropriate *Average Pressure Ramp Rate*, **APRR**, and target pressure. An appropriate target density is then calculated and furtherly used by the PLC algorithm as one of the three abovementioned safety limit parameters.

The *average pressure ramp rate* **APRR** is the pressure rise over a constant time frame. During the fueling period, the station applies a pressure, targeting an Average Pressure Ramp Rate value, based on the derived values within the Look-up tables. The APRR is given a tolerance in which it can deviate and nevertheless reach the target SOC, as depicted in figure 20.

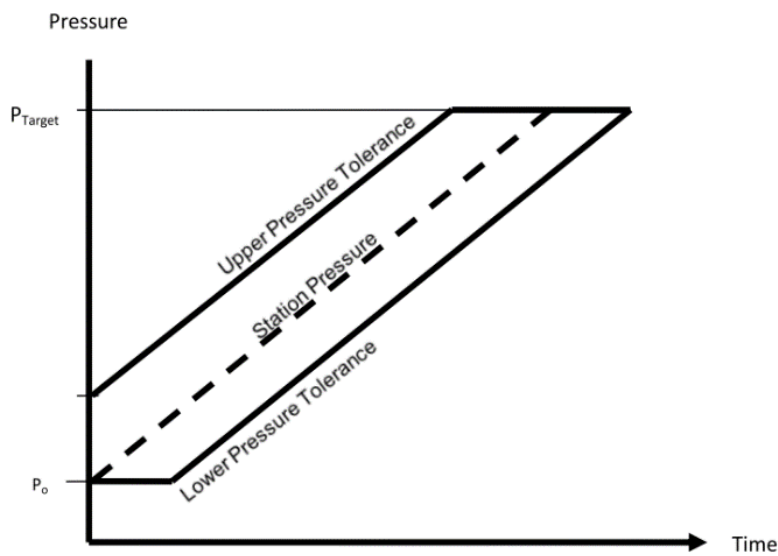


Figure 20: APRR boundaries and the pressure tolerance corridor [43]

Especially for the applications of non-communication fueling, extensive modeling work has been done by the SAE to develop a series of **parameter look-up tables** that optimize the fueling process while ensuring that the refueling demands are being met.

In attunement with the fuel delivery temperature, the vehicle tank's maximum mass capacity and the dispenser category, the station chooses a suitable look-up table, stored within the PLC unit, and reads an appropriate APRR out of the look-up table. In the following, the station will fuel along the APRR until the look-up table target pressure is reached. Figure 21 shows the look-up table for the reference conditions mentioned above.

H70-T40 4-7kg non-comm	APRR [MPa/min]	Target Pressure, P_{target} [MPa]											
		Initial Tank Pressure, P_0 [MPa]											
		0,5	2	5	10	15	20	30	40	50	60	70	> 70
> 50	no fueling	no fueling	no fueling	no fueling	no fueling	no fueling	no fueling	no fueling	no fueling	no fueling	no fueling	no fueling	no fueling
50	5,1	77,8	77,6	77,3	76,9	76,6	76,2	75,7	75,3	74,7	73,9	72,8	no fueling
45	8,1	76,3	77,2	76,9	76,5	76,4	76,2	75,6	75,3	74,7	73,9	72,7	no fueling
40	11,5	73,2	75,6	76,8	76,3	76,4	76,2	75,6	75,3	74,6	73,9	72,7	no fueling
35	12,4	72,9	75,3	76,4	76,0	76,1	75,9	75,3	75,1	74,5	73,8	72,7	no fueling
30	15,3	70,6	73,9	75,8	75,2	75,4	75,1	74,3	74,1	73,3	72,4	71,3	no fueling
25	18,5	69,0	72,8	75,1	74,5	74,7	74,3	73,3	73,0	72,0	71,1	no fueling	no fueling
20	21,8	67,9	72,1	74,5	73,7	74,0	73,4	72,2	71,9	70,7	69,7	no fueling	no fueling
10	28,0	66,3	71,1	74,1	73,2	72,4	71,6	70,9	69,6	68,4	66,9	no fueling	no fueling
0	28,5	74,0	73,4	72,4	70,6	70,7	69,6	68,6	67,1	65,7	64,0	no fueling	no fueling
-10	28,5	73,4	72,9	71,9	70,0	70,0	68,4	66,5	64,4	62,9	61,2	no fueling	no fueling
-20	28,5	72,9	72,3	71,3	71,0	69,5	68,0	65,7	62,4	60,0	no fueling	no fueling	no fueling
-30	28,5	72,1	71,6	70,6	70,4	69,0	67,4	65,2	61,8	58,7	no fueling	no fueling	no fueling
-40	28,5	71,6	71,1	70,2	70,0	68,5	66,9	64,8	61,5	58,5	no fueling	no fueling	no fueling
< -40	no fueling	no fueling	no fueling	no fueling	no fueling	no fueling	no fueling	no fueling	no fueling	no fueling	no fueling	no fueling	no fueling

Figure 21: Look-Up Table example for the reference case according to SAE J2601 [43]

3.1.2.2 Communication method

The **communication method** functions as follows:

Communications Fueling provides a valid data connection, based on infrared communications (IrDA), between the FCEV and the hydrogen fueling station. As being outlined in the underlying technical standard SAE J2709, unidirectional wireless communications between the FCEV and the hydrogen station measure the temperature and high-pressure storage tank volume continuously. The average pressure rate therefore becomes the feedback variable and becomes adapted to the continuously compared reference pressure ramp rate.

Figure 22 illustrates an overview of the SAE J2799 standard for Infrared communications between the FCEV and the Hydrogen Station.

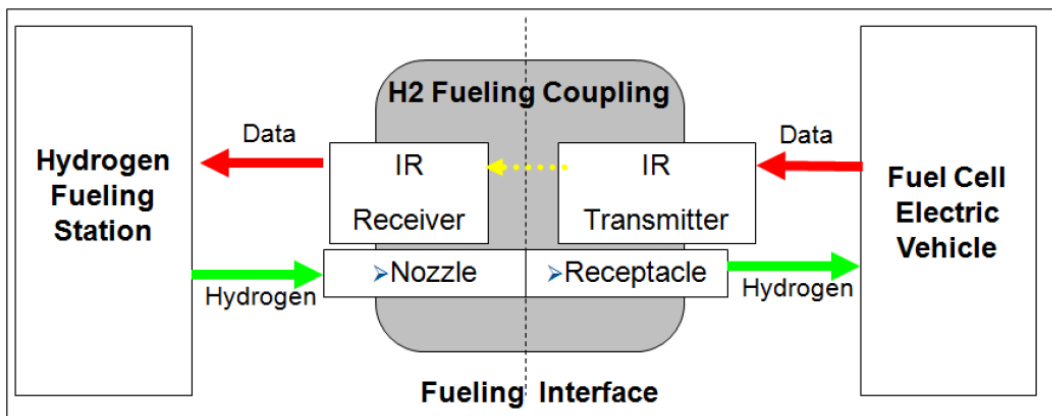


Figure 22: Process scheme of the signal flow within communications fueling [43]

Figure 23 shows a flow diagram of an exemplary non-communication fueling procedure.

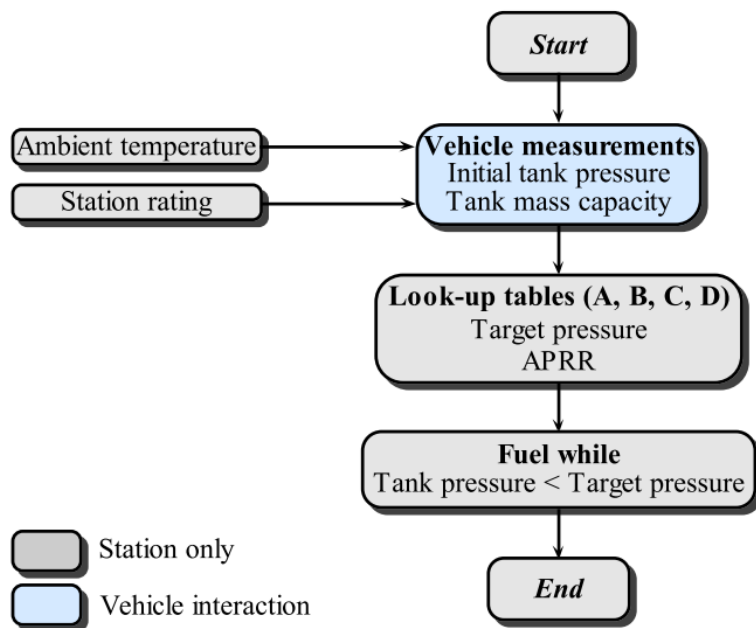


Figure 23: Procedure scheme for the “Non-Com” case [44]

3.1.3 Thermodynamics aspects & stop criteria

The following thermodynamic phenomena can be observed throughout the whole flow process, and have to be controlled as strict as possible in order to guarantee a paramount level of safety standards:

- Warming inside the vehicle tank, due the compression work taking place inside
- Heat transport from the hydrogen flow through every component layer of a pipe or vehicle tank
- Warming of the hydrogen flow at the exit of the pressure controller, heating up when throttled
- Warming of the hydrogen flow inside the pipes, due to friction and flow resistance, which is negligible for further investigations

As already described in other words and contexts above, the possibilities of providing uttermost levels of safety and control during a fueling procedure can be summed up in two plans of action:

1. An exact forecast of the temporary pressure and temperature development of the hydrogen inside the vehicle tank during fueling
2. A standardized fueling procedure

In case of deviating of the aimed course of fueling, so-called stop criteria, as already introduced in 3.1.2, serve as criteria to abort a fueling process instantly.

3.1.4 Cascade tank switching

A “multi-stack” fueling station, or cascade-tank storage system usually consists of one high-, one medium- and one low-pressure tank at pressures around 90-100, 60-70 and 40-50 MPa, respectively. Although, certain plants make use of up to 9 cascade storage tanks. When a vehicle connects to the station, the station starts fueling from the low-pressure tank.

Fueling continues until the pressure in the low-pressure tank becomes insufficient to maintain the APRR.

At this point, the station switches to the medium-pressure tank and the refueling proceeds. When the pressure in the medium-pressure tank is not sufficient to comply the APRR either, the station starts refueling from the high-pressure tank.

So, why is a design of multiple high pressure storage tanks firsthand considered to be useful?

Typically, in a single-tank storage system, the *throttling loss across the reduction valve is measurably significant* while complying with the APRR for the most part of the refueling period.

Hence,

- The throttling loss across the reduction valve causes a larger temperature increase, thus requiring a higher cooling demand, provided by increased heat exchanger performance.
- Furthermore, in a tank-to-tank refueling design, the storage tanks must be refilled with hydrogen from a separate low-pressure storage after each vehicle fueling procedure. This implies that the station requires a certain period of time to recover before a new refueling can be started. Thus, the customer may have to wait for the storage tanks to be refilled before he or she can refuel.
- Furthermore, storing the hydrogen at a high pressure in only one tank becomes rather expensive for reasonable sizes of hydrogen fueling stations, as already mentioned in 3.1.1.

Hence, the advantage of the cascade storage system becomes obvious.

- + Using several tanks of variable pressure levels results in a lower throttling loss across the reduction valve. This means that the entropy generation becomes less, compared to the single-tank storage design.
In other words, less of the compressor work used to achieve the high pressures in the tanks is going to be wasted.
- + In addition to that, a lower throttling loss across the valve results in a lower temperature increase, therefore requiring less cooling demand in the heat exchanger.

During a hydrogen fueling procedure, the APRR is supposed to progress within the predetermined pressure tolerance levels. An “intersecting” with either the upper or lower pressure ramps directly

leads to the instantaneous abortion of the fueling process. Therefore, all tank switching phases have to be held as short as possible. Longer periods of non-fueling time within one fueling procedure for the same car can trigger erroneous abortion signals, and therefore lead to interruptions of the overall fuel station's operational readiness.

A preassigned 5 second buffer phase is tolerated by SAE J2601 for letting the pressure controller readjust in case of a non-fueling phase. Figure 24 shows a fueling procedure for the fueling of one vehicle, while the non-fueling phases of the cascade tank switching remain short enough not to trigger an abortion signal.

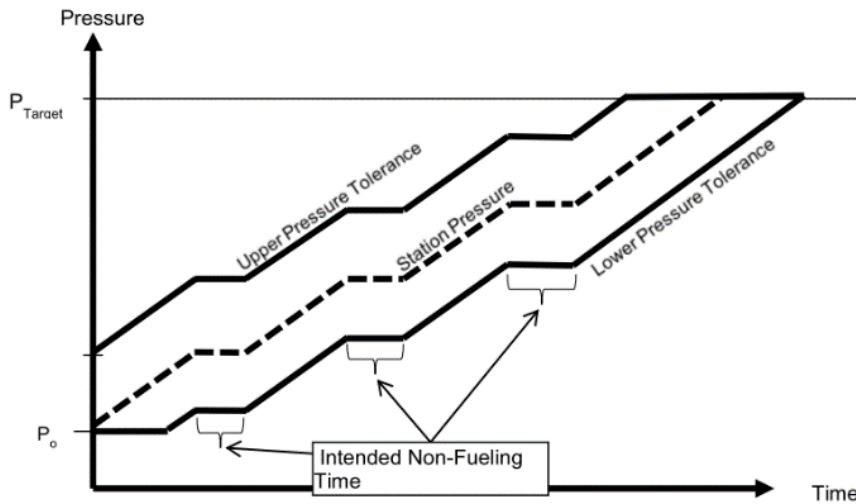


Figure 24: Course of an APRR within the pressure tolerance corridor and cascade tank-switching events [43]

Figure 25 shows the pressure development versus time over a complete fueling cycle, including non-fueling times and course deviations of the pressure ramp rate.

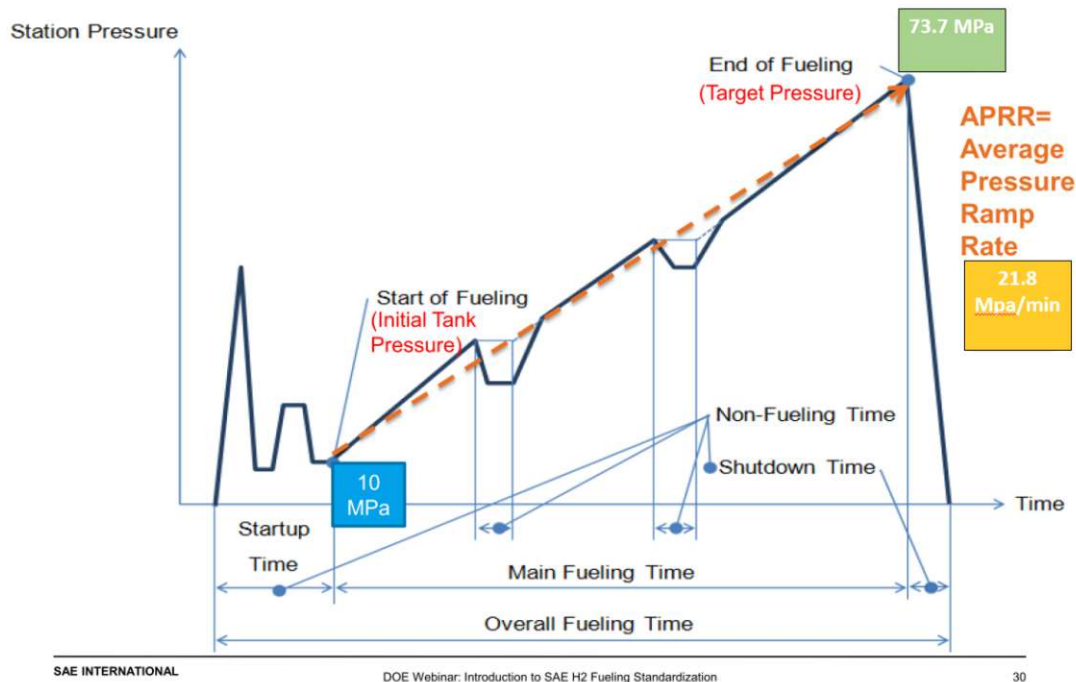


Figure 25: Fueling pressure gradient versus time of a complete fueling cycle [45]

3.1.5 Cryotechnology

It is not possible to fuel a vehicle with LH₂. Only by switching its aggregate state to supercritical, the vehicle tank can be fueled with supercritical CcH₂, being the product of gradually expanded and heated LH₂. [25] [2]

The procedure of fueling liquid hydrogen LH₂ can be summarized by the following process steps:

1. Liquid hydrogen is stored between 0.2 and 0.35 MPa, below 33.1K and at vessel volumes between 400 and 4000 kg H₂ within a so-called cryotank.
2. With the start of a fueling procedure, the liquid hydrogen flows through the so-called cryopump, being compressed up to 90 MPa within two compression stages. Thereby, the hydrogen reaches its *supercritical aggregate state* CcH₂.
3. Next, the then cryo-compressed hydrogen CcH₂ becomes heated by an air and an electric heat exchanger, connected in series.
4. After passing the pressure controller, it arrives within the target temperature range of 233-240K at the dispenser nozzle.

The fueling procedure for cryogenic liquid hydrogen CcH₂ shows higher energy efficiency rates and lower distribution costs, in case of large-scale demands of hydrogen. Reason for this is hydrogen's significantly higher energy densities in its liquid aggregate state, as already explained within subchapter 3.1.2. Therefore, saved costs regarding storage space, transportation space and

compression energy can be leading factors for favoring the fueling of hydrogen in its cryogenic liquid state, [25]

Within subchapters 3.1.2, 3.1.3 and 3.1.4, the essential knowledge and correlations of standard hydrogen fueling procedures have been outlined.

In the following chapter, the approach within modelling and simulation – central elements of the scope of this work - shall be explained.

4. Model description

In the introductory paragraphs of this chapter, a definition of the term *computer model* and *computer simulation* shall be given, as well as its subordinate term of *thermodynamic model*.

According to Mathworks'® MatLab-Simulink online documentation, a **computer model** is an abstract and yet simplified description of a system, capturing the behavior of the underlying real-world system, using *mathematical* equations, algorithms and diagrams, [46].

It becomes obvious that a **thermodynamic model** must therefore use thermodynamic equations beside mathematical fundamental correlations to display the behavior of a thermodynamic system. The underlying equations define the relationships between elements of the modeled system and attempt to display the concurrent action within the system. This could be a state of thermodynamic equilibrium, or the process to reach equilibrium.

The modelling of a real-world plant through thermodynamic equations requires simplifications and assumptions in order to be able to display meaningful behavior. These should be only as constraining as necessary to gain the desired level of accuracy, compared to expectable real-world experimental results. The assumptions made within this scope of work are listed in 4.2.

The object and aim of all thermodynamic modelling should be the achievement of predefined modelling aims, as described within subchapter 1.2 for the scope of this work.

A **computer simulation** is the execution of a computer program that contains all of the underlying model's equations and algorithms. Simulation, therefore, is the process of *predicting* the behavior of the appropriate model.

The execution of the program can be understood assigning the computer tasks of numerical approximation work. The so-called interpreter - a computer program itself of the superior computer program then has to choose between either direct or iterative mathematical methods to approximate solutions for linear algebraic or even (partial) differential equations.

There are many different types of computer simulation, The common feature they all share is the attempt to generate a sample of representative scenarios for a model, in which a complete enumeration of all possible states would be prohibitive or impossible.

The type of simulation program used within this work is a continuous dynamic simulation of a thermodynamic non-steady flow process.

4.1 Possibilities of MatLab, Simulink and Simscape

MatLab is a multi-paradigm numerical computing environment and proprietary programming language developed by MathWorks Inc. Most fundamentally, it offers

- matrix manipulations,
- plotting of functions and data,
- implementation of algorithms, creation of user interfaces, and
- interfacing with programs, written in other languages.

Although MatLab is intended primarily for numerical computing, optional toolboxes allow access to symbolic computing abilities.

Simulink is a MatLab-integrated *graphical programming environment* for modeling, simulating and analyzing dynamic multidomain systems. An integrated customizable block library and a graphical block diagramming tool together build the graphical user interface. Furthermore, the Simulink Add-Ons can

- either execute MatLab codes or be scripted from it.
- can automatically generate “C” source code for real-time implementation of systems
- create code for the use in independent embedded systems (“Embedded Coder” Ad-On)
- test physical systems via real-time computing (“Simulink Real-Time”),

among other currently emerging Add-Ons.

The most fundamental element of a MatLab-Simulink thermodynamic model is a so-called **block**, which shall resemble any considerable physical plant component, e.g. a vessel or a valve. The functionality of a single block is defined by multiple thermodynamic equations, being embedded within its source code. The sum of these equations are represented as block methods. These block methods are executed during the execution of a block diagram within a loop. Each passed cycle represents the evaluation of the block diagram at a certain point in time.

Simscape™ is a MatLab tool that employs a physical network approach. Thereby, blocks correspond to physical elements, such as pumps, motors, and op-amps. The lines which join these blocks resemble physical connections – e.g. pipes, cables – and deliver matter, energy or any kind of signal-based information.

Connecting the blocks results in MatLab-Simulink’s designated **physical component models**, as exemplified in figure 26. This approach makes it possible to describe the physical structure of a thermodynamic system, rather than the plain underlying thermodynamic correlations, [47].

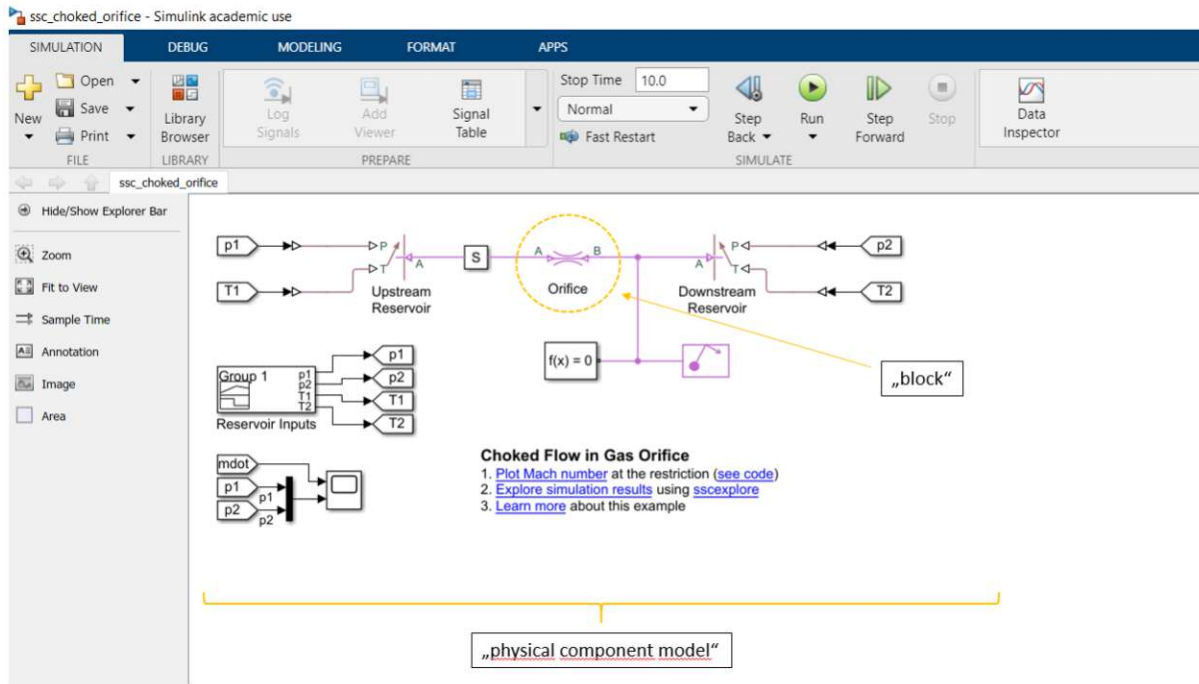


Figure 26: Example of a physical component model of a basic gas system on the Simscape GUI

4.2. Thermodynamic properties library

Modelling and simulation of thermodynamic systems, such as hydrogen fueling stations, requires access to the **fluids' thermodynamic properties**. A considerable number of independent thermodynamic property libraries is available for MatLab-Simulink. The library used in this work is *RefProp*, a fluid properties database first published by the National Institute of Standard and Technology in 1995. It requires a license and can be used of various software environments as a standard ".ddl" library file, which then needs a wrapper for integration into the environment used. [48]

An accurate model requires the largest ranges of pressure and temperature in the shape of vectors or two-dimensional arrays to be able to display a desired level of realistic fluid behavior. [49] MatLab can request thermodynamic property values from RefProp and furthermore structure and deposit all received property values.

Because the simulation shall display the most realistic behavior of hydrogen possible, Simscape therefore requires vector fields of specific thermodynamic properties, e.g. the dynamic viscosity μ or the specific enthalpy h . In figure 27, a vector field of the heat capacity at constant pressure c_p has been plotted by MatLab, in order to visualize its dependence on the predefined vector fields of pressure and temperature.

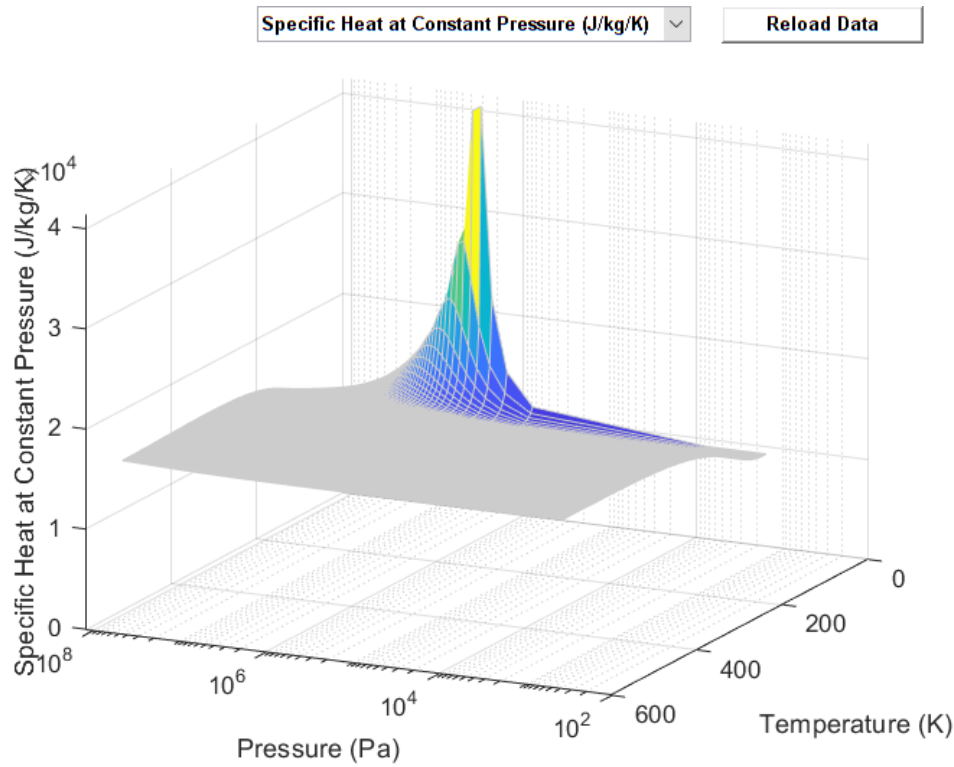


Figure 27: Vector field of c_p as a function of pressure and temperature

4.3 Structure of the model

The components connected in their corresponding order result in the thermodynamic computer model. In figure 28, a GUI snapshot of the model of this research project's hydrogen fueling station can be seen.

Explaining the function of every single block's algorithm component would only overburden this work with information. The overall functioning and behavior of the whole model can be explained best by dividing the model into four subcategories of component blocks, and explaining their intended purpose, functioning and expectable behavior as units:

- Gas flow unit
- Heat transfer unit
- Controller unit
- Tank switching mechanism unit

The entity of block components used within this model are namely:

Simscape Foundation Library – Gas domain components	
Gas properties for gas systems	Local restriction for gas systems
Solver configurations element	Mass&energy flow rate sensor for gas systems
Constant volume chamber for gas systems	Pressure&temperature sensor for gas systems
Gate valve for gas systems	Thermodynamic properties sensor for gas systems
Check valve for gas systems	Absolute reference for gas systems
Pipe for gas systems	

Simscape Foundation Library – Thermal domain components	
Convective heat transfer element	Thermal mass
Conductive heat transfer element	Temperature source

Simulink components of various Simulink sub-libraries	
Constant element	PID “1 Degree of freedom” element
Gain element	Interval test dynamic element
Compare to constant element	Data type conversion element
Clock element	Logical operator element
Scope element	Terminator element
Memory element	S-R Flip Flop element
Simulink – Physical Signal Converter	Assertion element
Physical Signal – Simulink Converter	Transport delay element

Table 2: List of utilized Simscape and Simulink block components

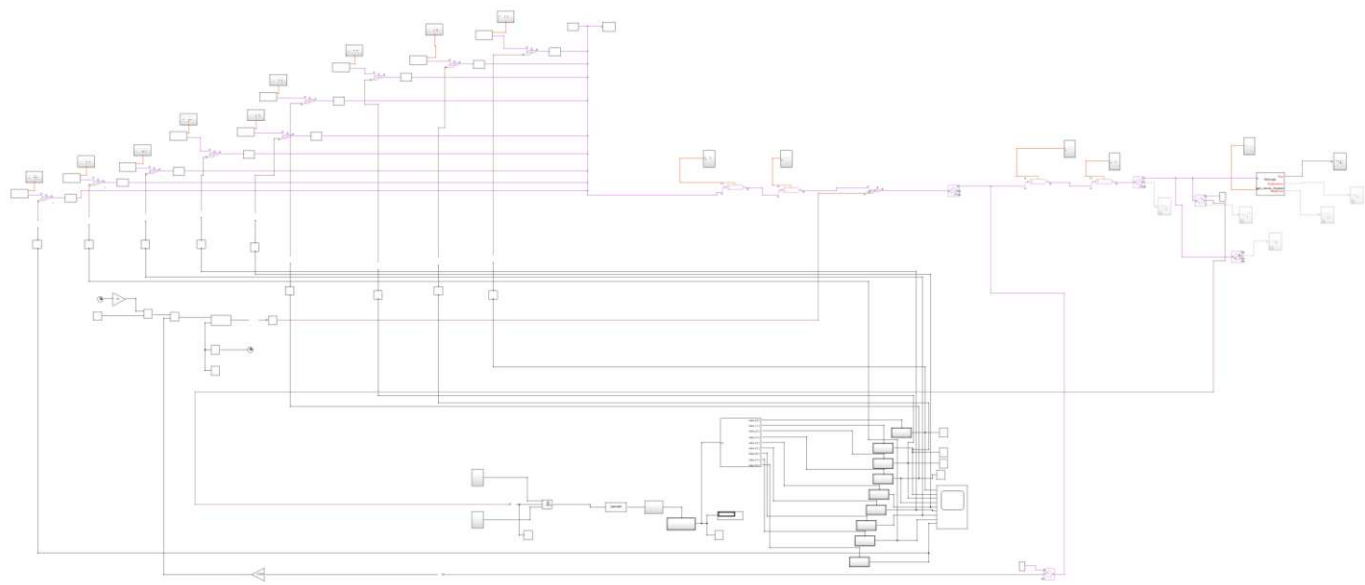
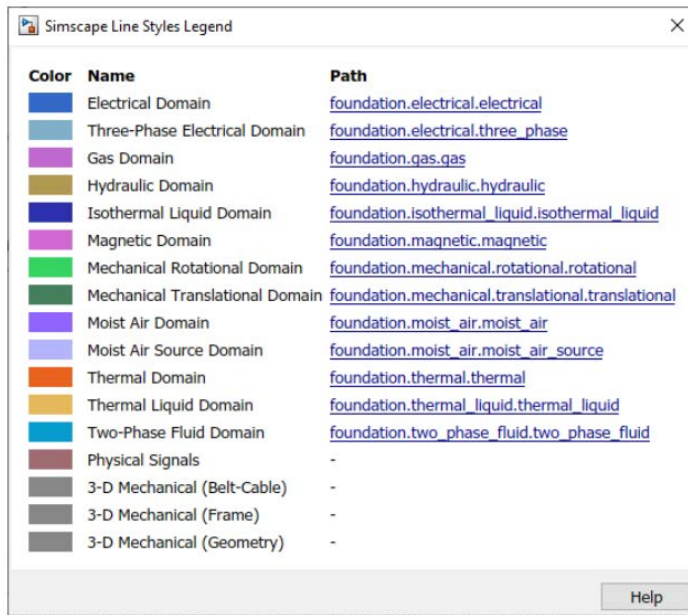


Figure 28: Global GUI's view on the hydrogen fueling station's model

Simscape Domains describe the physical domains through which component blocks exchange energy and data. Each domain uses its own *port type* and appropriate line style for the *physical signal lines*, distinguishing itself visibly from other domains.

The gas flow unit is part of the gas domain, and communicates its physical unit-based information via purple-colored physical signal lines. Figure 29 provides an overview on all Simscape domain-specific line styles.




















Color	Name	Path
	Electrical Domain	foundation.electrical.electrical
	Three-Phase Electrical Domain	foundation.electrical.three_phase
	Gas Domain	foundation.gas.gas
	Hydraulic Domain	foundation.hydraulic.hydraulic
	Isothermal Liquid Domain	foundation.isothermal_liquid.isothermal_liquid
	Magnetic Domain	foundation.magnetic.magnetic
	Mechanical Rotational Domain	foundation.mechanical.rotational.rotational
	Mechanical Translational Domain	foundation.mechanical.translational.translational
	Moist Air Domain	foundation.moist_air.moist_air
	Moist Air Source Domain	foundation.moist_air.moist_air_source
	Thermal Domain	foundation.thermal.thermal
	Thermal Liquid Domain	foundation.thermal_liquid.thermal_liquid
	Two-Phase Fluid Domain	foundation.two_phase_fluid.two_phase_fluid
	Physical Signals	-
	3-D Mechanical (Belt-Cable)	-
	3-D Mechanical (Frame)	-
	3-D Mechanical (Geometry)	-

Figure 29: List of available domains and its assigned line styles

4.3.1 Gas flow unit

The gas flow unit displays the transport of hydrogen as a pressure-gradient based non-steady flow process in the flow direction “cascade storage tanks” towards “vehicle tank”.

The flow process begins by gradually opening a gate valve, positioned after a check valve and one of multiple available high pressure storage tanks. The gate valve acts upon its information received from the “tank switching logic unit” at its in-built physical signal input port. The check valve serves as a security device so that the hydrogen can only flow out of a high pressure tank during fueling the process of cascade fueling.

The *gas properties* block enables the adjustment of gas behavior and connecting Simulink with appropriate gas property vector fields.

The solver configuration block gives access to a part of Simulink’s available settings regarding the choice and set-up of the used solver method. The entity of all solver settings can be found within Simulink’s menu item *model settings*. Both the blocks gas properties and solver configurations are

the only two blocks required as being connected to the model for a simulation's successful work flow.

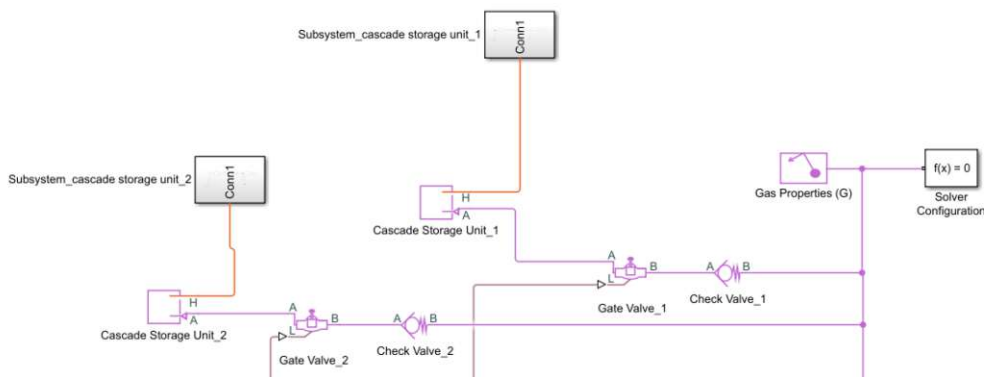


Figure 30: Cascade storage tanks, check valve, gate valve, gas properties block and solver configurations element, structured within the model's expectable flow direction

After passing the gate valve, the hydrogen continues flowing downstream. Hence, it passes the pipe sections “bank control” and “dispenser line” before entering the pressure controller. The pressure controller is a restriction valve. It receives information from a PID controller, and takes on the role of the actuator within model's “controller unit”.

The throttled hydrogen flow then leaves the pressure controller and passes the heat exchanger – submitting the gases' stored heat, generated by throttling, to the heat exchanger. The central responsibility of the heat exchanger is to cool down the throttled and therefore heated hydrogen flow to the fuel delivery temperature. This temperature is the dispenser entrance temperature, and can be read directly out of the fueling protocol category, as already mentioned in 3.1.2. For example, the corresponding fuel delivery temperature of the H70-T40 category is -40 °C.

The commercial plant's heat exchanger is a combination of a solid body cooling unit and a shell and tube heat exchanger, called “aluminum cold fill” unit.

As sketched in figure 31, a cast aluminum block contains 4 pipes, leading the cooling agent, and 2 pipes, leading the hydrogen flow. The cooling energy, stored by the aluminum block, is transferred through the pipe walls to the hydrogen flow.

The component block modelling the ACF uses the Simscape component block of a pipe, taking up the function of a plate heat exchanger. The pipe is simply wrapped inside a layer of aluminum, being in constant supply of cooling power. The aluminum layer sustains an average temperature of 233K constantly. The cooling power is delivered by an ideal cooling power source, called “temperature source”, a component of the Simscape “thermal” domain.

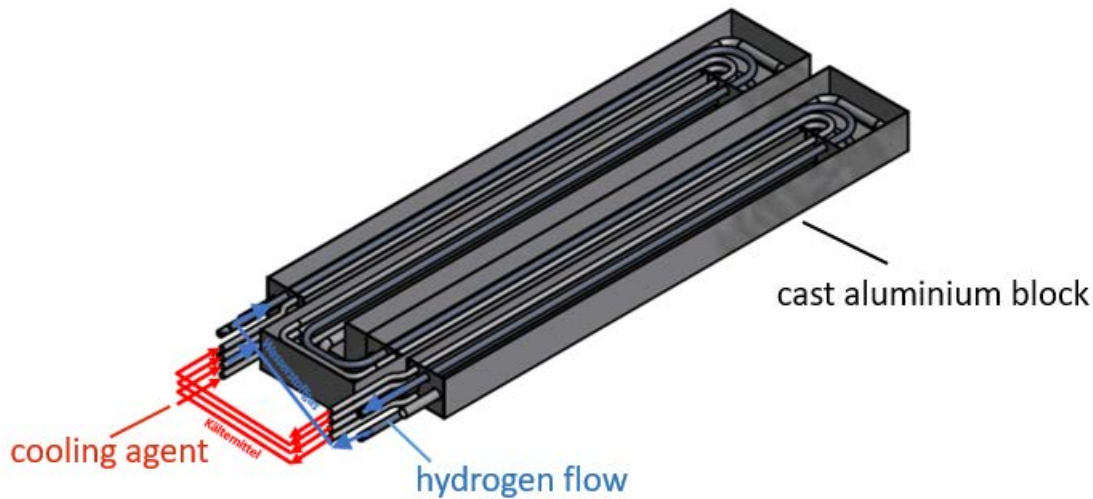


Figure 31: Sketch of an "ACF" unit [50]

After reaching the predetermined vehicle tank input temperature of - 40 °C, according to the underlying SAE fueling protocol (e.g. H70-T40), the hydrogen flow arrives at the pipe section "dispenser", as shown in figure 33.

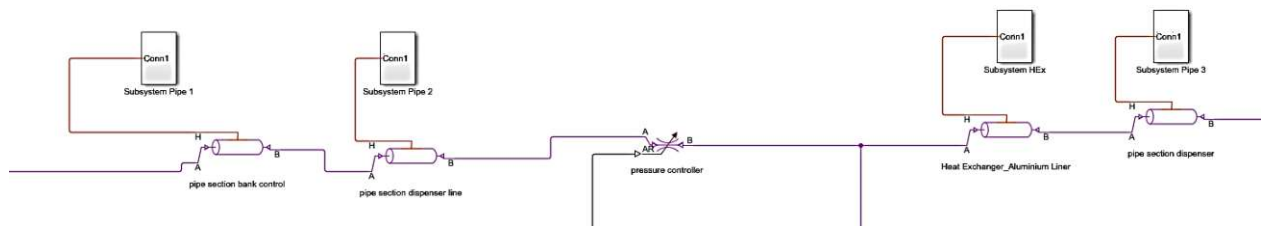


Figure 32: Pipe section "bank control", pipe section "dispenser line", pressure controller, heat exchanger and pipe section "dispenser" in the model's correct downstream flow direction

Before the hydrogen flow enters the vehicle tank, it passes three independently working sensor blocks. The "Mass & Energy flow rate sensor" block measures the hydrogen flow's mass flow rate in $\frac{g}{s}$, and provides an abortion of the fueling process in case of transcending the maximum allowed mass flow rate, according to SAE J2601. It is connected to a subsystem, which is acting as the mass flow control criterion, and is assembled by various Simulink logic block components. The "Pressure & temperature sensor", as well as the "Thermodynamic properties sensor" act the same according to their appropriate abortion criteria of SAE J2601.

The three subsystems, being connected to the vehicle tank block, offer the possibility to measure the density, mass flow rate and temperature inside the vehicle tank. In a real-world scenario, this can only be achieved if the vehicle is equipped with inline measurement sensors. As the majority of today's fueling procedures succeed on the basis of "non communication" protocols, the simulation uses these three inline measurement sensor blocks as optional tools for data comparison and validation.

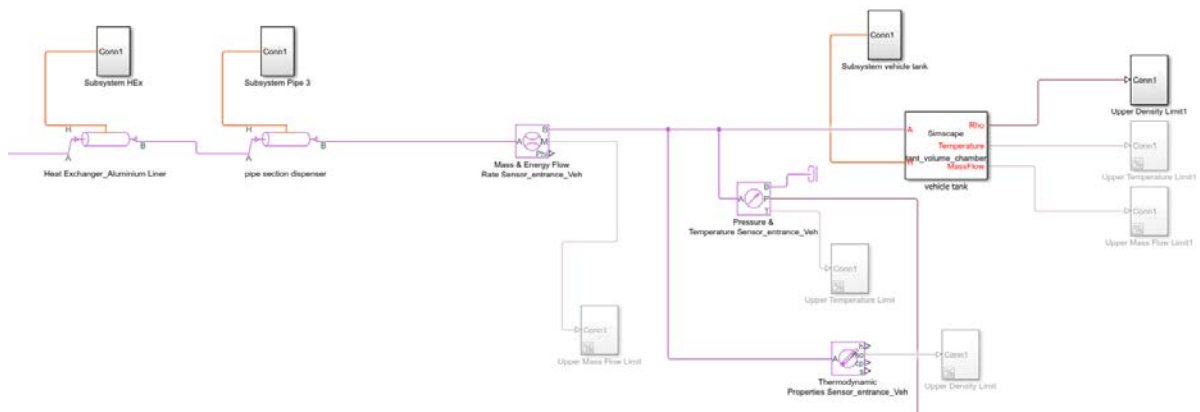


Figure 33: The "Mass & Energy flow rate sensor", "Pressure & temperature sensor" and "Thermodynamic properties sensor", concluding the gas flow unit together with the vehicle tank.

4.3.2 Heat transfer unit

The heat transfer unit displays the heat transfer between the hydrogen flow, the component's different material layers and fueling plant's environment. Heat becomes transferred either from the components through the material layers into the ambient air, or in the opposite direction, depending on the specific scenario's constitution and conditions. Each block component of the gas flow unit, except the sensor blocks, is connected to their heat transfer subsystem, modelling the heat transfer across each particular component's layer.

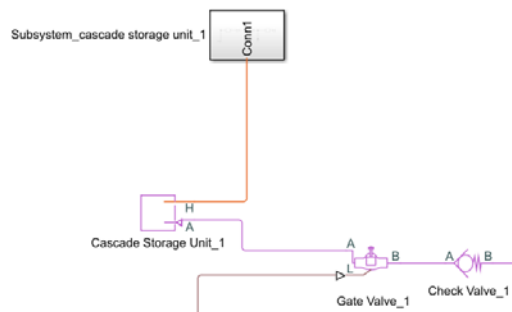


Figure 34: Thermal port connects cascade storage tank 1 with the tank's heat transfer subsystem

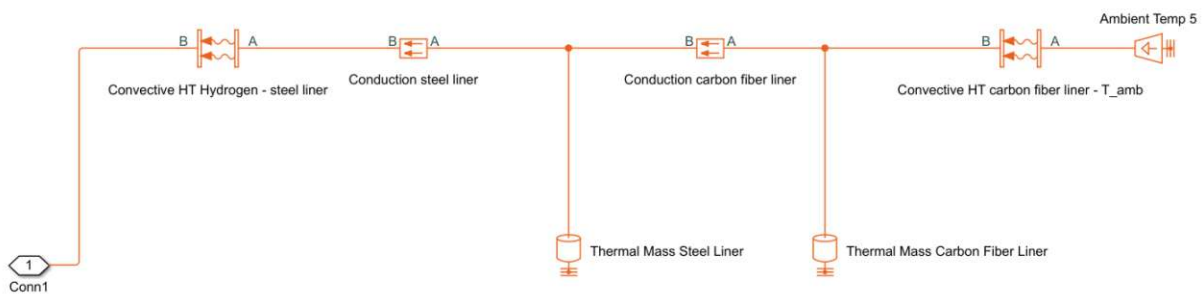


Figure 35: Physical component model of the heat transfer between hydrogen of cascade storage tank 1, the tank's material layers and the ambient air

Figure 35 shows the modeled heat transfer between a cascade storage tank and the ambient air in layers. The layer-to-layer heat transfer is structured into the following stages, providing a sufficient level of both simplification and accuracy:

- The underlying transport mechanism between the compressed gaseous hydrogen volume and the tank's innermost layer is based on convective heat transfer, being thermodynamically modelled and numerically approximated by the "Convective Heat Transfer Hydrogen – steel liner" block.
- The heat transfer throughout the innermost liner (chromium-molybdenum steel, in case of Type IV tank) can be predicted by the "Conduction steel liner" block, modeling conductive heat transfer within the steel liner in any direction.
- The heat transfer throughout the middle carbon fiber line can be predicted by the "Conduction carbon fiber liner" block, modeling conductive heat transfer within the carbon fiber liner in any direction.

Non-steady heat transfer problems can be solved by applying numerical methods. The corresponding approach consists of formulating the energy balance, and differentiate the energy balance with respect to time and space. *Through discretization of the control volume into smaller control volumes, the spatial derivative term can be eliminated.* Therefore, the remaining temporal derivative term can be solved through a suitable integration method, [25]. MatLab-Simulink offers a variety of solver programs. The choice of the solver used will be explained in subchapter 4.5.2.

- The blocks "Thermal mass steel liner" and "Thermal mass carbon fiber liner" initialize the steel and carbon fiber liner with their expectable masses, so that the appropriate layers can be discretized into smaller radial one-dimensional control areas.
- The heat transfer mechanism between the carbon fiber liner and the ambient air is based on convective heat transfer, and can therefore be modeled and numerically approximated by the "Convective Heat Transfer carbon fiber liner – T_amb" block.
- The block "temperature source" represents an ideal energy source within a Simscape thermal domain. It is able to maintain a constant temperature at its port. In the context of the scope of work, it models a constant ambient temperature, providing the thermal subsystem with a reference temperature. It is neither able to emit a heat flow, nor is it able to receive one, although it takes the role of the "end component" within this thermal subsystem.

4.4 Control unit

The control unit offers a modeling the fuel station's control circuit. Labeling the system in terms of control theory, the entire fuel station model can be classified as dynamic deterministic time-continuous distributed-parameter system. [51]

According to DIN 19226-4, the system can be structured into the following basic elements:

controlled variable	Pressure difference Δp of the volumetric flow rate, measured in $\frac{\text{bar}}{\text{s}}$ before and after the closest point of the restriction valve (= pressure controller)
Reference variable \equiv set value	APRR, selected by the control unit's algorithms and logic structures out of SAE J2601 look-up tables
Control variable	Pressure difference Δp in $\frac{\text{bar}}{\text{s}}$, which shall be adapted to the APRR
Actuator	Pressure controller = valve with a controllable restriction area and a corresponding input signal port
Disturbance variable	Volumetric flow rate at the entrance of the pressure controller

Table 3: Labelling the basic elements of the control unit according to DIN 19226-4 [51]

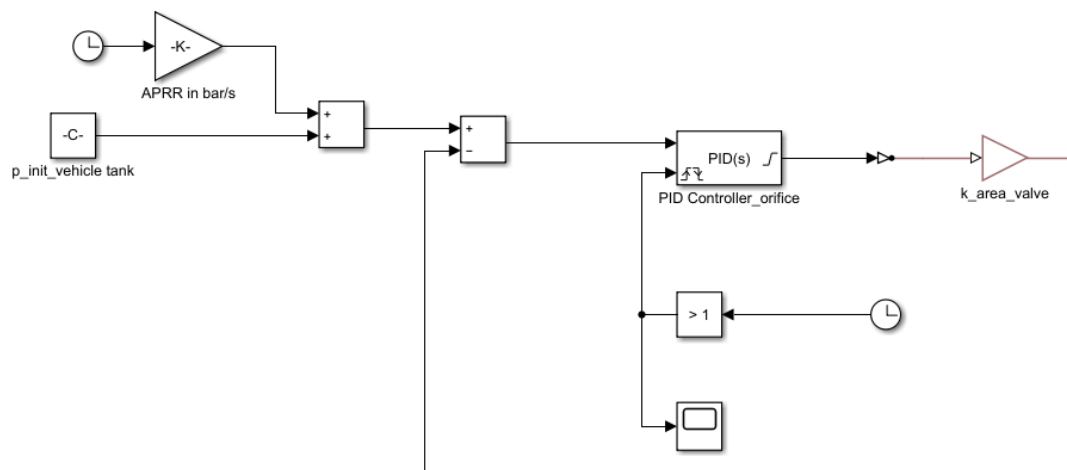


Figure 36: Central block elements of the control unit

Figure 36 shows the control unit's central elements. The look-up algorithm for finding a suitable APRR is modeled through the connection of

- a Simulink gain block,
- a continuous sum between the initial pressure value signal and the gain block, and
- a difference between the sensor's measured pressure value (measured at the exit of the pressure controller), and the sum's output signal.

This APRR Simulink signal then serves as the input signal of the PID controller block. After investigating the possibly best set of P-,I- and D-parameter values through established methods of e.g. Ziegler-Nichols and purely manual adjustment, the plant’s real-world PID-value settings could be even outperformed by Simulink’s “PID Tuner App” generated value set. In consideration of the control circuit’s aspired stability, rapidity and attenuation behavior, the commercial plant’s parameter set could not match the Simulink-generated levels of controller performance. It must be said that the commercially available plant’s control design is structured fundamentally different – being built upon a more complex constructional design and itself being written in the PLC language. Figure 37 shows a snapshot of the PID controller block’s input window.

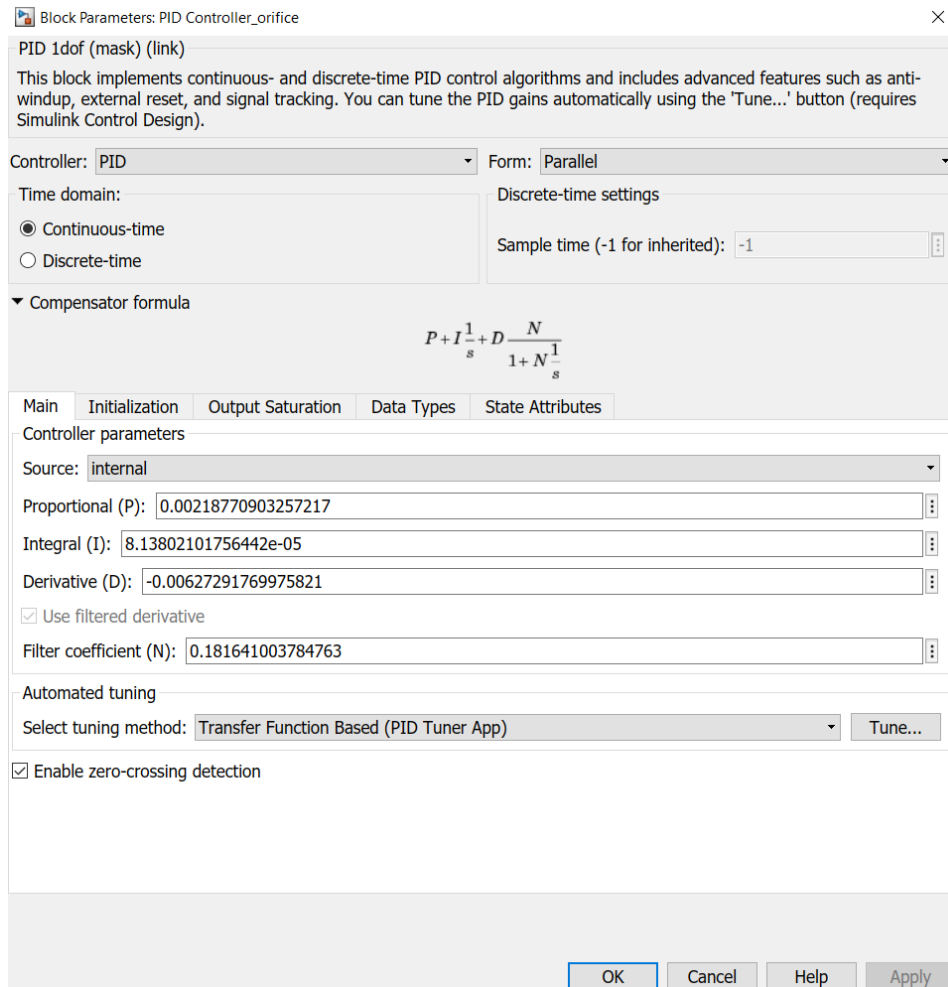


Figure 37: Snapshot of the PID controller block’s input window

It becomes obvious here that the character of the adjusted PID controller is a rather a PD-controller than a PID-controller, because the dominating magnitudes are the P-and D-parameters. This means that this PID-controller set up is able to avoid overshooting and permanent oscillating almost completely, while also being able to keep high its reaction rate, despite of a PD-controller’s inability to completely eliminate steady-state errors.

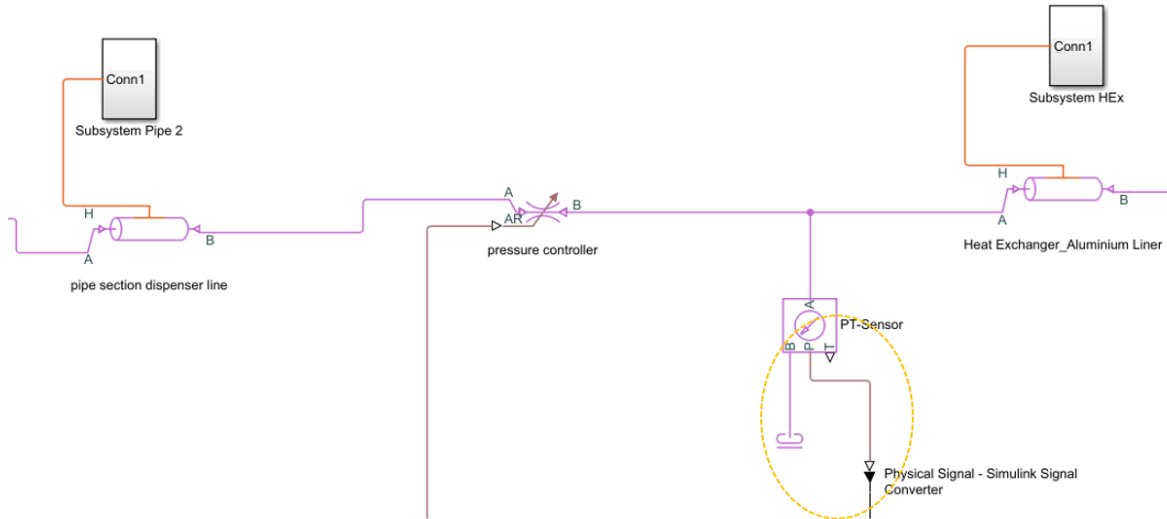


Figure 38: Pressure controller and the conversion of the measured pressure-gradient into a Simulink feedback signal

Figure 38 shows the pressure controller, taking the part as the actuator of this closed loop system. The reference signal of the PID-controller's preceding summation block, as shown in figure 37, is generated by the PT-sensor in figure 38. Before entering the summation block, the signal has to be converted from a pressure difference measurement into a mathematical Simulink signal, as being indicated by the yellow encirclement. The control circuit becomes closed thereby, and adjusts the volumetric flow rate's pressure gradient to an APRR value, generated by the control unit's gain block.

4.4 Tank switching mechanism unit

The mechanism of cascade tank switching underlies a second control circuit, independently operating alongside the control unit's circuit. Figure 39 shows the unit's part in which a lower and an upper *pressure tolerance ramp rate* are generated. This happens within the subsystems (yellow encircled) along the same procedure as described in subchapter 3.1.4 for the APRR signal.

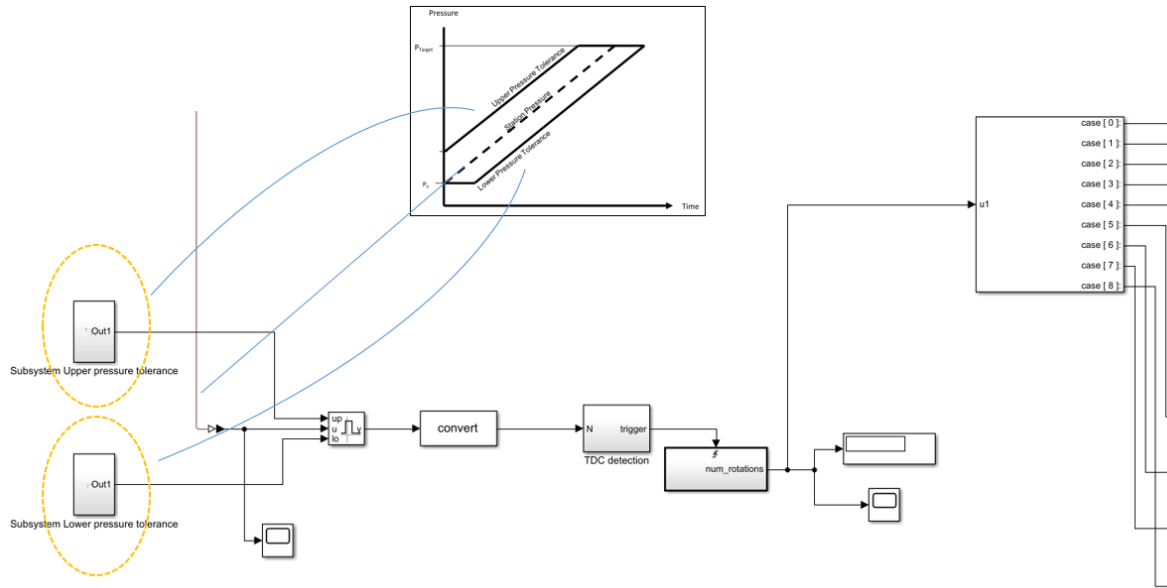


Figure 39: Upper and lower pressure tolerance boundaries generated inside the yellow encircled subsystems of this unit's snapshot

According to figure 20 in 3.1.2, these two signals together build the boundaries of the pressure tolerance corridor, in which the volumetric flow rate of the hydrogen flow is allowed to deviate in terms of pressure differences during a fueling procedure.

Figure 40 shows a detail-view of the middle part of the tank switching mechanism unit.

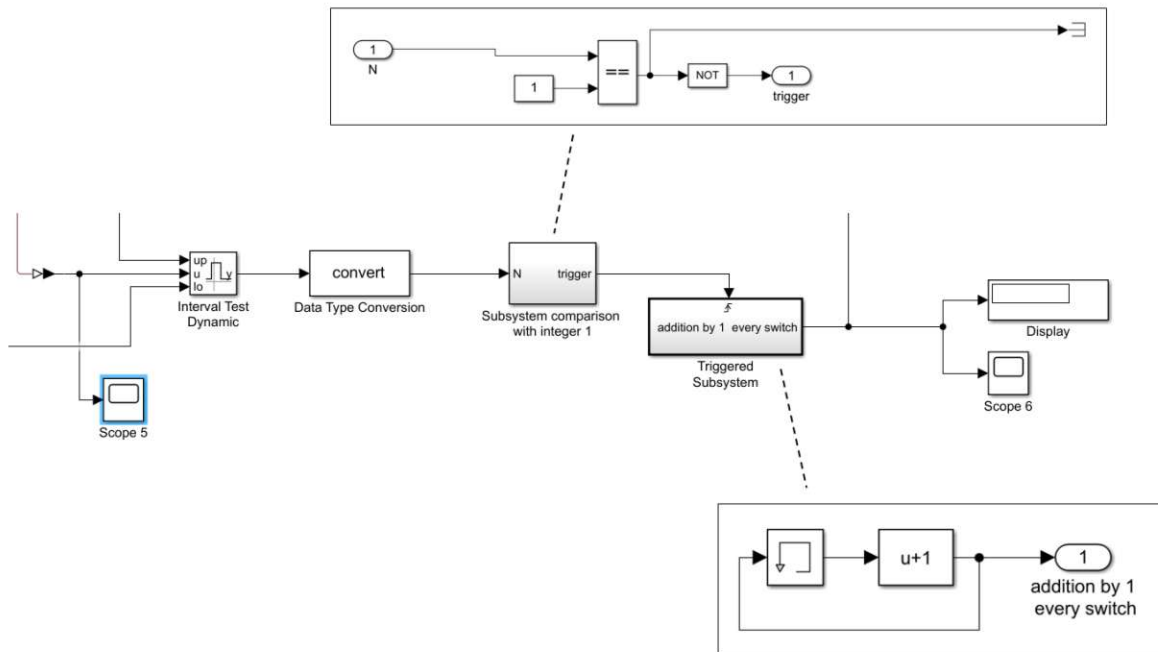


Figure 40: Middle part of unit „tank switching mechanism“ and its logic block subsystems in an expanded pop-up view

- The “interval test dynamic” block furthermore monitors if the fueling procedure’s pressure ramp crosses one of the two boundaries. In case of crossing, the “interval test dynamic” sends the Boolean output signal “TRUE”, otherwise it sends “FALSE”.

As long as the signal equals “TRUE”, the pressure ramp rate is progressing as expected.

A crossing of the lower boundary means that the current cascade storage tank has reached its lower pressure threshold, and a cascade tank switch must be initiated for continuing the ongoing fueling procedure.

- The following “data type conversion” block converts the Boolean signal into an integer, whereby “TRUE” equals 1 and “FALSE” equals 0.
- Next, the subsystem “comparison with 1” passes a signal, labelled as an integer with value 1, on to the next block. In case of the signal labelled 0, the signal becomes terminated by the “termination” block element, and the signal flow stops here.
- The “Triggered subsystem” block adds the integer of 1 up to its previously received input signal, and directly passes it on after adding up. In case of a cascade storage tank reaching its lower pressure threshold, the “triggered subsystem” block sends out an integer, taking up the role as a *counter* for each tank switching event.
- The following “display” and “scope” elements serve as simple tools for monitoring the appropriate functioning of the counter.

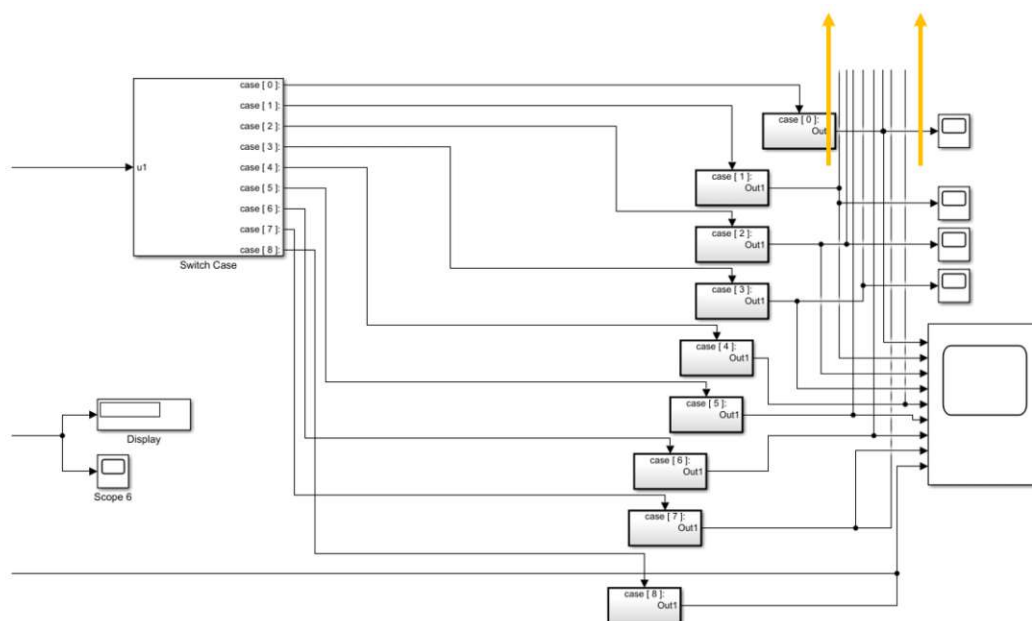


Figure 41: The “switch case” block, transmitting integers in case of a match between input signal and its inherent “case” values

- The “switch case” block, as shown in figure 41, transmits the integer 1 only if one of its inherent “cases” or conditions is met. For example, the “Case 1” output port sends the integer signal 1 *only* if its input is 1. “Case 2” output port sends the integer value 1 only if its input is 1. The same principle applies for “Case” ports 3 to 9.
- Each of the following connected subsystems contains a Set-Reset flip-flop, as shown in figure 42. These Set-Reset flip-flops provide that an input value once assigned at port “S” with the integer value 1 remains at 1 until the end of a simulation run.

The thereby created “tilting stability” of each “case” output port signal keeps the connected gate valves open, once they receive an integer signal of 1. This makes the overall cascade tank switching mechanism succeed, as long as the following check valves function as follows:

By reaching one tank’s lower pressure threshold, the next cascade tank’s gas flow cannot enter its preceding tank’s volume involuntarily, although an upstream pressure-gradient towards the preceding tank would physically allow it. Yet the check valves allow a gas flow to pass downstream only,

- Providing a safety function for unintentional refueling of one upstream cascade tank, and
- Let the pressure-gradient flow, continue and conclude an ongoing fueling procedure

at the same time.

The abovementioned block functions sum up all the working steps of a tank switching mechanism, though they do not build a closed loop system, as in 4.4. Yet, a closed loop is neither necessary, nor would it increase simplicity or robustness of the tank switching mechanism.

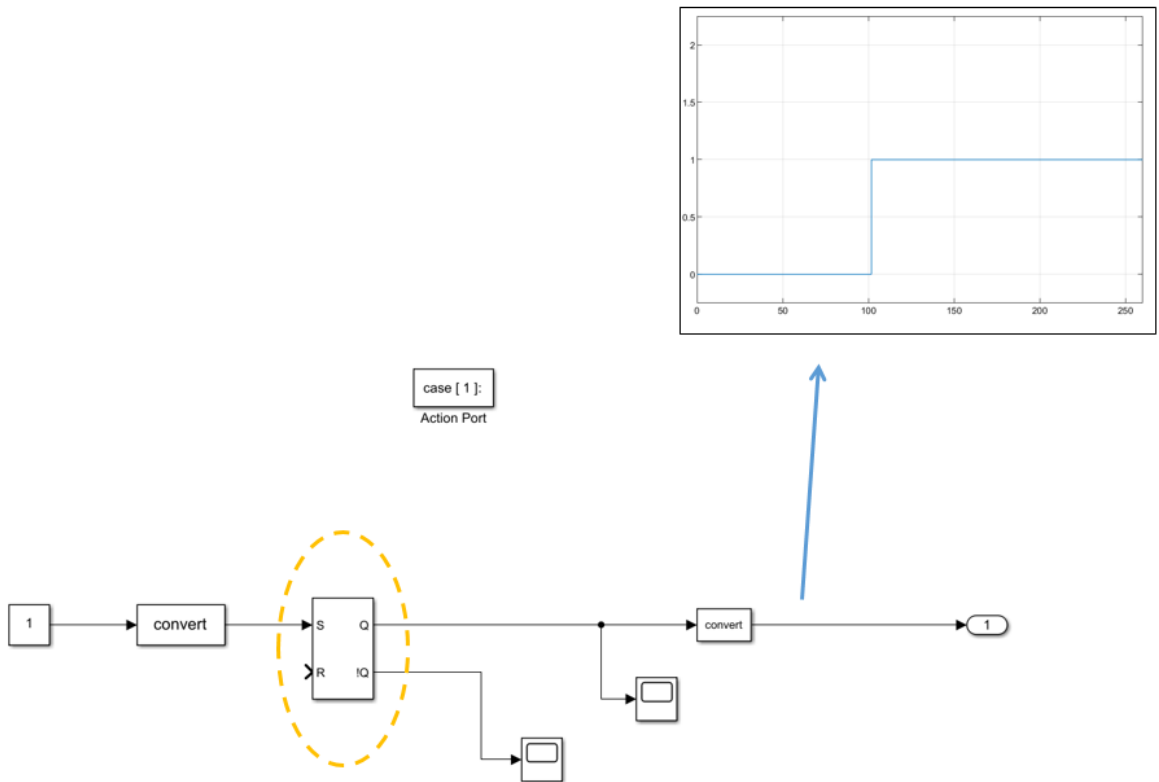


Figure 42: Close-up of a Set-Reset flip-flop and a corresponding assignment of an output integer value 1 with sustained "tilting stability"

4.5 Workflow of the simulation

Within this subchapter, the workflow of one representative Simscape simulation run shall be exemplified.

4.5.1 Model settings and configurations before simulation start

Before a simulation can be executed successfully, certain settings and configurations have to be adjusted within the simulation environment. Especially in case of a gas domain system, using Simulink-Simscape for a continuous dynamic simulation, the requirements are:

Domain-unspecific requirements:

- Expectable initial values must be assigned to all model's blocks
- The chosen solver method is applicable for the underlying simulation scenario. E.g., avoiding to choose a fixed-step solver for expectably continuous dynamic systems, requiring rather variable-step solver methods

Gas domain-specific requirements:

- The gas properties and solver configuration elements must be connected directly to the gas domain by gas domain connection lines.
- All pressure & temperature sensor blocks must be connected to an “absolute reference” element. This block represents the grounding reference element in a gas network where pressure and temperature are equal to zero.

Requirements for non-steady pressure-gradient based flow processes:

- A positive and steady pressure-gradient is available at the start and throughout the simulation, so that the mechanism – using the pressure-gradient as the driving force of the flow – can be utilized as intended

4.5.2 Choice of solver

Being able to simulate a dynamic system requires the computation of its states at successive *time steps* over a specified time span.

- The successive time points at which the states and outputs are computed are called **time steps**.
- The length of time between steps is called the **step size**.

The process of computing the states of a model in this manner is known as *solving* the model. The optimal solver balances high computational accuracy with the shortest simulation time. A universal solving method, being applicable to a certain amount of diverse models, cannot exist therefore, [52].

Based on the dynamics of a model, several conclusions on the choice of solver method can be made in advance:

- A variable-step solver is better suited for purely continuous models, e.g. the dynamics of a mass spring damper system.
- A fixed-step solver suits better for a model that contains several switches, like an inverter power system. This is due to the number of solver resets that would cause a variable-step solver to behave like a fixed-step solver.

Simulink offers a broad range of established and proven solver methods, amongst others the methods of Euler, LSODE, Dormand-Prince, Runge-Kutta, Dassl, Bogacki-Shampine and many more.

The **type of solver** selected is “variable-step”. *Variable-step solvers* vary the step size during the simulation. They reduce the step size to increase accuracy when a model's states are changing rapidly and increase the step size to avoid taking unnecessary steps when the model's states are changing slowly. This functioning might shorten the simulation time of your model significantly, compared to the fixed step solver, using a fixed step size throughout the whole simulation task.

The ***solver method*** selected is the “auto solver” option. It chooses a suitable solver algorithm and sets the maximum step size of the simulation. According to Simulink’s “auto solver selection” progress chart, as shown in figure 43, it is very likely that the predominant solver method is *ode23t*.

Auto Solver Heuristics

The system has		Continuous states		
		The system is an ordinary differential equation (ODE)		The system has differential algebraic equations (DAE)
The solver type is	Only discrete states			
	Fixed-Step	FixedStepDiscrete	ode3	ode14x
Variable-Step	VariableStepDiscrete	The model is stiff	The model is non-stiff	ode23t
		ode15s	ode45	

Figure 43: Solver selection process of the “auto solver” method

4.5.3 Executing the simulation

Basically, the execution of a dynamic system simulation can be divided into three simulation phases:

- **Model compilation phase:**
The simulation starts by invoking the model compiler program. The compiler converts the model to an executable form. In case of this gas domain model, the compiler most importantly
 - flattens the model hierarchy by replacing virtual subsystems with the blocks that they contain
 - determines the block execution order by task-based sorting.
- **Link phase:**
The simulation engine
 - allocates memory needed for signals, states, and run-time parameters
 - initializes memory for data structures that store run-time information for each block
 - creates method execution list - invoking a model's block methods to compute its outputs in the most efficient order
- **Simulation loop phase:**
The simulation engine successively computes the states and outputs of the system successively at intervals from simulation start time to the finish time, *using information provided by the model.*

During the simulation phase, the simulation’s author can take influence on the course of simulation for the first time. The model compilation phase and link phase are lists of tasks, entirely handled by the simulation engine.

Aiming for a basic level of usability, the simulation starts **programmatically**. This means that the three abovementioned phases only start if the MatLab command “sim” has been executed inside a superordinate MatLab-program.

This simulation’s superordinate MatLab program is simply an input window, asking the user to input fill in initial simulation values. Figure 44 shows a snapshot of the MatLab input window.

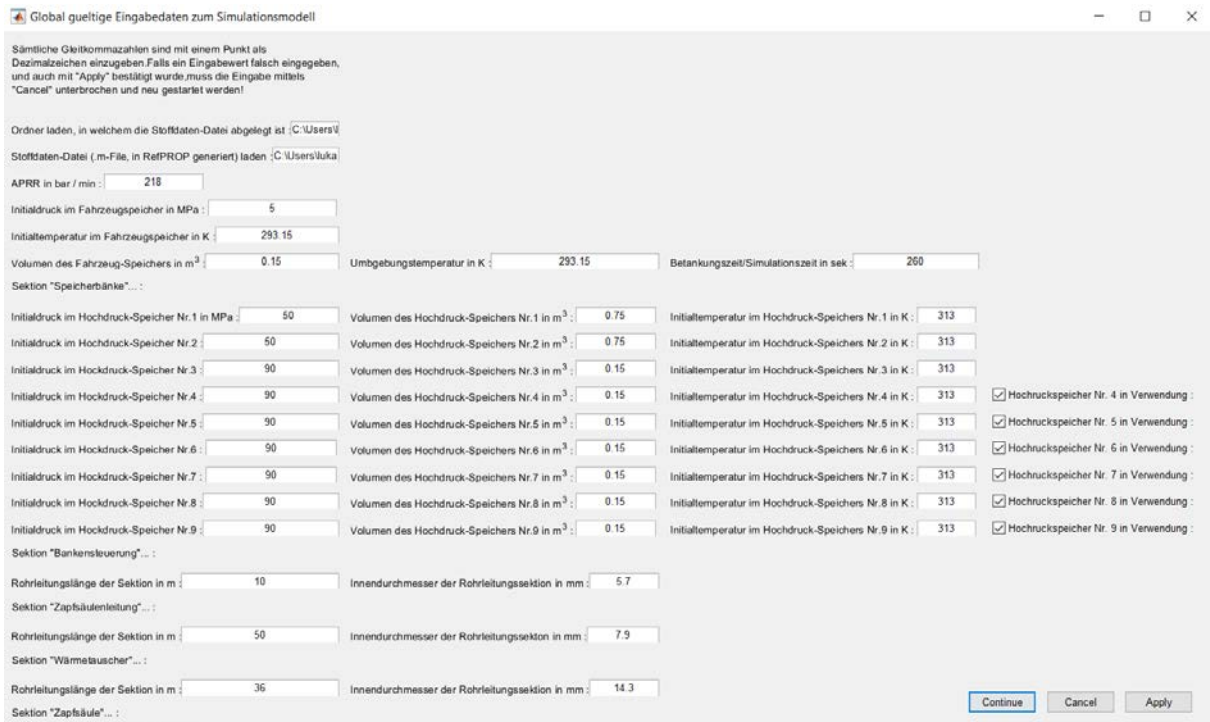


Figure 44: Snapshot of the MatLab input window, providing initial values for the following Simscape simulation

After filling in all the intended initial values and confirming the input (by pressing the window’s “continue” button), MatLab

1. calculates specific initial values, only calculable by MatLab, after certain essential parameters have been entered and confirmed.

E.g., calculating the pipe cross section area of the section “dispenser line” for the determination of the volumetric flow rate, as described by equation 3.29 in subchapter 2.3. The inner diameter, essential for this simple calculation, has therefore first to be entered into the input window. MatLab can then calculate the pipe’s cross section area as shown in equation 4.1.

$$A_{dispenser\ line} = \frac{d_{inner\ dispenser\ line}^2 \pi}{4} \quad (4.1)$$

2. opens the corresponding simulation file through the code's command "*open (file name)*"
3. enters the Simulation Loop phase through the code's command "*sim (file name, simulation time)*", which means:
Simscape starts to compute the states and outputs of the model at intervals from the simulation start time to the finish time, using all the input delivered by the superordinate MatLab code.

After a complete simulation run, the resulting thermodynamic parameters, such as the pressure or density inside the vehicle tank, can

- either be retrieved manually inside MatLab for postprocessing purposes. The parameters are by default stored within predefined "workspace variables" (e.g. the "simlog" variable) in structures of MatLab arrays (see figure 45 and 46), or
- become displayed by the Simscape Results Explorer. Thereby, all resulting parameters can be plotted and compared against each other. All of the simulation results of chapter 5 were generated graphically by the Simscape Results Explorer.

```

1
2
3   res = sim('Druckregler_v11_PKW.slx')           %assigning a file for starting the Simscape simulation
4                                           %to the workspace variable
5                                           %"res"
6
7
8   res.simlog.pipe_section_dispenser_line.mdot_A.plot   %retrieves the simlatoon data, stored within the variable "res",
9                                           %and creates a plot of the mass flow
10                                          %at the entrance of the plant'sdispenser line
11
12
13
14
    
```

Figure 45: An applicable MatLab code example for retrieving and printing an array of mass flow data inside MatLab

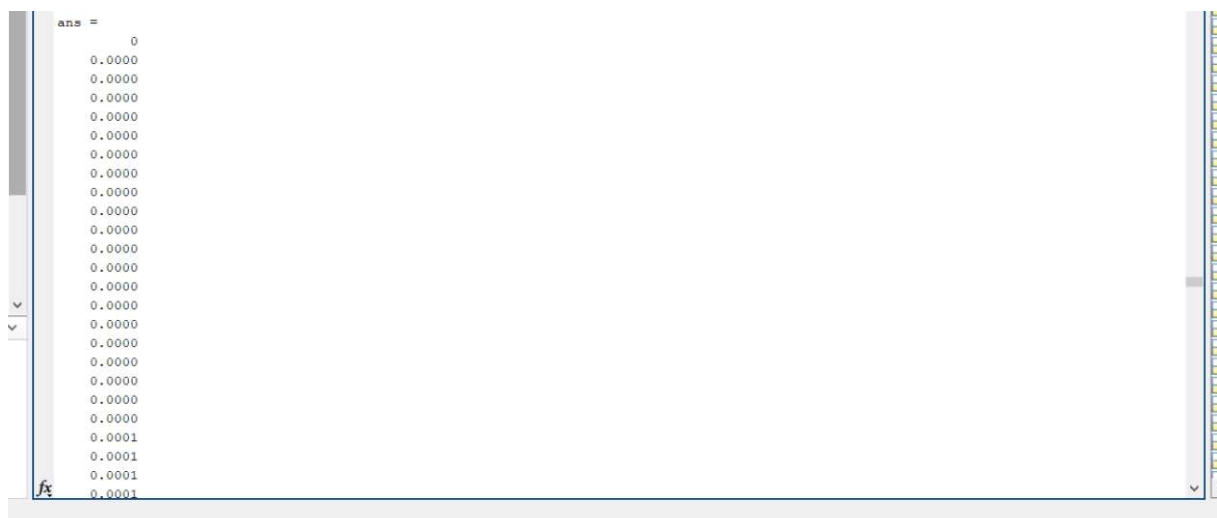


Figure 46: The corresponding cell array, containing the mass flow data

5. Simulation results

5.1 Parameter study

Within the following chapter, two realistic fueling scenarios will be introduced. Their simulated thermodynamic properties will be compared to each other.

Especially four working points along the model's horizontal structure offer key insights and information of certain simulated state variables. Beforehand, these four working points shall be introduced for all upcoming comparison and analysis efforts. The positions are situated

1. after the outlet of the cascade tanks = before the pressure controller inlet
2. after the pressure controller outlet
3. after the heat exchanger = inside the dispenser = before inlet of the vehicle tank
4. inside the vehicle tank

Figure 47 shows the positioning of the four working points inside the basic process scheme.

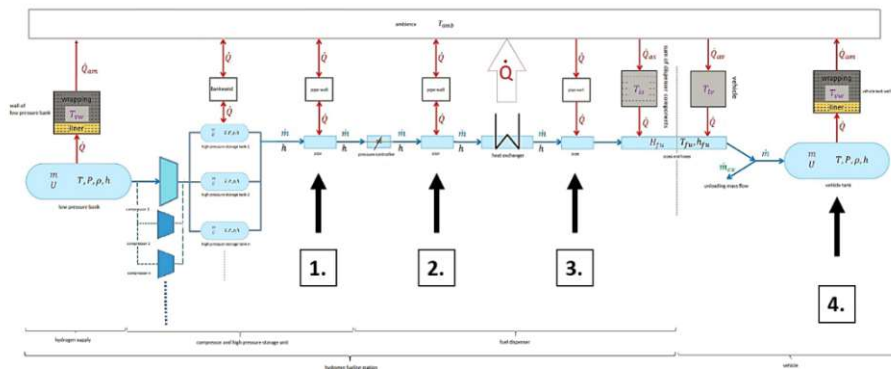


Figure 47: Positioning of the four working points inside the basic process scheme

5.1.1 Scenario 1

The first scenario investigated displays a very typical fueling scenario for a passenger car. The initial values of the fueling procedure are listed within table 3.

Cascade storage tanks

<u>Storage tank 1</u>		
p_{init} in MPa	T_{init} in K	V_{init} in L
50	313.15	750
<u>Storage tank 2</u>		
p_{init} in MPa	T_{init} in K	V_{init} in L
75	313.15	750
<u>Storage tank 3</u>		
p_{init} in MPa	T_{init} in K	V_{init} in L
90	313.15	150

Vehicle tank

p_{init} in MPa	T_{init} in K	V_{init} in L
5	293.15	150

$T_{ambient}$ in K	293.15
Fueling protocol category	H70-T40
APRR in MPa/min	21.8
$t_{simulation}$ in s	260

Table 4: Typical initial values of a passenger car fueling scenario

Providing an initial pressure level of 5MPa, the car's vehicle tank is almost entirely empty. By choosing any available fueling protocol category, several target values can be read out of SAE J2601 before the simulation has started. These target values serve as central references, allowing an evaluation of the course of simulation. The following target values shall be accomplished for fueling scenario 1:

- The target pressure of the vehicle tank, according to category H70-T40 non-communication, shall be 74.5 MPa
- Considering the APRR of 21.8 MPa/min for a H70-T40 fueling protocol, the target fueling time must be 3min11s or less
- The maximum pressure level for the 4-7kg tank volume category is 80Mpa

Figure 48 shows the simulated pressure profile for table 3.

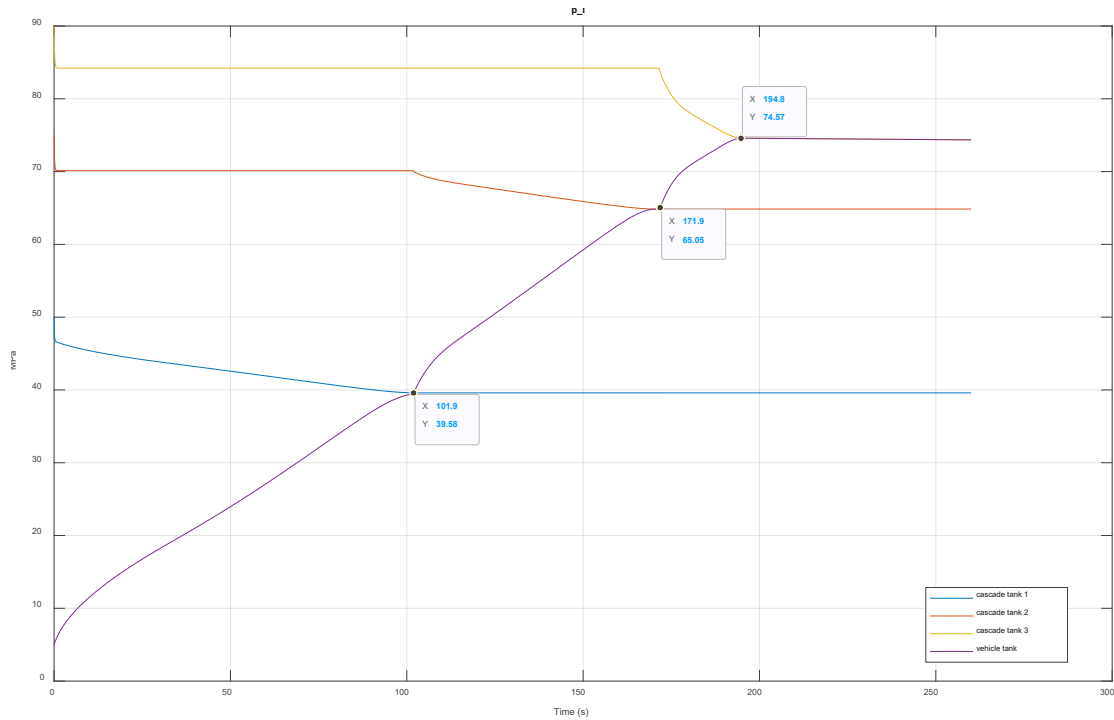


Figure 48: Pressure levels of an H70-T40 non-com fueling procedure, utilizing three cascade storage tanks

As can be seen, the pressure equalization between cascade storage tank 1 and the APRR initiates the corresponding gate valve of cascade storage tank 2 to open, starting the next cycle of pressure equalization. It becomes obvious that cascade storage tank 1 and 2 can provide hydrogen as long as the pressure gradient is non-zero. The highly reactive behavior of the PID controller provides for a tank switching very close to reaching total pressure equalization. This behavior arranges for the highest levels of pressure gradient utilization. A switching mechanism, starting too early, would only waste potential pressure levels of the cascade tanks in current use. Figure 49 shows the model's high exploitation of available pressure levels, allowing the pressure controller to fuel until 0.03s close to pressure equalization.

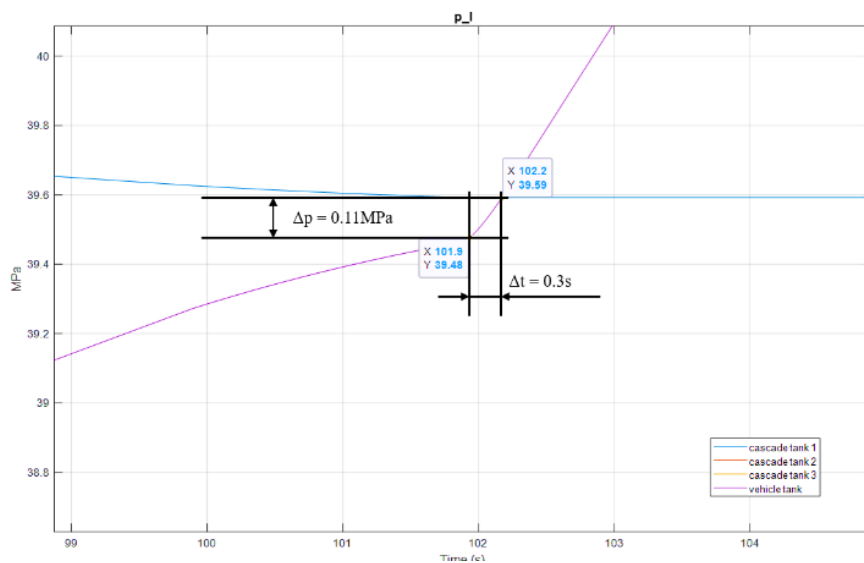


Figure 49: Display of the tank switching mechanism's late actuation, resulting in high exploitation rates of the pressure gradient

Looking at the final pressure level within figure 48, it becomes visible that the simulation did reach the foreseen target pressure of 74.5MPa almost on the spot, as determined within the look-up tables of SAE J2601 for a “non-com” H70-T40 protocol. However, possible causes for the non-reaching of the foreseen target pressure are manifold, and can be divided into two categories:

- Constructional design causes:
 - The pipe diameters selected for each pipe element are too small in diameter, providing higher pressure losses and therefore less potential pressure-gradient than expected of SAE J2601

- Simulation design causes:
 - The pressure controller did actuate either to slow during phases of onramping and tank switching, or
 - The pressure controller actuated along an APRR, shallower than proposed by SAE J2601

Figure 50 shows the temperature trends at the outlets of cascade tank 1-3, and the inner vehicle tank temperature.

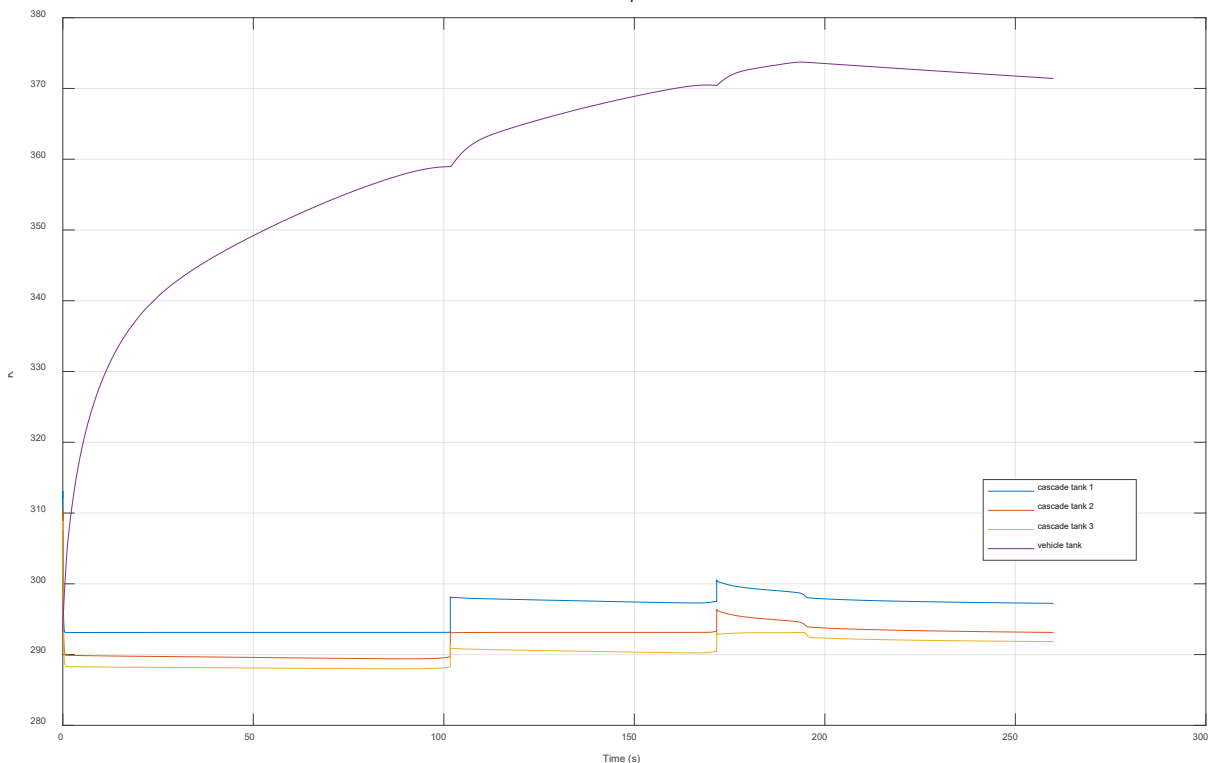


Figure 50: Temperature development, simulated at the cascade tank outlets, and the inside of the vehicle tank

It can be observed that the vehicle tank temperature overshoots the SAE J2601 temperature operating limit of 358.15K (85°C) of the “communication” method by 12K.

While an overshooting of this temperature operating limit triggers an abortion command within every commercial plant, a temperature operating limit does not exist for the “non-com” method.

Commercially applied vehicle tanks are designed to be able to withstand temperatures beyond 358.15K for limited amounts of time. This must be provided for the common fueling scenario, as described in the following:

A FCEV leaves the air-conditioned garage with a vehicle tank temperature of 298.15 K. After 1-2 minutes of driving, it arrives at a hydrogen fueling station. Its vehicle tank temperature still measures 295.15 K, although the ambient temperature is significantly lower – measuring 268.15 K. By applying the “non-com” method, the station’s algorithm chooses the APRR, based on the ambient temperature and the vehicle tank volume. For lower ambient temperatures, steeper APRRs must be used. The same applies for the contrary case. [43]

While the yet higher vehicle tank temperature did not assimilate to the ambient temperature, the fueling procedure starts, erroneously applying an APRR too steep for the vehicle tank’s non-assimilated temperature. Therefore, the operating temperature limit of 358.15 K becomes overreached close to the end of the fueling procedure.

Therefore, a temporary overreaching of the intended operating temperature limit of 358.15 K is *acceptable* for the “non-com” fueling scenario, as long as being overreached for seconds close to the end of the fueling procedure.

Figure 50 shows the progress of the mass flow rates for 3 cascade storage tanks and a H70-T40 protocol. The cascade tank’s mass flow rates, as well as the vehicle tank mass flow rate are plotted as in case of inline measurement.

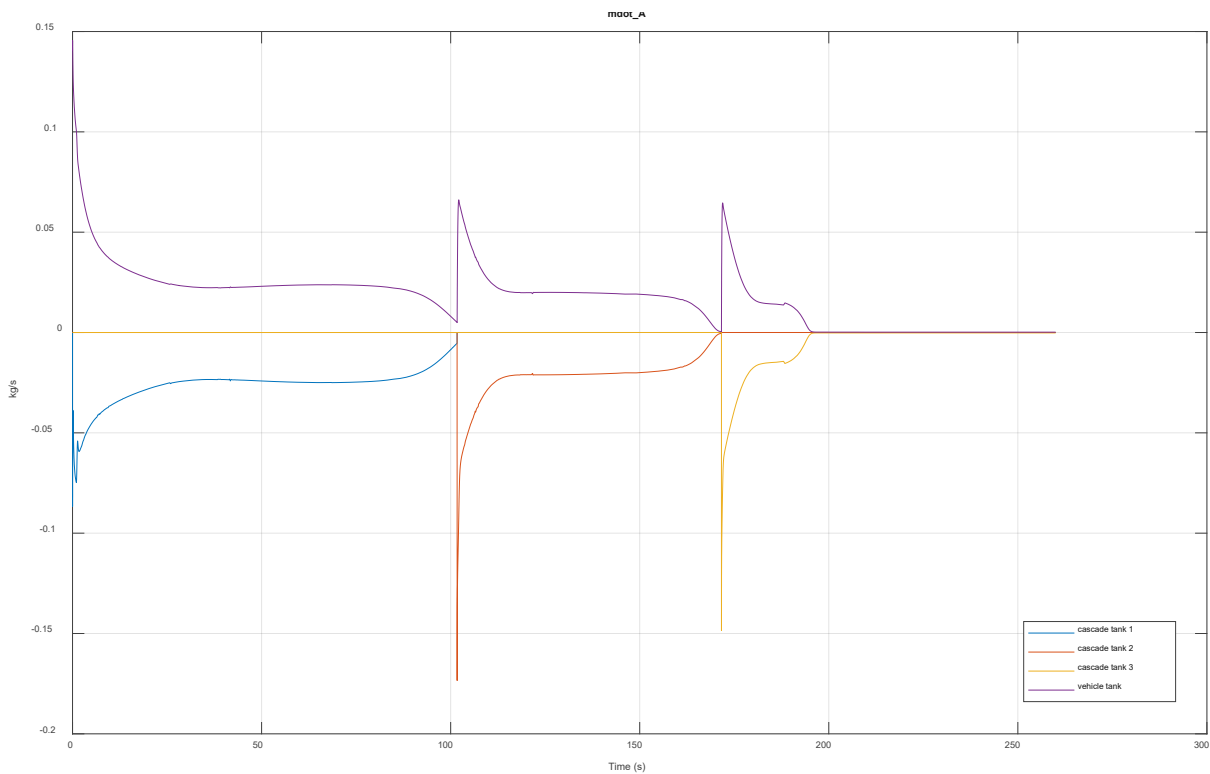


Figure 50: Progress of mass flow rate for an H70-T40 fueling and 5MPa initial vehicle tank pressure, using three cascade tanks

The tank switching is clearly visible in form of the sharp-edged peaks. As soon as the pressure controller starts to realign the hydrogen flow's measured pressure ramp to the APRR, the peaks gradually start to flatten out. At time 120 s, the mass flow overreaches the operating mass flow limit of 0.06 kg/s for a few seconds. This overreaching would not trigger an abortion command inside commercial plants, because it lasts not any longer than 5 seconds, which is the maximum period within a “non-com” fueling scenario for overreaching, [43]. Hence, the simulation does not violate the safety limits of the underlying fueling protocol.

Figure 51 shows the densities at the inside of the three cascade storage tanks and the vehicle tank.

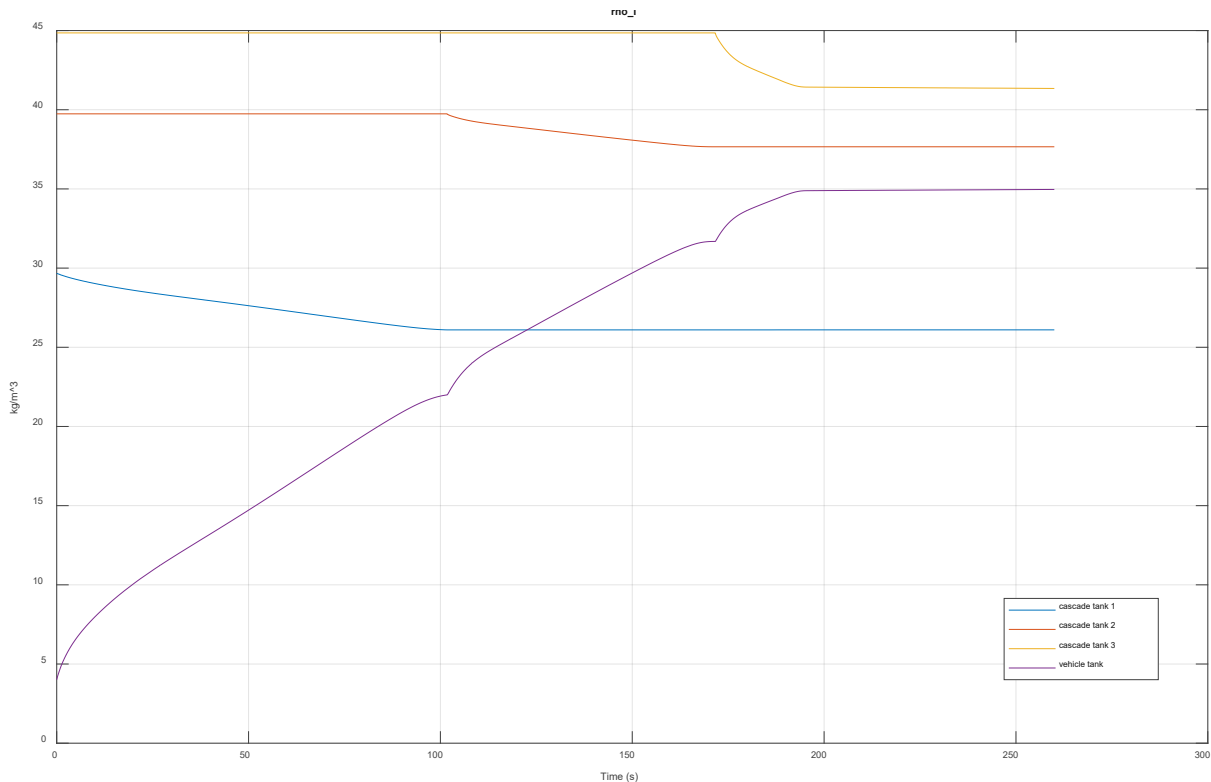


Figure 51: Density gradients, simulated inside of cascade tanks and the vehicle tank (initial pressure: 5 MPa)

Similar to figure 46, the tank switching mechanism becomes visible in form of a flattening out of the density gradient, reaching its end of capacity in form of a slight yet noticeable kink. Besides the rather typical progressing course of the density gradients, it is worth mentioning that the target density for any fueling protocol category, $40.2 \frac{g}{cm^3}$, has not been reached, [43].

This circumstance is not a major issue. Since fueling stations, operating with the “non-com” method, are not able to measure thermodynamic properties, such as e.g. the vehicle tank density, they rely upon fueling along a rather conservative APRR. The lack of measurement instruments, as opposed to the “com”-method, makes it indeed impossible to reach the target density of 40.2 g/L and the individual target pressure at once.

Next, the convective heat flow rate between hydrogen flow and the pipe's inner steel surface will be analyzed. As displayed in figure 53, the convective heat flow rates have been superposed for working points 1-4.

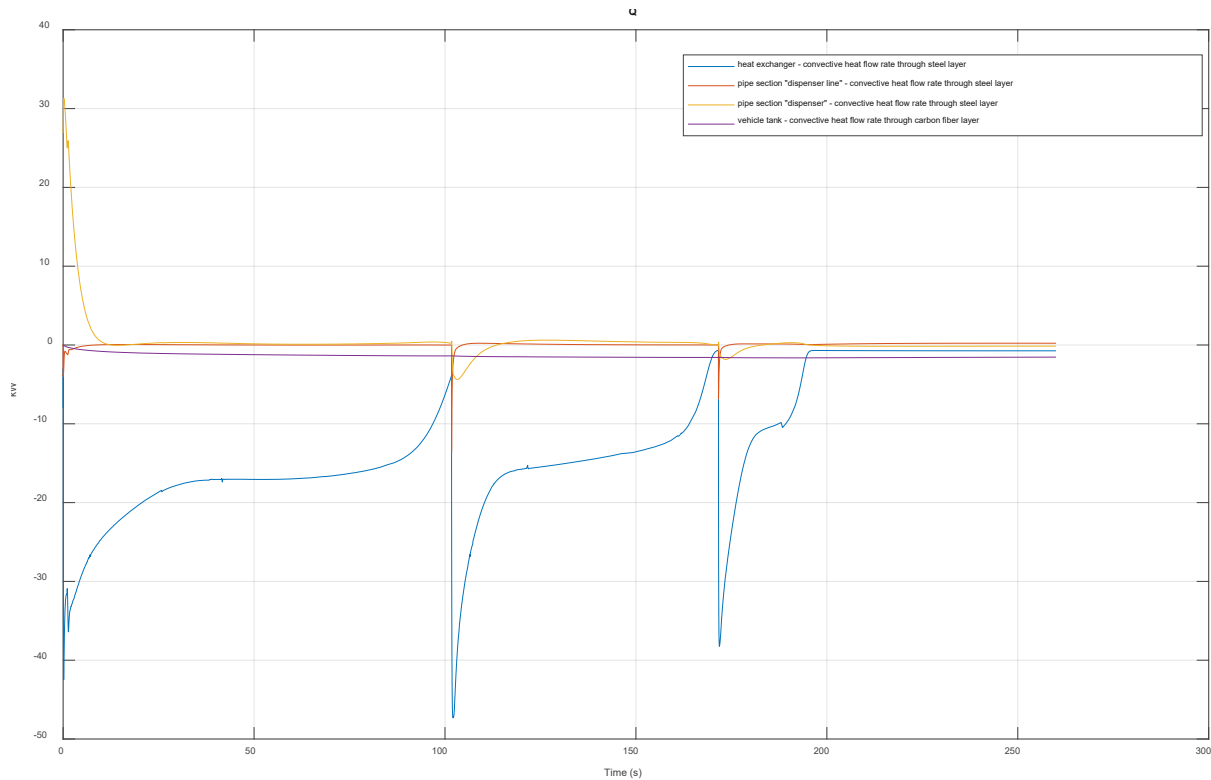


Figure 53: Convective heat flow rates between hydrogen flow and the components' innermost layers

As foreseen for a properly functioning fueling station, the heat exchanger delivers significant convective heat flow rates into the hydrogen flow. The heat exchanger's cooling power is visible as the blue, negative-signed heat flow rates of figure 53. The cooling power reaches a minimum at the pressure equalization between a cascade storage tank and the APRR. At this state, corresponding for pressure equalization, the heat exchanger recognizes the tank switching mechanism and immediately starts to equalize the throttling heat at the pressure controller outlet.

The convective heat flow rate at the thermal port of pipe section "dispenser" starts with a significant positive-signed high heat flow rate at the start of the hydrogen fueling procedure. This is definitely due to the expansion of hydrogen directly at the beginning of the fueling procedure, generating heat at the same time according to the Joule-Thomson-effect.

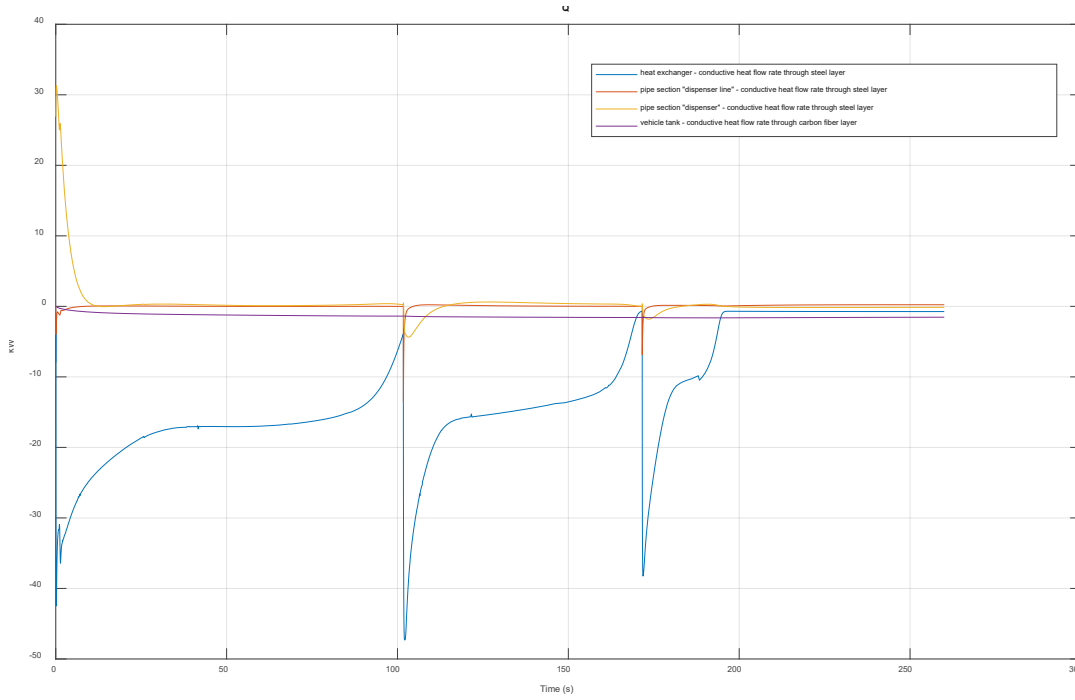


Figure 54: Conductive heat flow rate through the components' steel or carbon fiber layers

Similar to convective heat transfer rates of figure 53, the conductive heat flow through the component's innermost layers show

- the heat exchanger's supply of cooling energy as the numerically largest heat flow rate, besides
- a heat flow through the dispenser's steel layer towards ambient air within the first seconds, generated by throttling of the pressure controller.

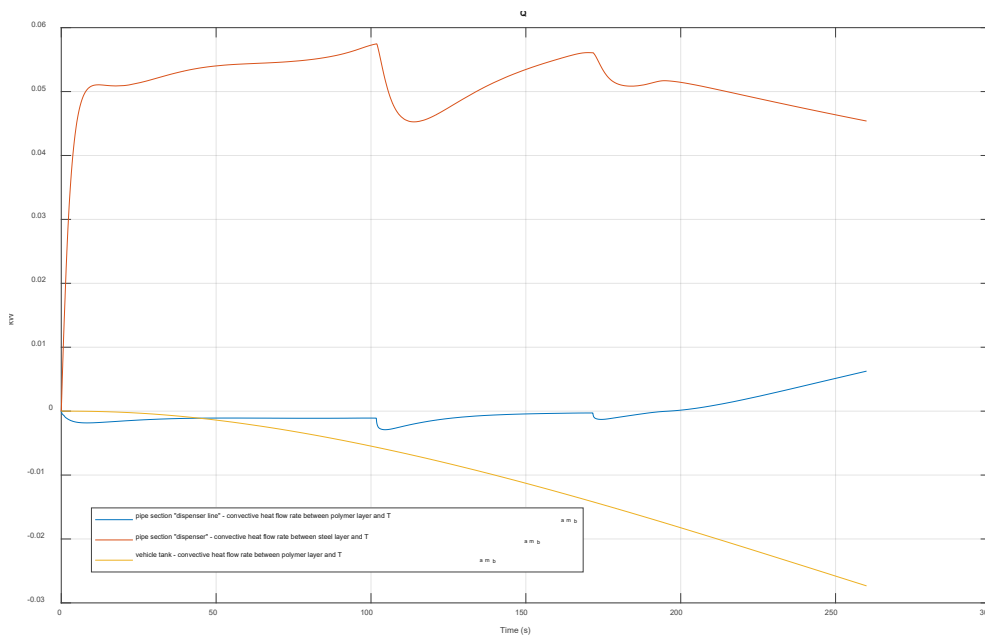


Figure 55: Convective heat flow rates between outermost components' material layers and the environment

Figure 55 shows the convective heat transfer between the outermost components' material layers and the ambient air. At first glance, it looks as if the convective heat flow from steel layer towards environment of the dispenser block shows overall high heat flow rates, contradicting the behavior of preceding conductive heat transfer of figure 54. Yet the magnitudes of the convective heat transfer rates are lower by a factor of 500, proving that

- the convective heat flow from the component's material layers towards ambient air are significantly low.
- The magnitude of conductive heat flow rates of figure 54 is consistent with the magnitude of the adjacent convective heat flow rates of figure 55.

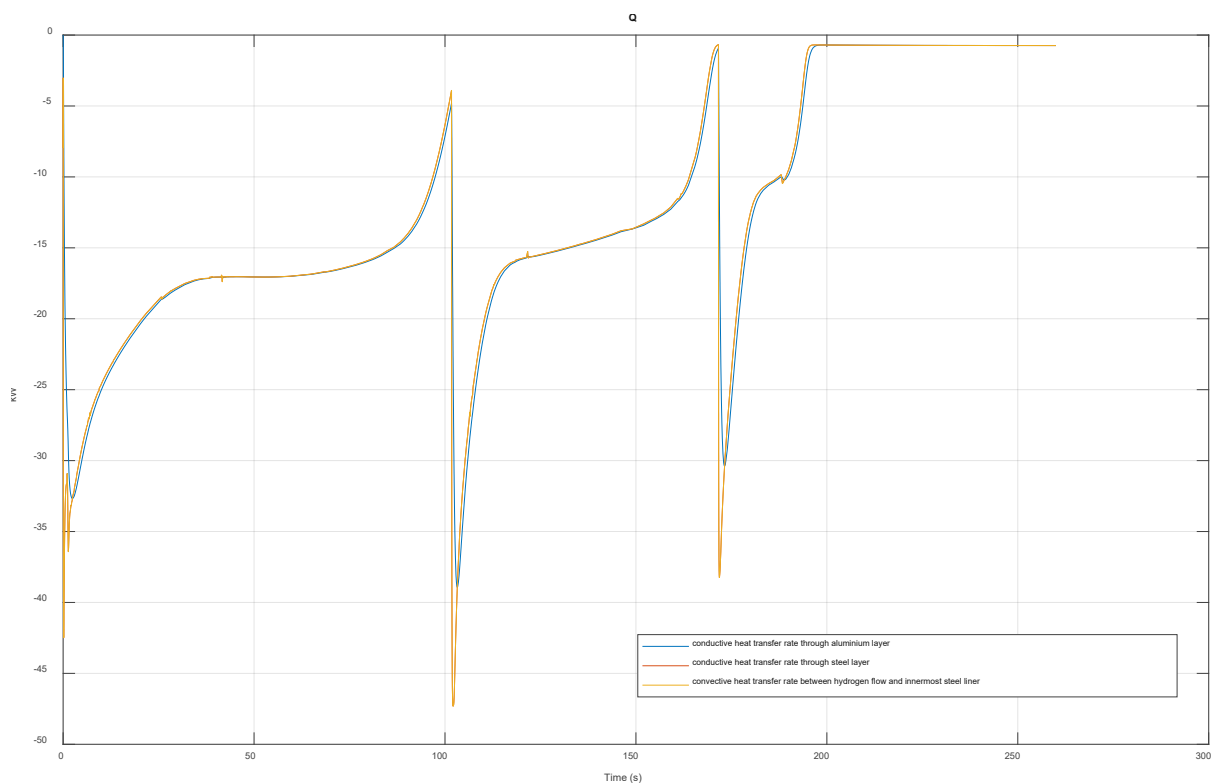


Figure 56: Conductive and convective heat flow rates through the material layers of the heat exchanger

Figure 56 shows the heat transfer through all material layers of the heat exchanger. Therein, both convective and conductive heat transfer rates show the same course of heat transfer rate, although the convective heat of the expanded, heated hydrogen numerically peaks at the tank switching.

This peaking can be expected for the convective heat flow inside the heat exchanger because of the following order of transfer phenomena:

1. The heat at first dissipates instantly from the hydrogen flow through the material layers into the environment. This effect shall be labelled as *instant cooling*.
2. Next, a turning point is reached, which signals the end of the instant cooling effect.
3. The heat exchanger's effort set in, starting to neutralize the remaining generated amount of expansion heat. This effect shall be labelled as *actuated cooling*.

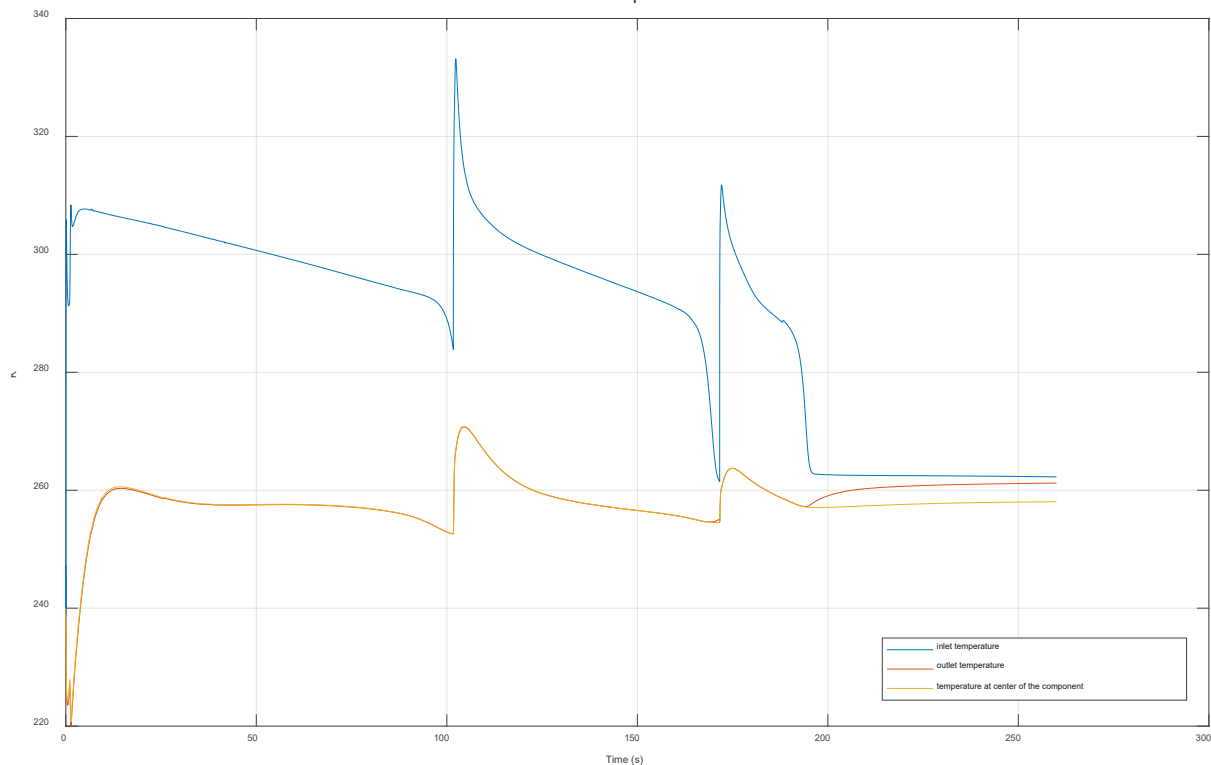


Figure 57: Temperatures at the inlet, outlet and center of heat exchanger block

The following graph shows inlet, center and outlet temperatures of the heat exchanger’s hydrogen flow. At the beginning of the fueling procedure and each tank switching event, the expansion heat of the hydrogen flow – subsequent to gate valve opening or throttling – gradually becomes equalized by the continuous cooling power supply of the heat exchanger.

The modelled heat exchanger component provides an outlet temperature of 255 K as its best performance of cooling at the tank switching between tank 1 and 2.

Compared to commercially available ACF units, this performance is neither outmatching commercial ACF’s performances, nor is it insufficient. According to available measurement data on the performance of the company’s applied ACF unit, it is possible to maintain outlet temperatures of 235-240 K almost steadily during a typical fueling procedure. This fact makes it obvious that the modelled heat exchanger block has not reached its full potential of predicting real-world ACF behavior. For reasons of applicability and a limited amount of research time frame, the model of the heat exchanger has been kept rather simple, in order to provide a fully functioning yet simple block component for the overall plant model.

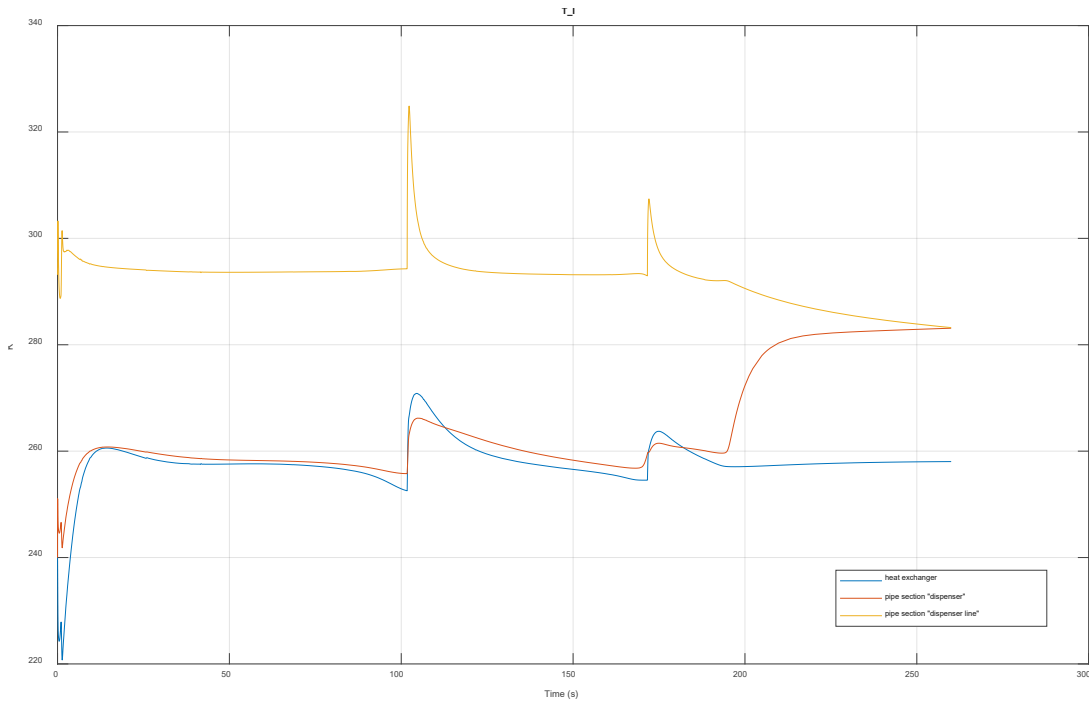


Figure 58: Temperatures inside of heat exchanger and pipe sections “dispenser line” and “dispenser”

Figure 58 shows the pipe sections “dispenser line” and “dispenser” as upstream and downstream components of the heat exchanger, and its corresponding temperature gradients. After the end of fueling at 195 s, the pipe section temperatures of the idling fueling station start to even out into an idling temperature of approximately 282 K. The heat exchanger block reaches an idling temperature of 259 K, yet it does not achieve its predetermined ideal cooling target temperature of 233 K, as being determined in the block component’s input mask (figure 59).

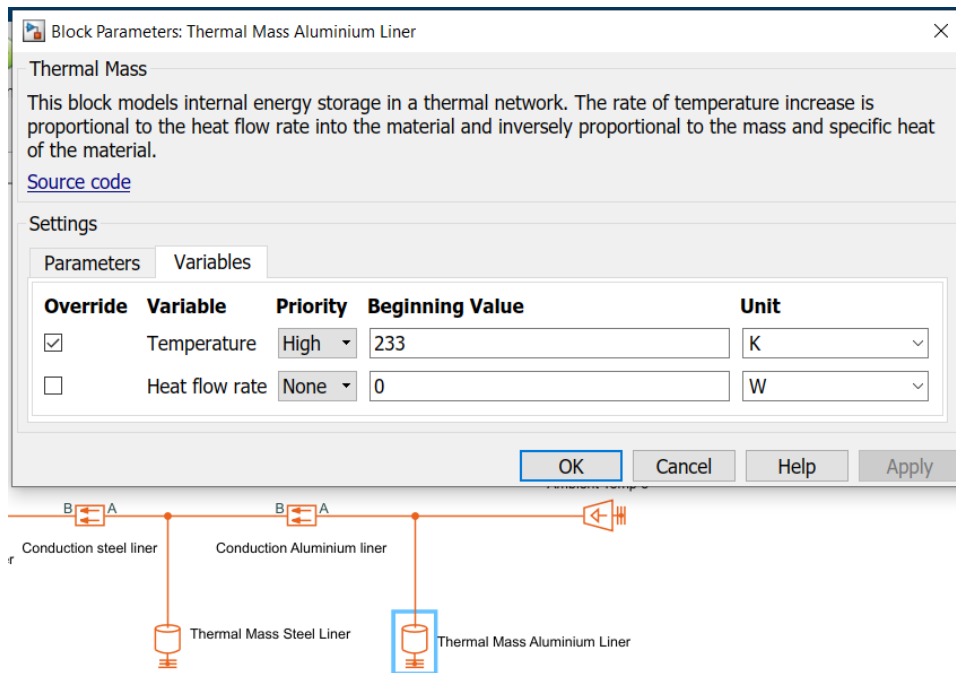


Figure 59: Snapshot of the Simscape input mask of the ACF's "thermal mass" block for the aluminum layer

This circumstance reveals that the cooling energy, supplied by the “target cooling temperature” block (figure 60), cannot be delivered unrestrictedly to the hydrogen flow, in either case of a running or an idling fuel station.

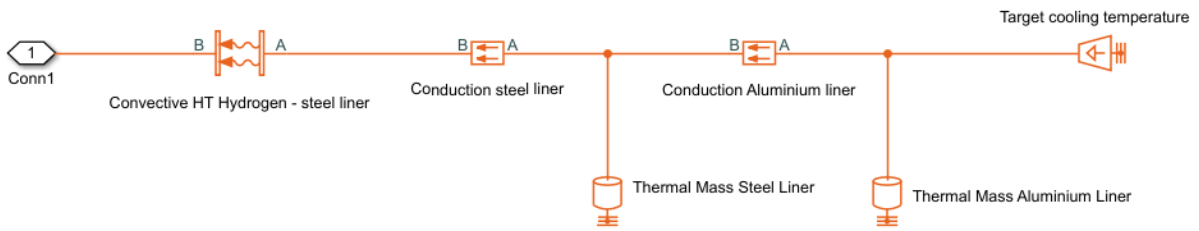


Figure 60: Model of the heat exchanger's "thermal domain" subsystem, showing the "target cooling temperature" block as the source of cooling supply

After checking the already applied thermal conductivity coefficients for the aluminum and steel layer, the numbers seem to be accurate and furthermore applicable. The thermal conductivity coefficients applied are:

Thermal conductivity coefficients in $\frac{W}{mK}$

Steel (34CrMo4)	Aluminum	Carbon fiber
45 [53]	700 [43]	0.5 [43]

Table 5: Thermal conductivity coefficients applied for the material layers of the model

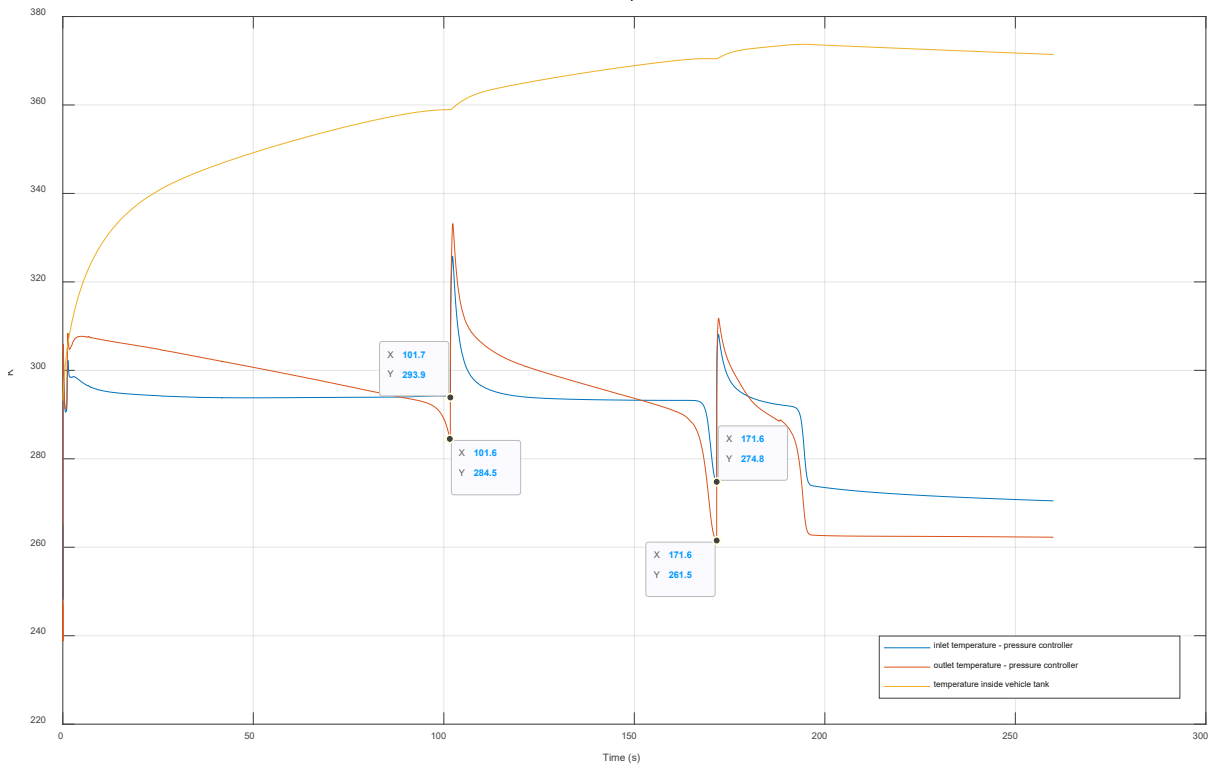


Figure 61: Temperatures at the inlet and outlet of pressure controller, together with inner vehicle tank temperature

Figure 61 shows the temperature gradients at the inlet and outlet of the pressure controller, together with the inner vehicle tank temperature. The following observation is worth mentioning:

While the inlet temperature measures lower for each cascade tank fueling cycle, the outlet temperature firstly is higher, due to expansion, and then cools down. This cooling is achieved through the decrease of the pressure gradient along a fueling cycle. A decrease of pressure gradient at the outlet of the pressure controller results in less expansion of the outflowing hydrogen flow, and therefore less increase in flow temperature. This behavior can be considered as expectable.

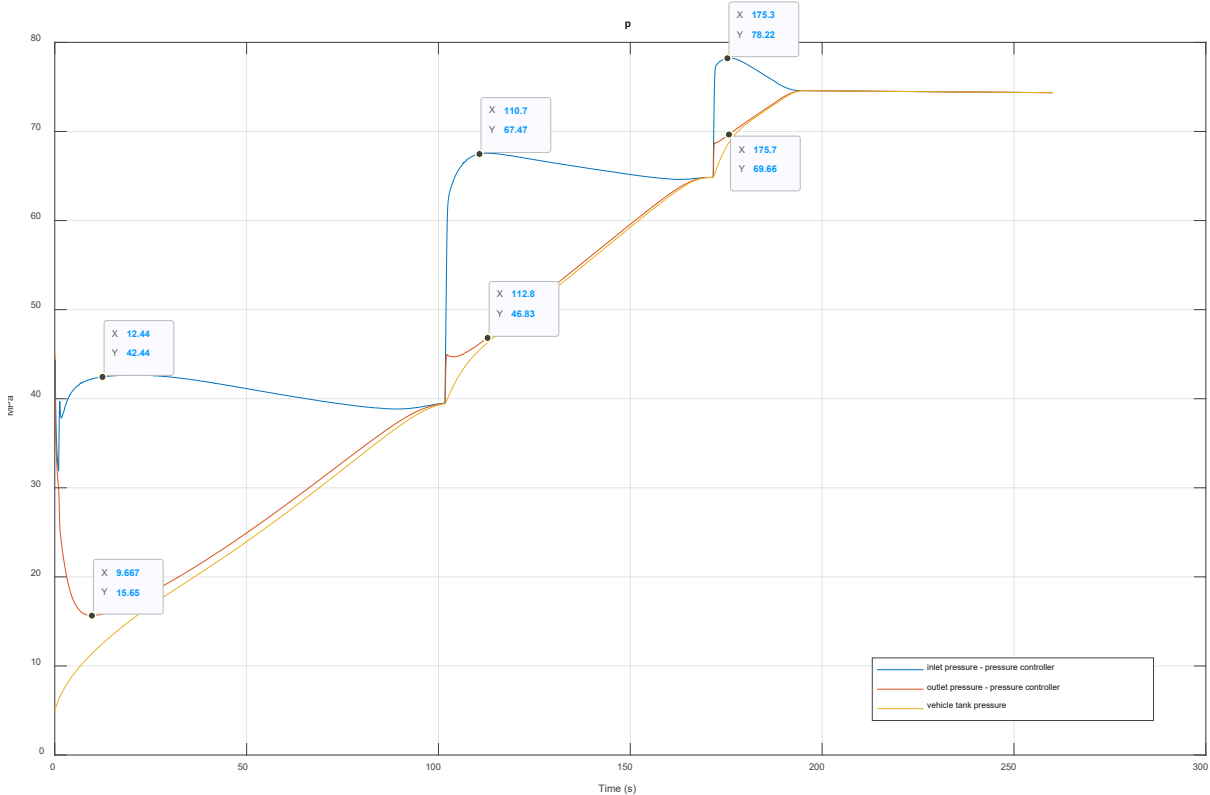


Figure 62: Pressure at the inlet and outlet of pressure controller, together with inner vehicle tank temperature

In figure 62, the behavior of the pressure gradients at the inlet and outlet of the pressure controller can be seen. Simultaneously with the switching of cascade tanks, the outlet pressure decreases in consequence of throttling and gas expansion.

The pressure controller's variable orifice rapidly closes to smaller orifice diameters, as soon as the pressure gradient of a recently opened cascade storage tank arrives at the inlet. This is the logical actuating consequence for preventing an abrupt acceleration of the hydrogen flow, once another fully charged cascade tank starts to supply with high pressure gradients.

The visible increase of pressure at the inlet for each tank switching is the slight *retaining of higher pressure gradients at the upstream side of the orifice*. This happens directly after the orifice diameter has reduced rapidly.

Extracting the essential insights gained for scenario 1, the following observations are valid throughout the entirety of scenario, and apply for all previously exemplified detail scenarios:

- The complete fueling procedure takes 3 minutes and 14.8 seconds for achieving the final pressure of 74.58 MPa
- The fueling phase of cascade tank 1 takes longest (39.58 s), while cascade tank 2 takes second longest (25.47 s) and cascade tank 3 shortest (9.52 s). This is due to the pressure initialization of 50-75-90 MPa of the three cascade storage tanks, in correlation with an initial vehicle tank pressure of 5MPa and an APRR of 21.8 MPa.

The insights obtained by analysis of scenario 1 will gain an informative value, once being compared with another typical fueling scenario. For the next subchapter, a second typical fueling scenario will be introduced. Its simulated thermodynamic properties will be exemplified and directly compared to the results of scenario 1.

5.1.2 Scenario 2

The second scenario displays another common fueling scenario for a passenger car. Its initial vehicle tank pressure provides for a filling level of 53.3%, which can be interpreted as half-full. The initial values of the fueling procedure are listed within table 5.

Cascade storage tanks

<u>Storage tank 1</u>		
p_{init} in MPa	T_{init} in K	V_{init} in L
50	313.15	750
<u>Storage tank 2</u>		
p_{init} in MPa	T_{init} in K	V_{init} in L
75	313.15	750
<u>Storage tank 3</u>		
p_{init} in MPa	T_{init} in K	V_{init} in L
90	313.15	750

Vehicle tank

p_{init} in MPa	T_{init} in K	V_{init} in L
45	293.15	150

$T_{ambient}$ in K	293.15
Fueling protocol category	H70-T40

APRR in MPa/min	21.8
$t_{simulation}$ in s	260

Table 6: Initial values of fueling scenario 2

The target values, read out of SAE J2601, only differ in the target pressure. In short, they are:

- The target pressure of the vehicle tank, according to category H70-T40 non-communication, shall be 71.9 MPa
- Considering the APRR of 21.8 MPa/min for a H70-T40 fueling protocol, the target fueling time must be 3min11s or less
- The maximum pressure level for the 4-7kg tank volume category is 80 MPa

Figure 63 shows the simulated pressure profile for fueling scenario 2.

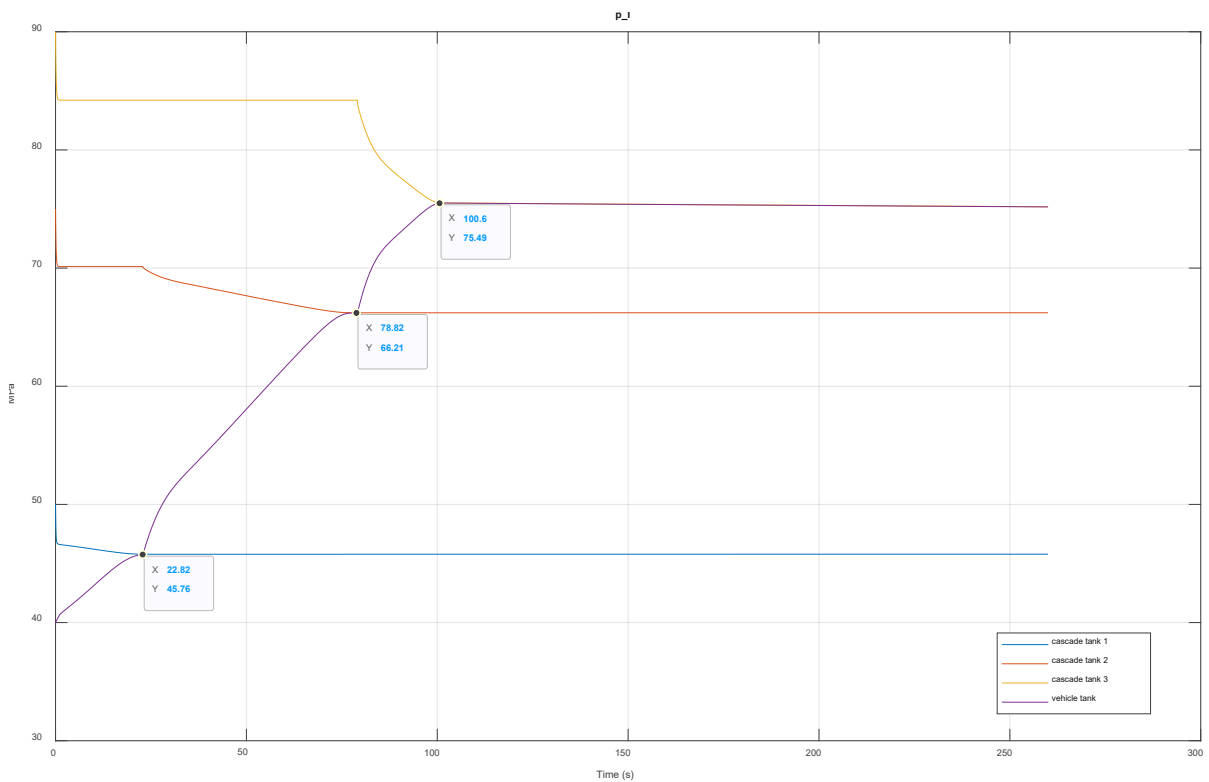


Figure 63: Pressure levels of an H70-T40 non-com fueling procedure, utilizing three cascade storage tanks and an initial vehicle tank pressure of 40 MPa

The two major observations made are:

- The target pressure of 71.9 MPa becomes overreached by 3.59 MPa. Since the maximum operating pressure, as introduced in 3.1.2, allows for maximum pressures of 87.5 MPa in our scenario as the upper pressure safety limit, the rather slight overreaching 3.59 MPa is acceptable as an expectable fueling impreciseness.
- The fueling phases of the cascade tanks change according to the higher initial vehicle tank pressure. Therefore, cascade storage tank 2 fuels the longest period of time, while cascade tank 1 and 3 reach pressure equalization soon after being connected.

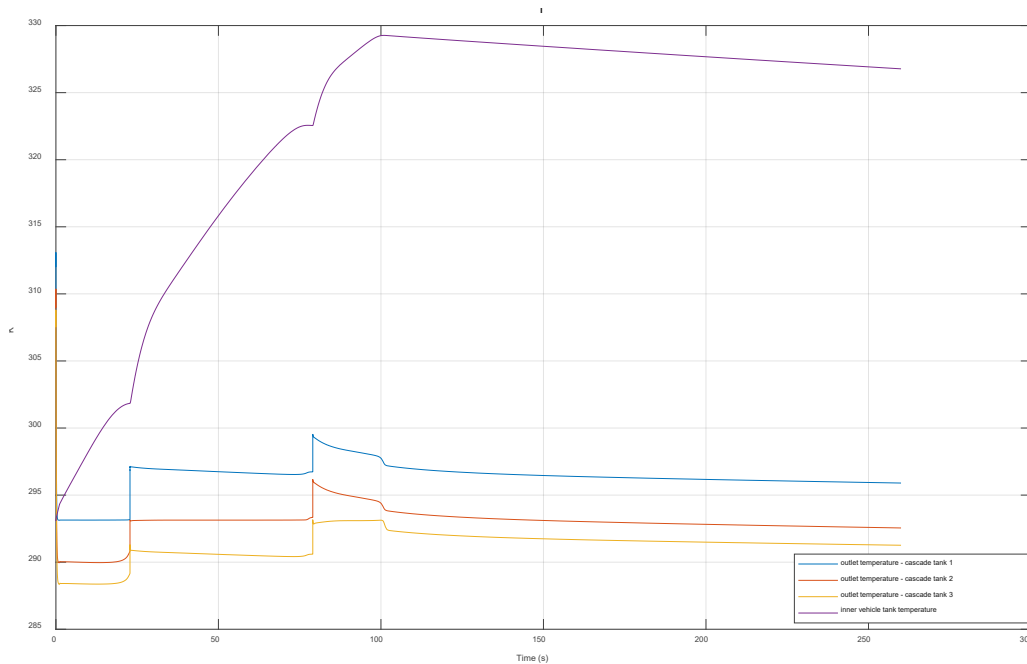


Figure 64: Temperature development, simulated at the cascade tank outlets, and the inside of the vehicle tank

The temperature development at the outlets of the cascade tanks, as well as their mass flow rates show no remarkable quantitative changes or deviations, compared to their counterparts of scenario one.

Figure 64 and 65 both show the simulation results for the cascade tanks' outlet temperature and mass flows.

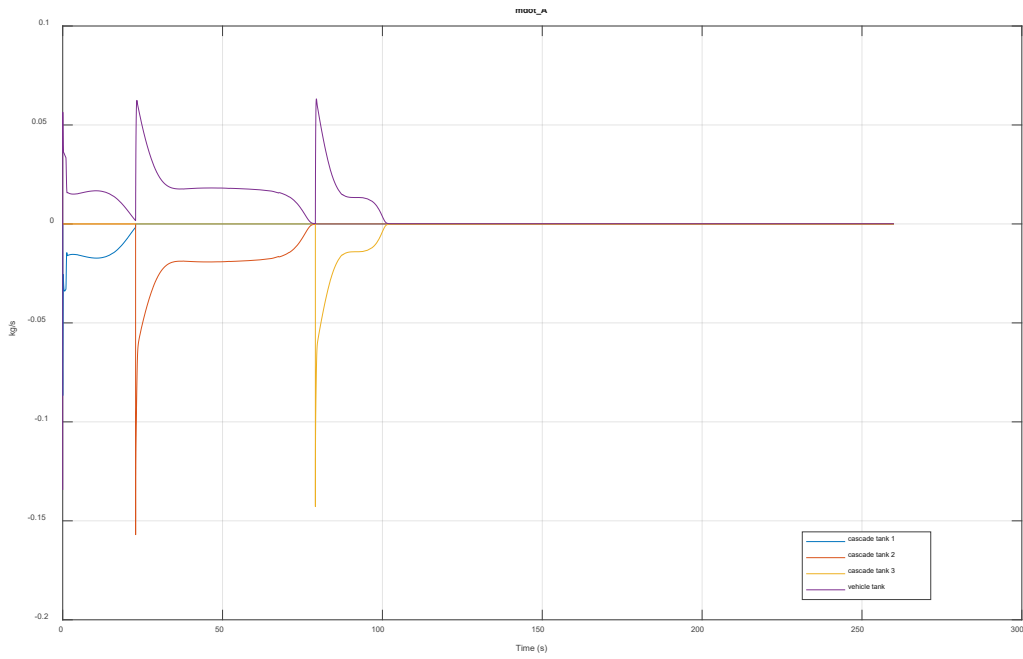


Figure 65: Progress of mass flow rate for an H70-T40 fueling and 40 MPa initial vehicle tank pressure, using three cascade tanks

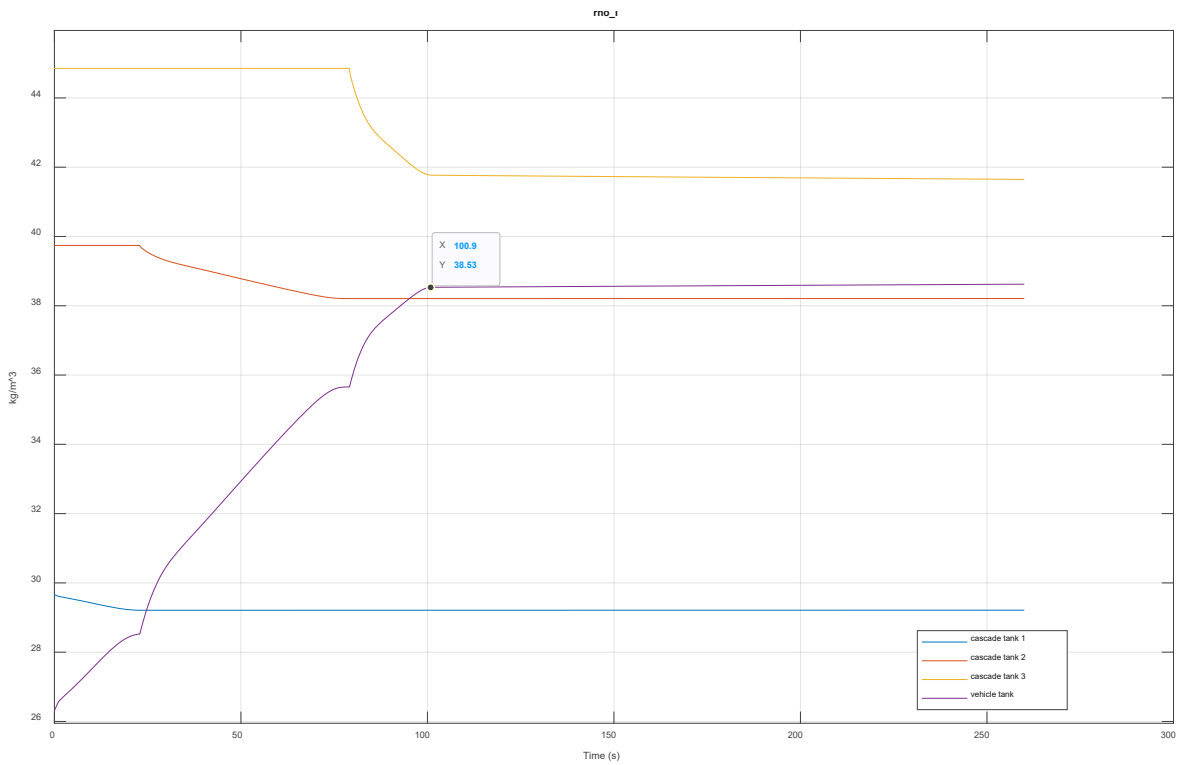


Figure 66: Density gradients, simulated inside of cascade tanks and the vehicle tank (initial pressure: 40 MPa)

Comparing the density gradients of fueling scenario 1 and 2, the final density of scenario 2 is slightly higher, measuring $38.53 \frac{kg}{m^3}$. The minor overreaching of the target pressure of scenario 2 is the most probable cause for this circumstance. Neither vehicle tank volume, nor the APRR applied did change, which could have been alternative probable causes.

The final density of $38.53 \frac{kg}{m^3}$ is very close to the maximum allowable density for H70-T40 fueling procedures of $40.2 \frac{kg}{m^3}$, and indicates high overall performance of the model.

Both convective and conductive heat flow rates of figure 67 and 68 show no major deviations to its counterparts of scenario 1. One observation is nevertheless worth-mentioning:

The positive-signed convective heat flow rate at the thermal port of pipe section “dispenser” needs longer to be neutralized by the cooling power of the heat exchanger. A possible reason for this could be the more abrupt decrease of instant cooling after the cascade tank switch, as visible in figure 63. In the comparable counterpart of figure 53, the decrease of *instant cooling* happens more dynamic in absence of a significant breaking-in, as in figure 67.

Therefore, scenario 1 distributes both its *instant* and *actuated cooling* power more evenly. The heat generated within the dispenser can be neutralized faster thereby.

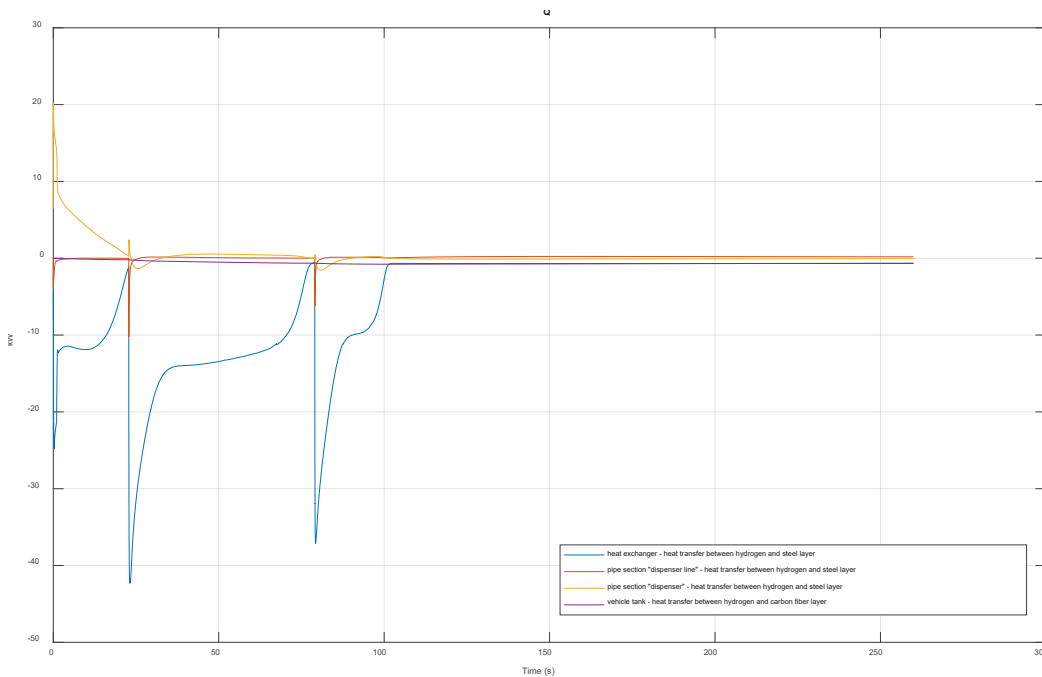


Figure 67: Convective heat flow rates between hydrogen flow and the components' innermost layers

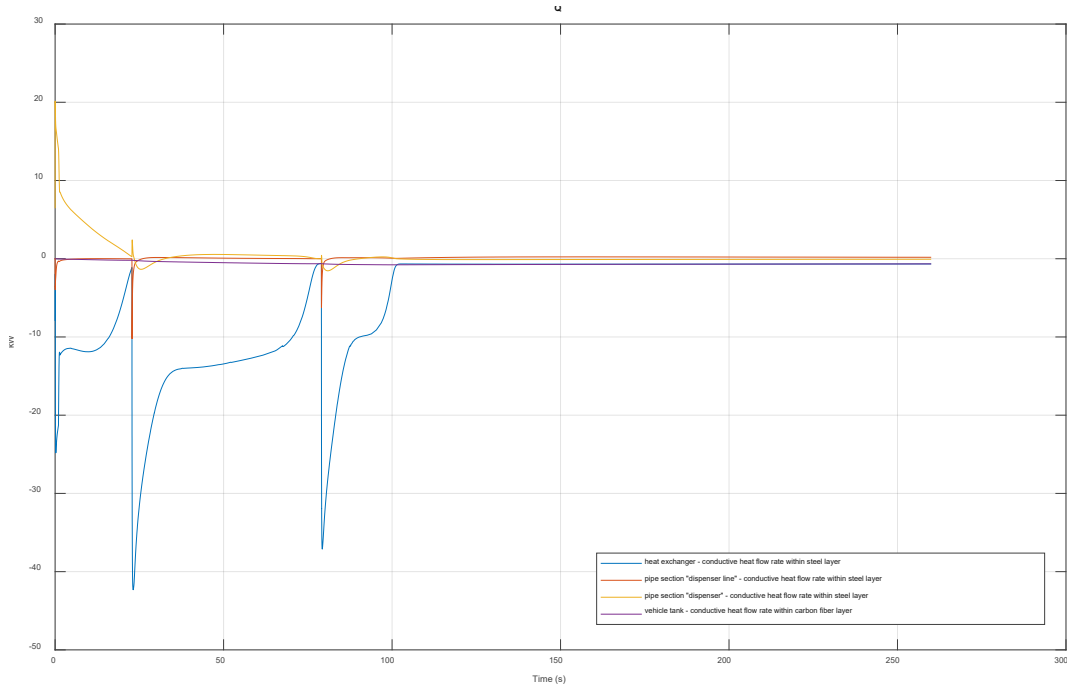


Figure 68: Conductive heat flow rate through the components' steel or carbon fiber layers

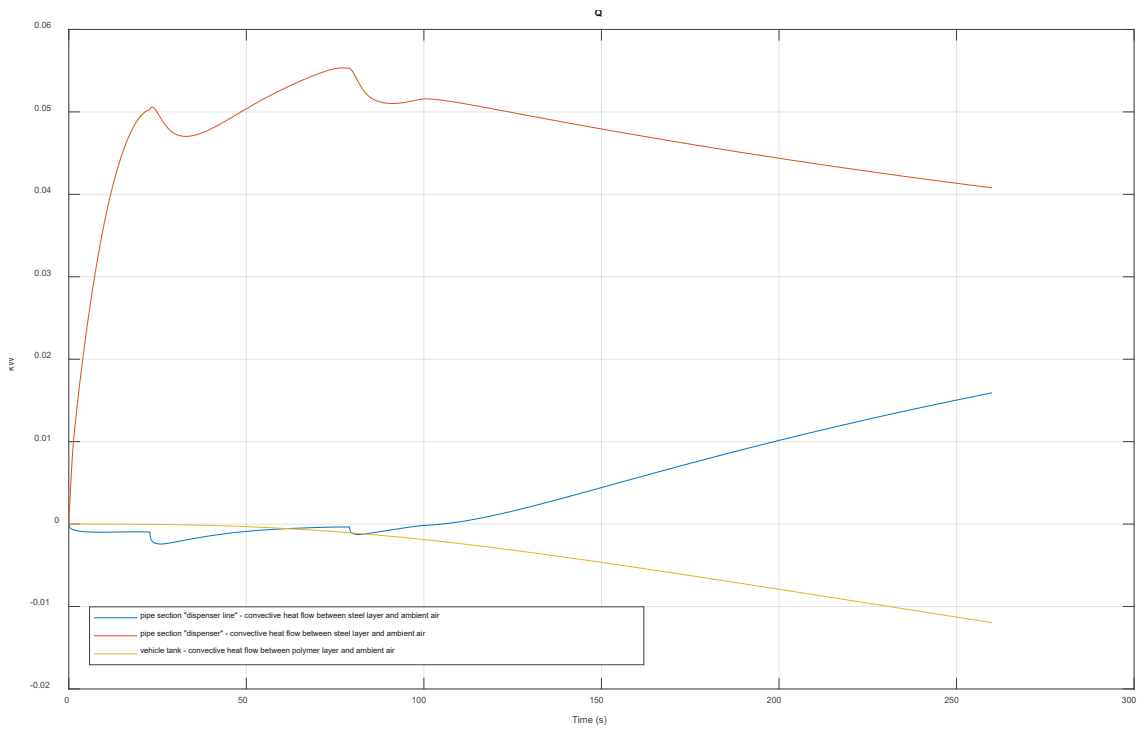


Figure 69: Convective heat flow rates between outermost components' material layers and the environment

Similar to scenario 1, the convective heat transfer between the outermost components' material layers and the ambient air is lower by a factor 500, compared to the convective heat transfer from hydrogen to the innermost steel liners. The course of the simulated data points show are coherent with the fueling set-up of scenario 2, and show no segments of special behavior, compared to figure 55.

Figure 70 reflects the more pronounced effects of *instant* and *actuated cooling* of scenario 2. Conductive and convective heat transfer rates through the material layers of the heat exchanger experience more pronounced peaks, followed by more abrupt declines.

These more pronounced effects visible in figure 53, 67, 68 and 70 are probably not linked to any changes in operating parameters. A shorter total fueling time for scenario 2 leads to a more “compressed” and compact display of the trends in figure 70, while the simulation time of 260 s is unchanged.

Also within scenario 2, the heat exchanger block reaches an idling temperature of 256 K, yet it does not achieve its predetermined ideal cooling target temperature of 233 K. Figure 72 shows this reoccurring issue for scenario 2.

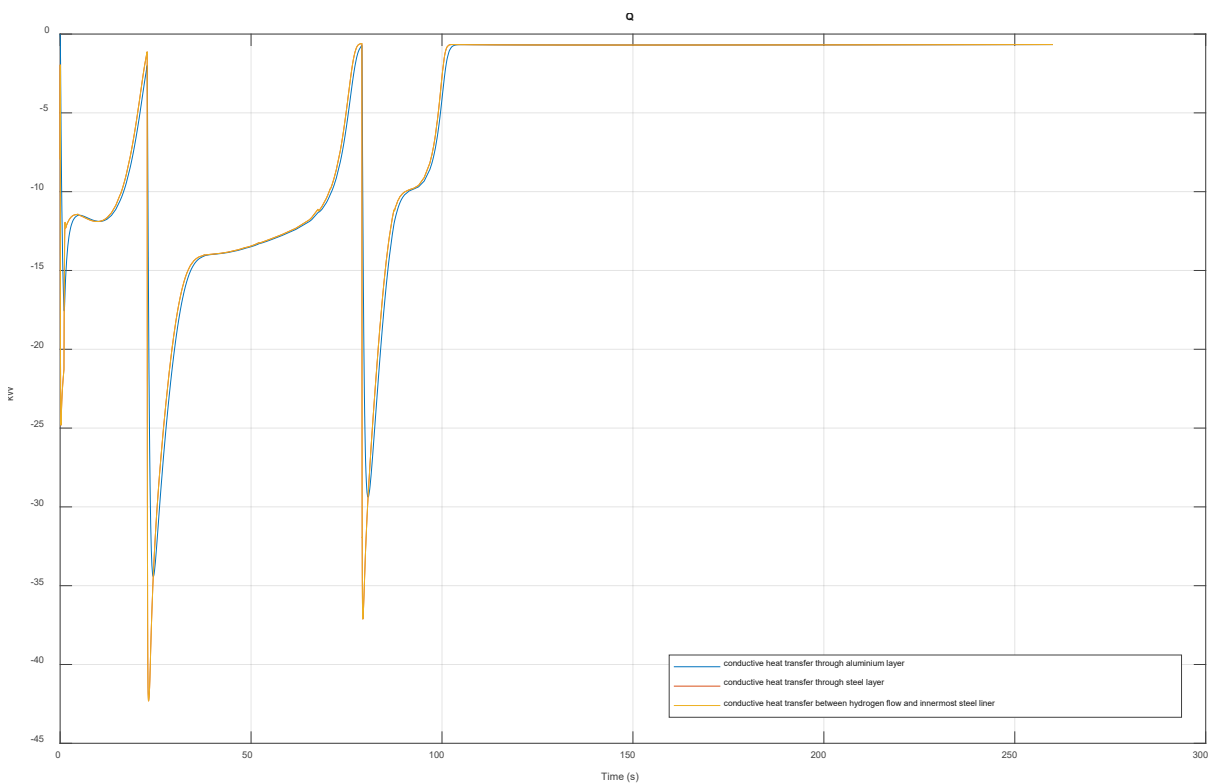


Figure 70: Conductive and convective heat flow rates through the material layers of the heat exchanger

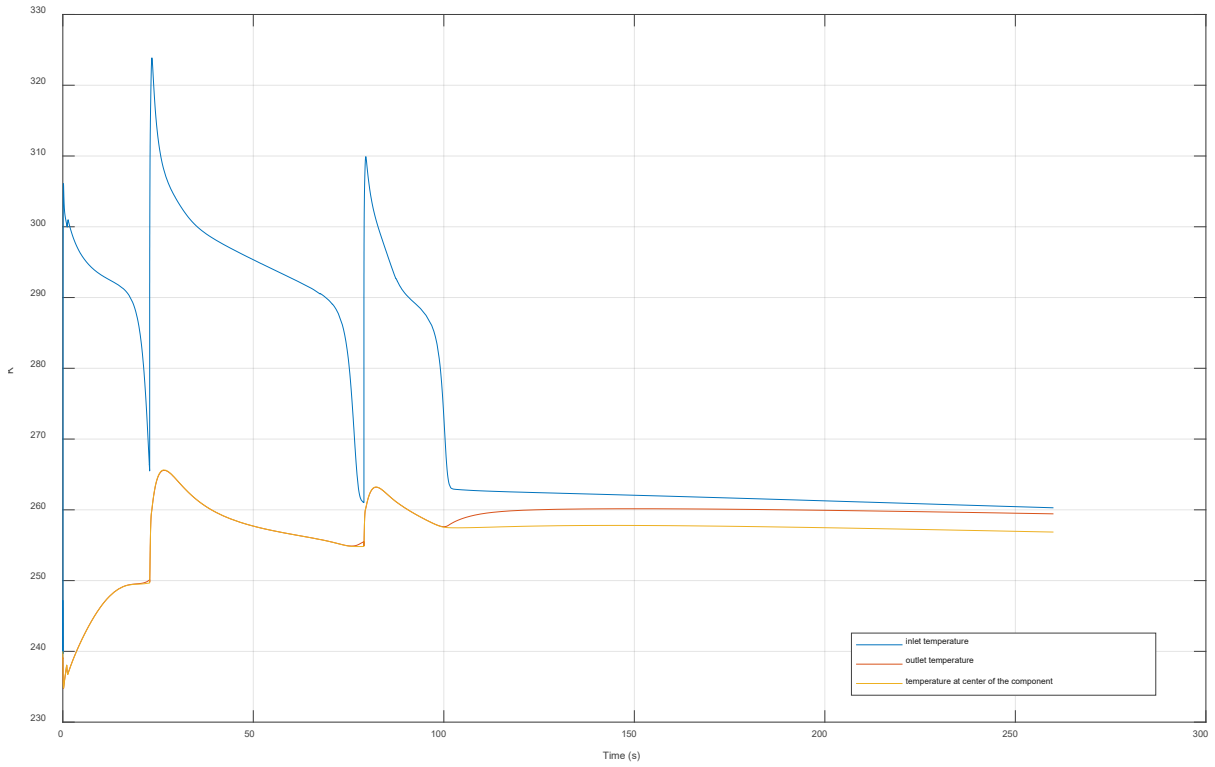


Figure 71: Temperatures at the inlet, outlet and center of heat exchanger block

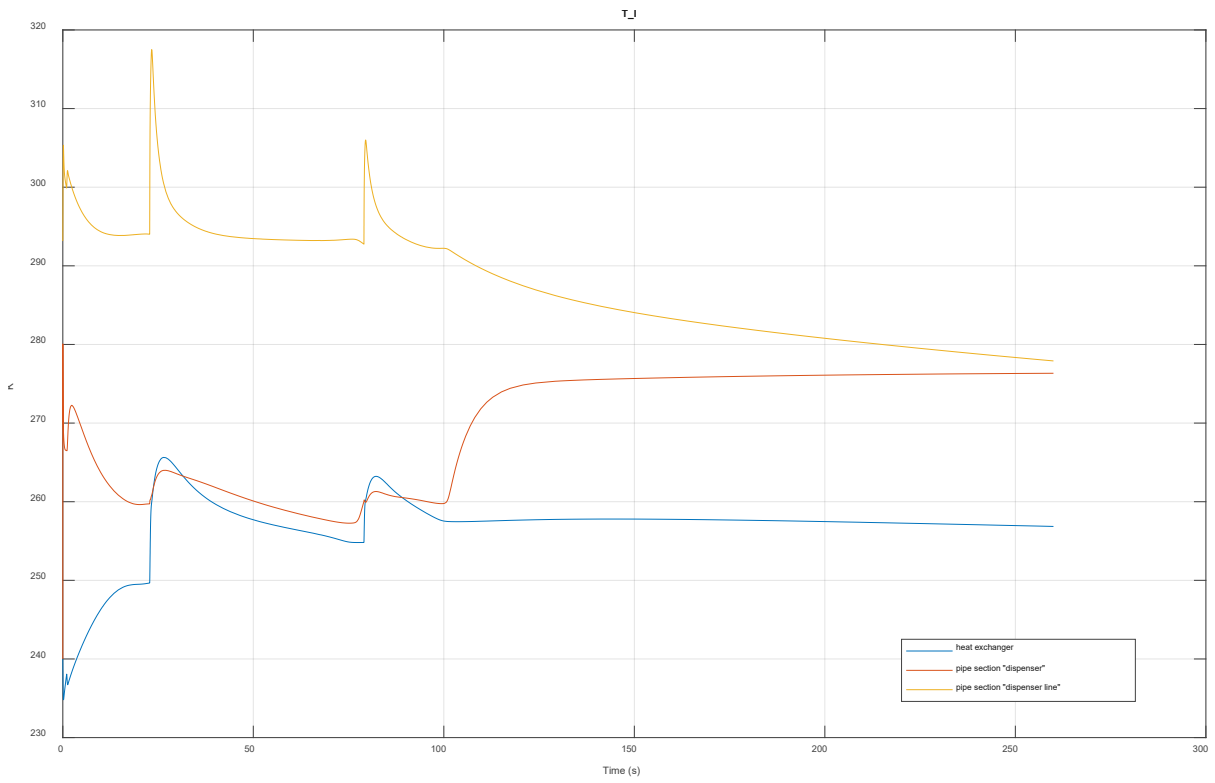


Figure 72: Temperatures inside of heat exchanger and pipe sections "dispenser line" and "dispenser"

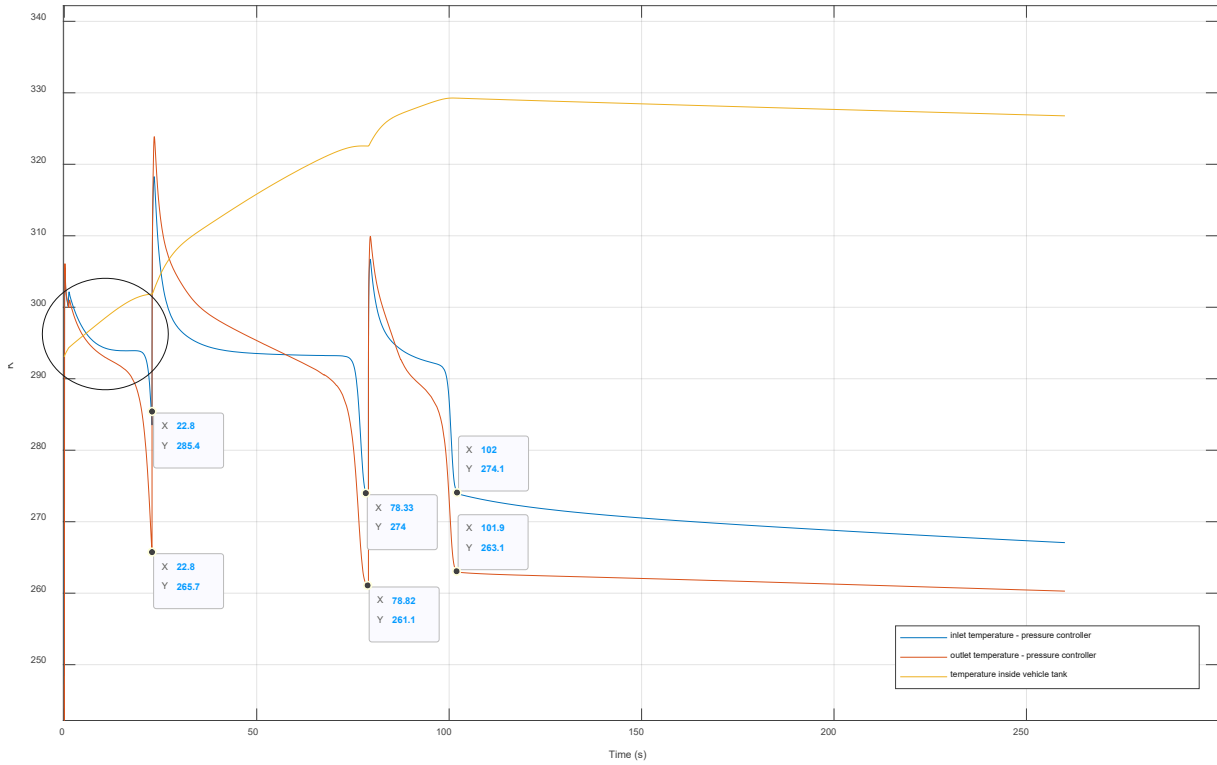


Figure 73: Temperatures at the inlet, the actuating orifice diameter and the outlet of pressure controller

Figure 73 shows the temperature gradients at the inlet and outlet of the pressure controller for scenario 2, together with the inner vehicle tank temperature.

While the inlet temperatures are lower for the second and third cascade tank fueling phase, the outlet temperature during the first cycle is lower than its corresponding inlet temperature (see encircled segment). This correlates not to the expected higher outlet temperature at the beginning of a fueling phase. In the expected case, the hydrogen flow should experience by throttling and subsequent expansion at the first segment of each cascade tank fueling phase.

Despite of thorough investigation, the causes for this minor deviation from expectable simulation results could not be identified until now.

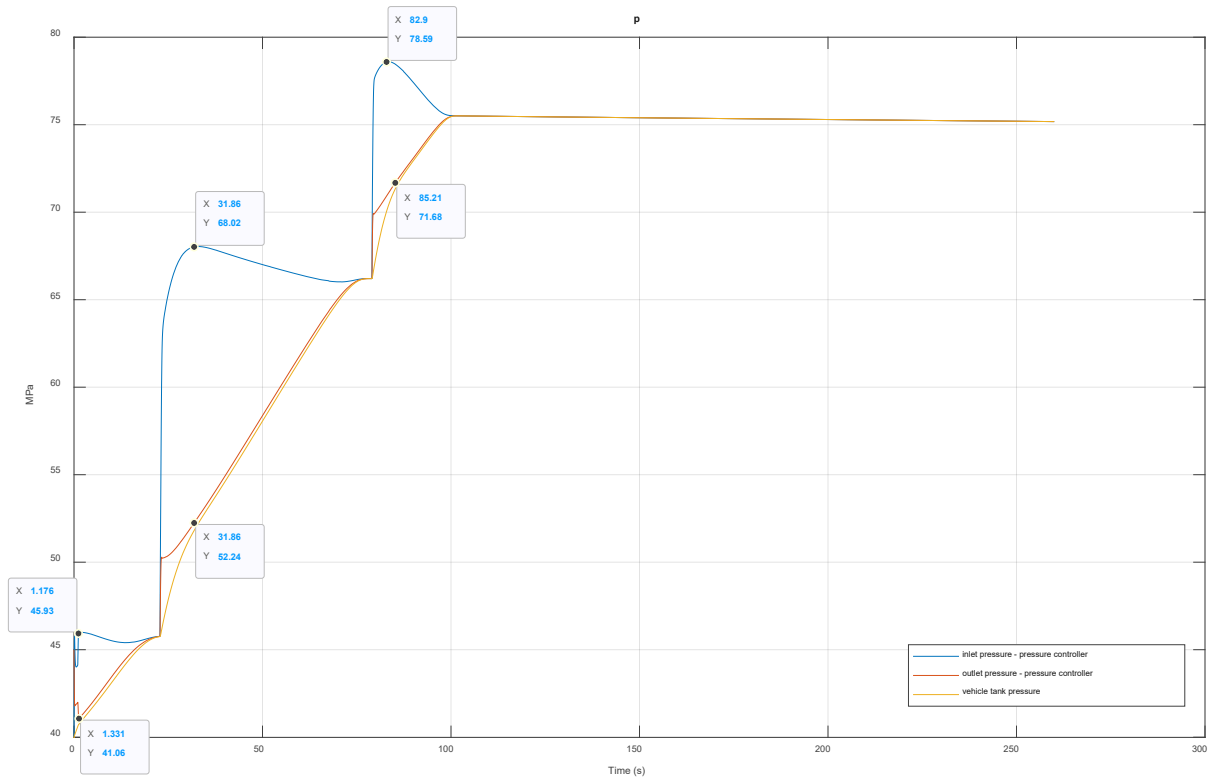


Figure 74: Pressure at the inlet and outlet of pressure controller, together with inner vehicle tank temperature for scenario 2

Figure 74 displays the inlet and outlet pressure trends of the pressure controller for scenario 2.

In coherence with scenario 1 and figure 62, the pressure controller's orifice rapidly closes to smaller orifice diameters, as soon as the pressure gradient of a recently opened cascade storage tank arrives at the inlet. This causes a slight *retaining* or "backing-up" of higher pressure gradients at the upstream side of the orifice, and therefore an increase of pressure at the controller inlet. No special deviations to the expectable behavior could be discovered within figure 74.

Extracting the essential insights gained for scenario 2, the following observations are independent of the results of scenario 1, and apply for all previously exemplified detail scenarios:

- The complete fueling procedure takes 1 minute and 40.6 seconds for achieving a final pressure of 71.9 MPa
- The fueling phase of cascade tank 2 takes longest (56.0 s), while cascade tank 1 takes second longest (22.82 s) and cascade tank 3 shortest (21.78 s).

5.1.3 State of Charge

In the course of analyzing and comparing the simulation results of scenario 1 and 2, the State of Charge - SOC – is a central parameter within the scope of hydrogen fueling, and shall be exemplified here for both fueling scenarios.

By definition, the SOC is the ratio between

- the measured vehicle tank pressure at a uniform gas temperature of 15 °C, and
- a reference density, defined for 15°C and the NWP of the corresponding fueling protocol category.

It reads

$$SOC = \frac{\rho(p, T)}{\rho(NWP, 15^{\circ}C)} * 100\% \quad (5.1)$$

The NWP amounts to 70MPa for all H70-T40 fueling protocol category scenarios. The plotted SOC trends are displayed in figure 75.

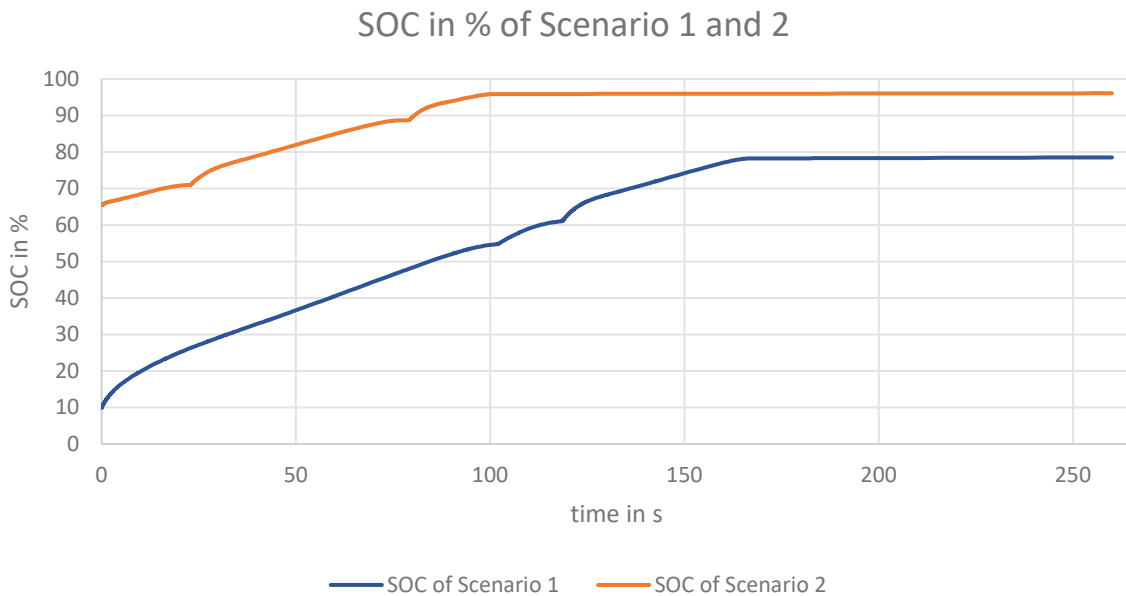


Figure 75: SOC percentages for fueling scenario 1 and 2

It can be observed that fueling scenario 1 starts with initial 9.9% SOC and reaches up to 78% final SOC, while fueling scenario starts higher at 65% SOC and reaches 96% final SOC. As already briefly explained in 5.1.3 and 5.1.4, the initial vehicle tank pressure levels contribute for the major part to both the course and final percentages of SOC.

5.2 Scenario variations

For the purpose of simulating possible disturbance reactions of already commercially available fueling station designs, this chapter analyzes the simulation results of two probable incidents, based on the underlying Simscape physical component system. The reference fueling scenario for all comparison efforts of case 1 and 2 is fueling scenario 1, as introduced in 5.1.1.

5.2.1 Case 1: Outage of Heat Exchanger

In case of a total interruption of cooling power supply by the heat exchanger, the following observations can be obtained, as visible in the plots figure 76, 77, 78, 79 and 80:

- The pressure gradients proceed identically, compared to the case of an operating heat exchanger. Therefore, the SOC must be identical in value, and therefore has not been plotted.
- The overall fueling time is 2 seconds longer
- The final vehicle tank temperature is by 63.55 K higher than in case of an operating heat exchanger
- The achieved final vehicle tank density is $0.3-0.4 \frac{kg}{m^3}$ lower, compared to the case of an operating heat exchanger

The final vehicle tank temperature of case 1 makes the major effect of a total outage visible: The final vehicle tank temperature overreaches the maximum allowed operating temperature of 358.15 K by far. This circumstance is expectable, and an even higher increase of the vehicle tank temperature can be expected, due to the following observation:

Compared to the cooling power of the ACF unit of the real fueling station, the cooling power of correlating component block can deliver only a fraction of the available ACF unit cooling power. The block component's simple structure and realization are the main reason for this discrepancy. More complex and elaborated heat exchanger block models would have resulted in significantly higher susceptibility to divergence behavior and consecutive simulation errors. By implementing the heat exchanger block in the structure of a simple plate heat exchanger, a high measure of basic robustness can be provided for all simulation efforts.

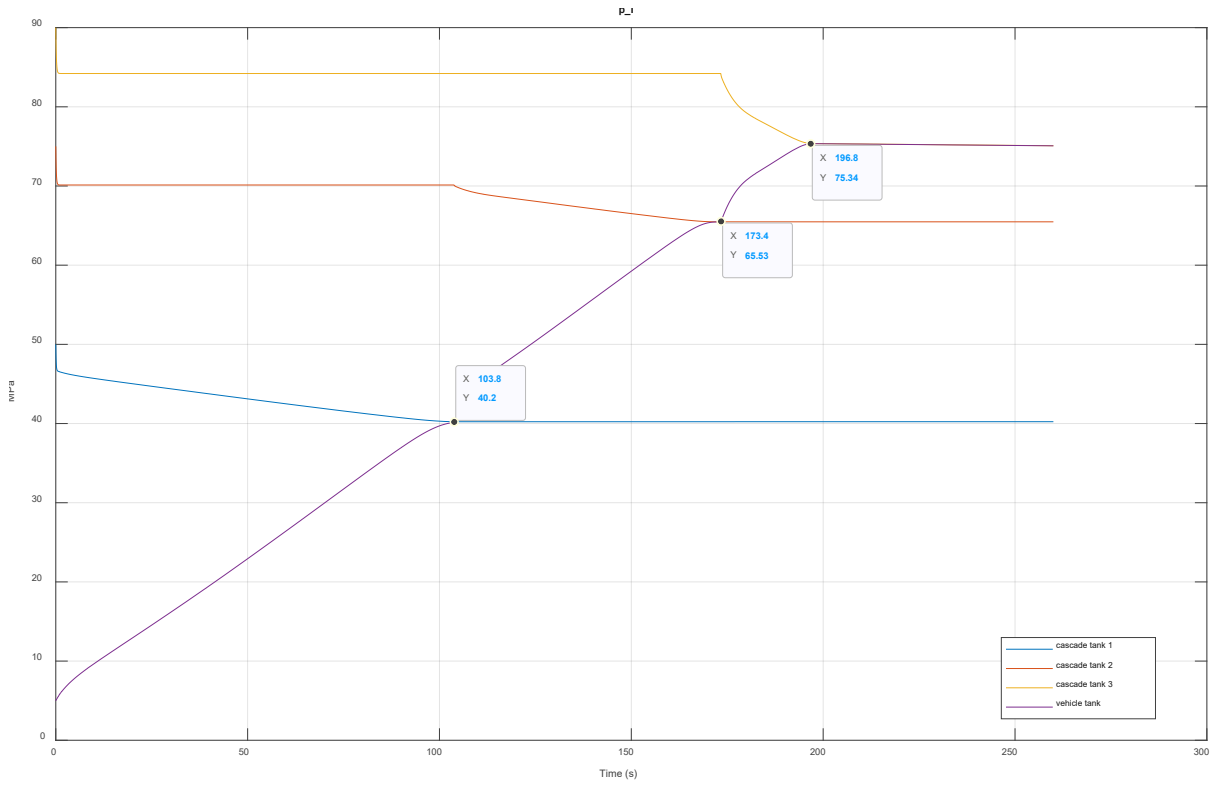


Figure 76: Pressure profiles of the cascade tanks and the vehicle tank in case of an outage of the heat exchanger

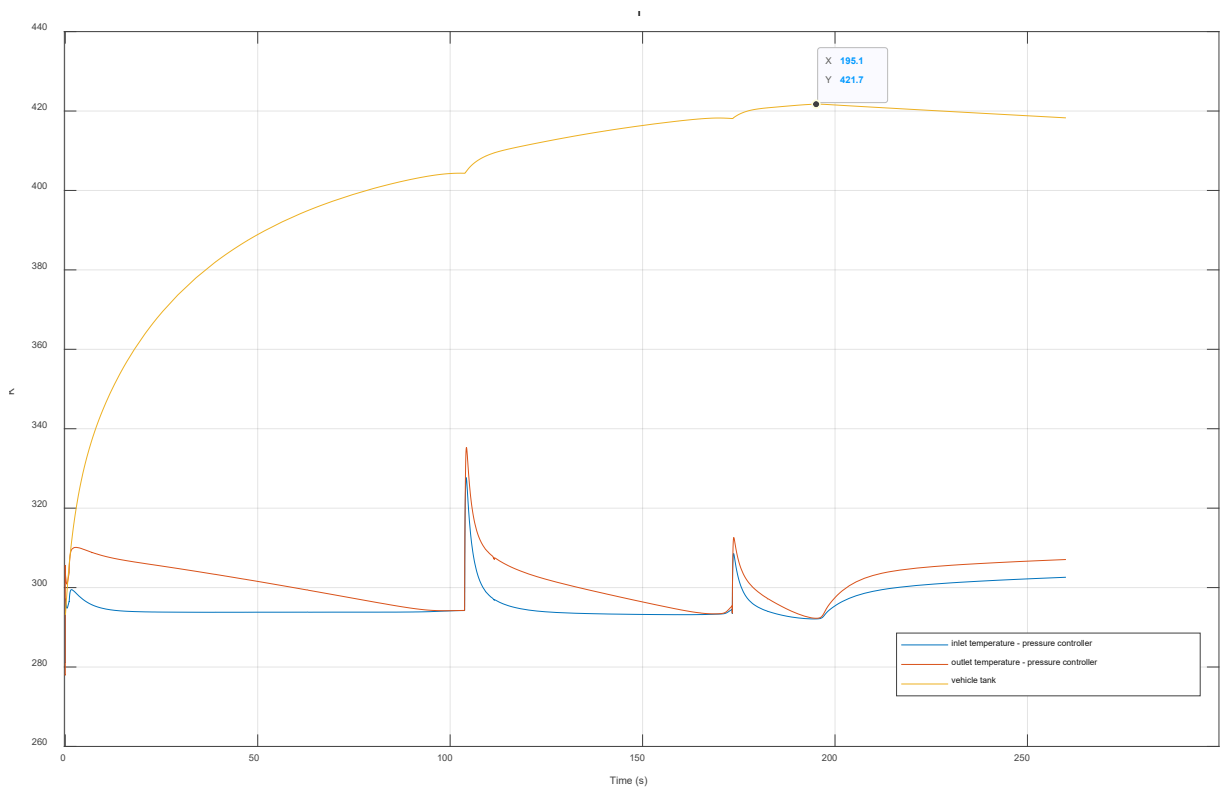


Figure 77: Temperature profiles of the inlet and outlet of the pressure controller, and the vehicle tank in case of an outage of the heat exchanger

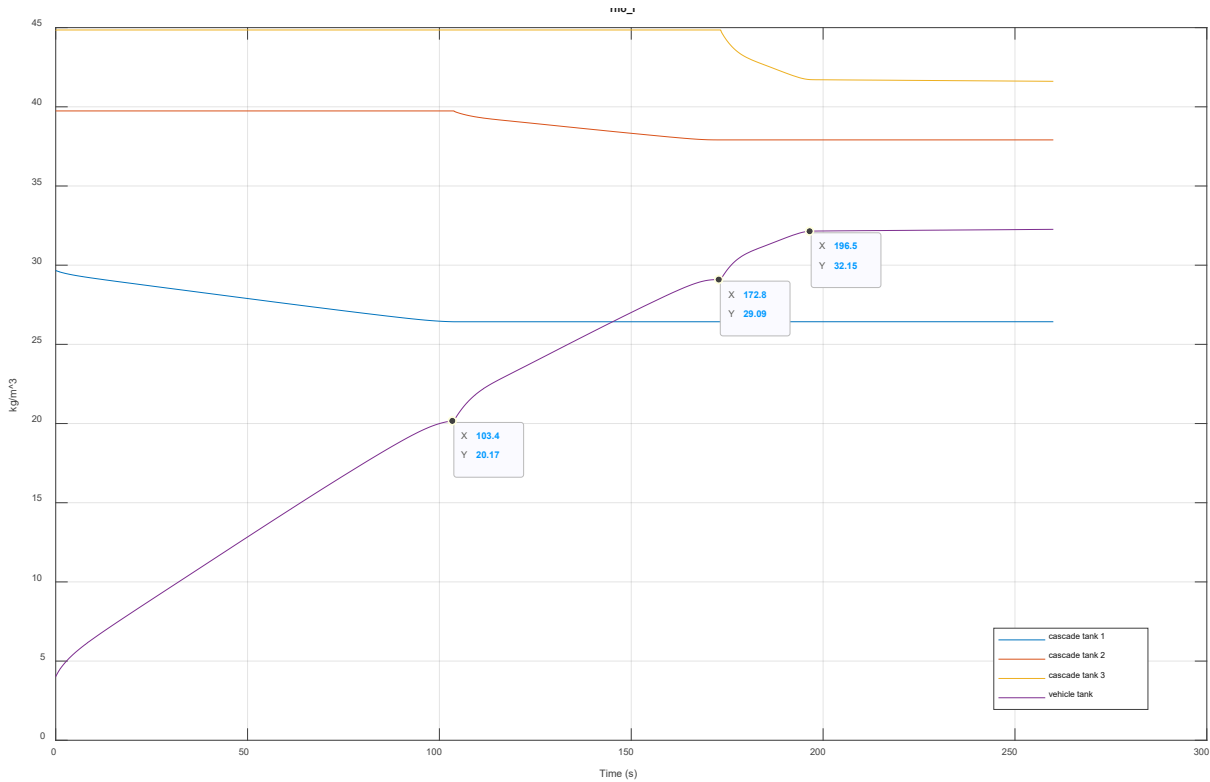


Figure 78: Density profiles of the cascade tanks and the vehicle tank in case of an outage of the heat exchanger

As shown in figure 79, a “convective heat transfer” block’s positive direction is from port A to port B. This means that the heat flow is positive if it flows from A to B.

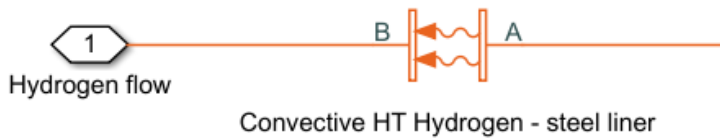


Figure 79: Block positive direction of a “convective heat transfer” block

By observing figure 80, it becomes visible that the convective heat flow for pipe section “dispenser”, generated by hydrogen throttling, shows much higher negative values than in scenario 1 and corresponding figure 81. The heat of expansion, usually equalized by the heat exchanger’s cooling energy, now dissipates without any cooling into the surrounding steel layer of the dispenser channel, taking the most direct route to equalize its heat capacity. Figure 81 shows the compared scenario, using a properly working heat exchanger.

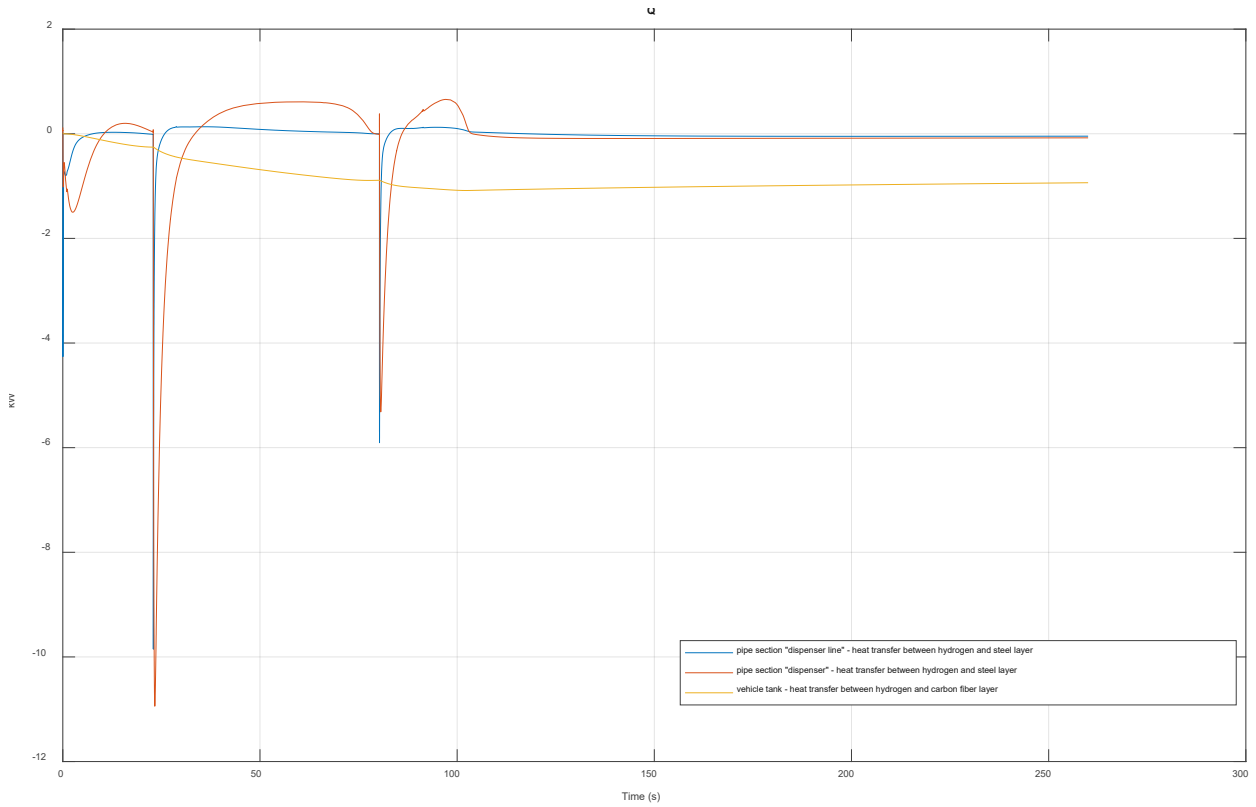


Figure 80: Convective heat flow rates between hydrogen flow and the components' innermost layers – case 1, outage of heat exchanger

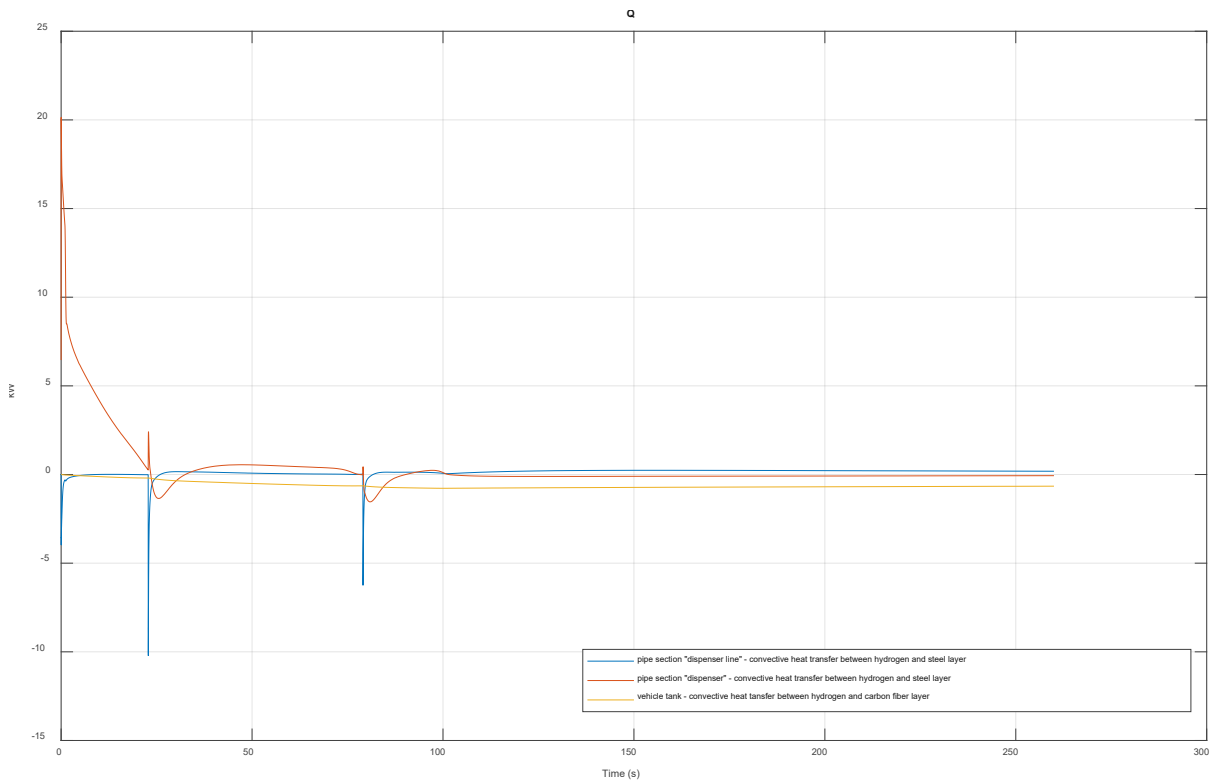


Figure 81: Convective heat flow rates between hydrogen flow and the components' innermost layers – fueling scenario 1, heat exchanger supplies cooling power

5.2.2 Case 2: Changing the controller's control parameters

In case of an actualization of the controller's control parameters in the course of a possible PLC unit reset, the pressure controller's general required abilities, such as *regulation* and *command tracking* are likely to be decreased or even dissolved completely. [54] More important than e.g. overshooting the setpoint of a control variable or the resulting energy expenditure of certain control behavior, the **reactiveness** of the controller contributes the largest part to the fueling station's control behavior

In case of an erroneous readjustment of the controller parameters, two possible outcomes emerge in sole consideration of reactivity:

- The pressure controller actuates faster than desired. This can either result in either
 - more efficient tank switching, due to even higher speeds of orifice adjustment, or
 - undesired overshooting of the fueling ramp rate signal, thus resulting in abortion of the fueling procedure
- The pressure controller actuates slower than desired. This can result in
 - instantaneous abortion of the fueling procedure, as soon as the fueling ramp rate leaves the pressure tolerance corridor, as explained in 3.1.4.
 - delay and idling for each tank switching, due to the controller's decreased capabilities of narrowing and widening the pressure controller's orifice accurately fast during tank switching

Since the overall efficiency of the fuel station's performance, especially its part of tank switching mechanism is of major interest within this work, the latter case of slowed reactivity will be simulated.

In order to change the actual controller settings of a "PD-controller" to a slower configuration, the P-component will be increased, resulting in a

- decreased rise time – in this case equivalent to steeper pressure ramp rates, besides
- *steady state errors* – equivalent to *idling times during the execution of a tank switch* [55]

This configuration is accomplished by increasing the P-component by a factor 100. The following observations can be gained by investigating the selection of simulation results, displayed in figure 82 and 83:

- The fueling procedure remains between 7 and 11 seconds in an idling mode before completing the corresponding tank switching process, and opening the orifice for the pressure supply of the subsequent cascade tank
- The utilized slopes of the pressure ramp rate are steeper. Therefore, the overall fueling time amounts to only 1 minute and 32 seconds. This shortening of overall fueling time also brings along a potential factor of instability for the control system: Following steeper pressure ramp

rate slopes increase the risk to hit the upper boundary of the pressure tolerance corridor, and therefore an abortion of the overall fueling procedure.

- The final fueling temperature measures 2-3 K higher, compared to fueling scenario 1.
- The final vehicle tank pressure amounts to 75.63 MPa, which is almost coherent to the final vehicle tank pressure of fueling scenario 1, measuring 74.58 MPa. Hence, the SOC of case 2 must amount approximately 65%, and will not be plotted separately. Despite of steeper pressure ramp rate slopes, the final vehicle tank pressure remains almost unchanged. Preceding estimations, without any distinct simulation efforts, would probably suggest a significant change of the final vehicle tank pressure, which is not the case.

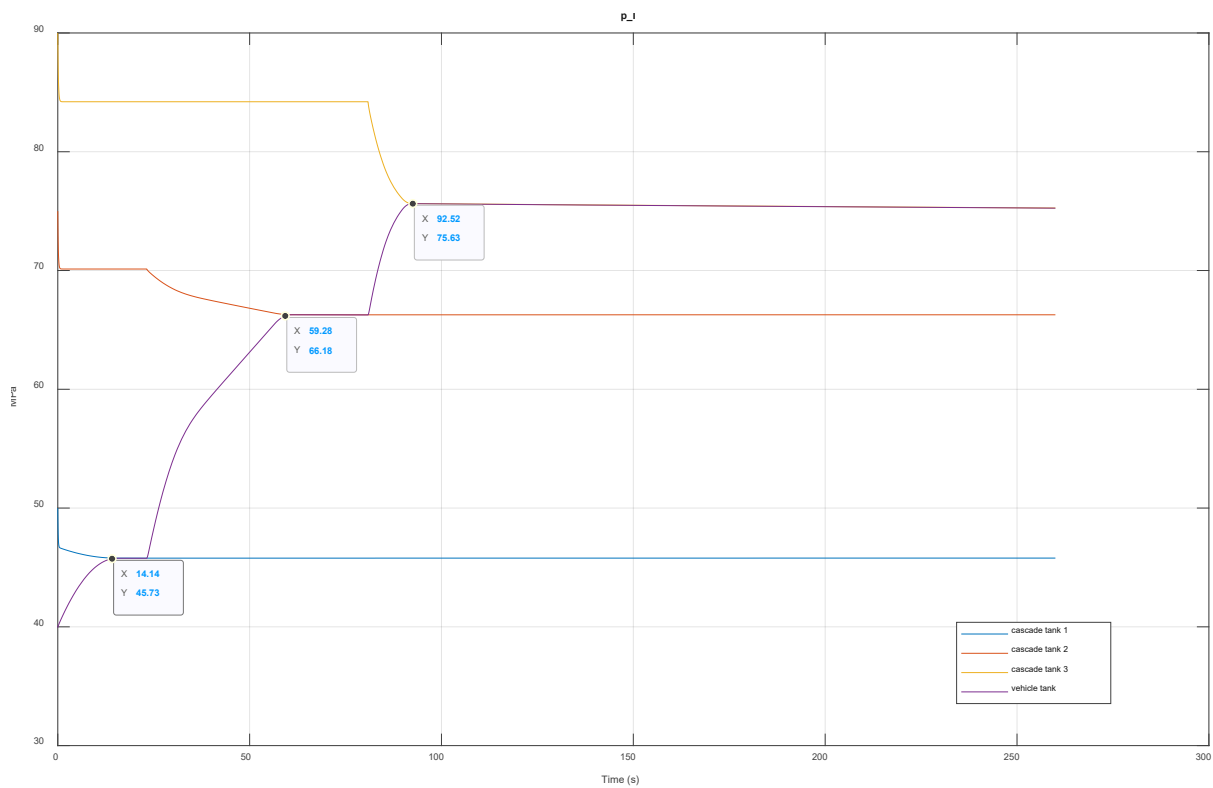


Figure 71: Pressure profiles at the outlets of the cascade tanks, and the inside of the vehicle tank in case of a change of the control parameters

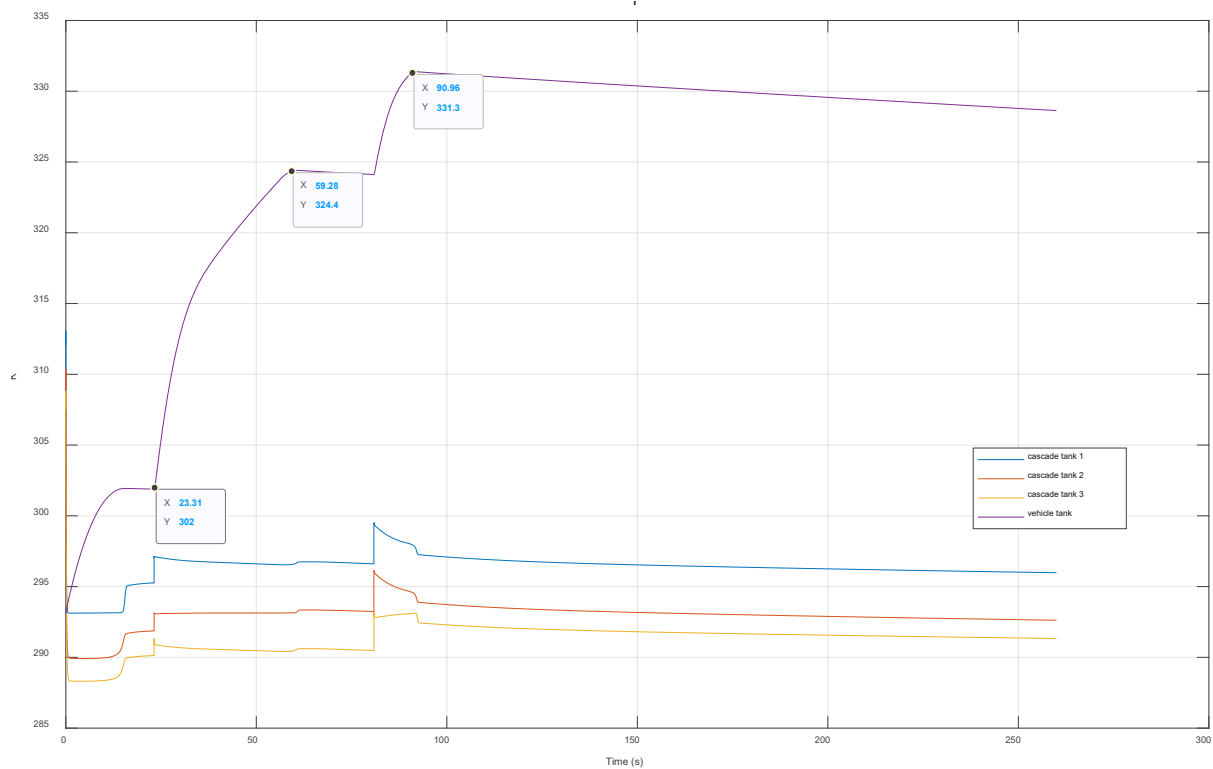


Figure 82: Temperature profiles at the outlets of the cascade tanks, and the inside of the vehicle tank in case of a change of the control parameters

6. Conclusions and further work

The overall scope of research of this work was to gain raw data, and hence a better understanding of an existing design of hydrogen fueling station through the creation and application of a simulation tool. All sub aims and requirements of the scope of this work could be met. The plots of the simulation results prove the plant performance, as expected by the company's research staff. The tool itself behaves robust and converges almost consistently for the case of simulating passenger car fueling procedures.

Besides the creation of a commercially applicable simulation tool, two real-world fueling scenarios have been analyzed in the approach of a scientific parameter study. The trends of thermodynamic properties of each scenario have been compared. Numerous expectable detail scenarios could be affirmed.

On the other hand, the simulation results reveal room for improvement for certain tasks of the simulation tool. For example, a refined and more detailed implementation of the heat exchanger model block will be necessary to display higher cooling supply also during idling times of the plant.

Two independent cases of disturbances have been simulated as well. The corresponding results not only deliver the most expected degree of disturbance behavior, but also deliver high resolution plots. The simulation tool's results offers higher degrees of detail and informative value for plant failure scenarios ("most conservative cases"), compared to the existing calculations of the company.

6.1 Further work

In order to provide for accurate outlet temperature during operation and especially idling times, the heat exchanger model block has to be revised with the intent of receiving uninterrupted cooling power, measuring 233 K, at the heat exchanger outlet. A model block of a tube bundle heat exchanger would be a feasible alternative.

A possible consecutive research project could be the technical economic analysis, which has been originally proposed to be a second major part of this master thesis project. An overall refinement and upgrading of the simulation tool by adding a supply unit and a set of compressors, as sketched within the left part of figure 18, would be another option of proceeding.

Although the hydrogen economy still demands further extensive research effort, and – equally important – efforts and trust of investors, hydrogen technologies are undeniably going to be central and game-changing technologies of the future. All present simulation efforts contribute to an improvement of the underlying product's price-performance ratio. This furthermore supports its competitiveness at the open market, and adds to its growing market demand.

Finally, it can be summed up that all commercially available applications of hydrogen technology need to experience an enhancement of their price-performance ratio, as well as elaborate development of overall performance, error-free availability and intra-sectional coupling possibilities – if the world aspires to experience a transition to sustainable energy technologies.

Through the simulation tool created within this work, another mosaic shall be provided in enhancing a promising technology for present and future.

References

- [1] „Worldometer,“ 02 2019. [Online]. Available: <https://www.worldometers.info/world-population/>.
- [2] M. Klell, H. Eichsleder and A. Trattner, *Wasserstoff in der Fahrzeugtechnik: Erzeugung, Speicherung, Anwendung*, Wiesbaden: Springer Wiesbaden, 2018.
- [3] W. E. Council, „World Energy Resources 2016,“ Cornhill, London, 2016.
- [4] L. Barreto, A. Makihiro and K. Riahi, „The hydrogen economy in the 21st century: a sustainable development scenario,“ in *International Journal of Hydrogen Energy* 28, 267–284, 2003.
- [5] D. Haeseldonckx and W. D’haeseleer, „Concrete transition issues towards a fully-fledged use of hydrogen as an energy carrier: Methodology and Modelling,“ in *International Journal of Hydrogen Energy* 36 (2011), 4636-4652, University of Leuven, Belgium, 2011.
- [6] W. McDowall and E. M., „Forecasts, scenarios, visions, backcasts and roadmaps to the hydrogen economy: A review of the hydrogen futures literature,“ in *Energy Policy* 34 (2006), 1236-1250, Policy Studies Institute, London, UK, 2006.
- [7] J. T. Kiehl and T. K.M., „Earth's Annual Global Mean Energy Budget,“ in *Bulletin of the American Meteorological Society* 78 (2), S. 197–208, Boulder, Colorado, USA, 1997.
- [8] R. P. a. L. M. Core Writing Team, „Climate Change 2014: Synthesis Report - Fifth Annual Report,“ in *Contribution of Working Groups I, II and III to the Fifth Assessment Report of the IPCC*, Geneva, Switzerland, 2014.
- [9] T. Bielmeier, „Wasserstoffmobilität – Marktentwicklungsaktivitäten Weltweit,“ in *14. Symposium Energieinnovation*, 10.-12.02.2016, Graz, Austria, 2016.
- [10] B. Zohuri, *Hydrogen Energy: Challenges and Solutions for a Cleaner Future*, Cham, Switzerland: Springer International Publishing AG, 2019.
- [11] „Realising the Hydrogen Economy,“ MEED Media FZ LLC., 11 10 2019. [Online]. Available: <https://www.power-technology.com/comment/standing-at-the-precipice-of-the-hydrogen-economy/>. [Zugriff am 17 03 2020].
- [12] M. Sartory, M. Justl, P. Salman, A. Trattner, M. Klell and E. Wahlmüller, „Modular Concept of a Cost-Effective and Efficient On-Site Hydrogen Production Solution,“ in *WCX™ 17: SAE World Congress Experience*, SAE International, USA, 2017.
- [13] A. Otto, M. Robinius, T. Grube, S. Schiebahn, A. Praktiknjo and D. Stolten, „Power-to-Steel: Reducing CO2 through the Integration of Renewable Energy and Hydrogen into the German Steel Industry,“ MDPI Publishing, Basel, Switzerland, 2017.
- [14] J. Töpler and J. Lehmann, *Hydrogen and Fuel Cell: Technologies and Market Perspectives*, Berlin: Springer Berlin-Heidelberg, 2016.

- [15] R. Kothari, D. Buddhi and R. Sawhney, „Comparison of environmental and economic aspects of various hydrogen production methods,“ in *Renewable and Sustainable Energy Reviews, Volume 12, Issue 2, 02/2008, p553-563;*, Devi Ahilya University, Indore, India, 2008.
- [16] M. Striednig, *Thermodynamische Analyse eines Betankungsprozess mit Druckgas*, Graz: Technische Universität Graz, 2013.
- [17] P. Ghosh, B. Emonts, H. Janßen, J. Mergel and D. Stolten, „Ten years of operational experience with a hydrogen-based renewable energy supply system,“ *Solar Energy*, Nr. 75, p. 469–478, 2003.
- [18] A. Léon, *Hydrogen Technology: Mobile and Portable Applications*, Berlin: Springer Heidelberg-Berlin, 2008.
- [19] A. Züttel and L. Schlapbach, „Hydrogen-storage materials for mobile applications,“ *Nature* 414(6861), pp. 353-358, 01 2001.
- [20] A. Heller, „llnl.com,“ Lawrence Livermore National Laboratory, 03 12 2008. [Online]. Available: <https://web.archive.org/web/20081203082104/https://www.llnl.gov/str/June07/Aceves.html>. [Zugriff am 2020 04 06].
- [21] „HyGear expands its hydrogen trailer fleet in Europe,“ HyGear Technology & Services B.V., 05 07 2019. [Online]. Available: <https://hygear.com/news/hygear-expands-its-hydrogen-trailer-fleet-in-europe/>. [Zugriff am 2020 03 29].
- [22] M. M. U. Fowler and K. P., „Power-to-gas to produce hydrogen enriched and renewable natural gas for energy storage in the southeastern United States,“ University of Alabama, Huntsville, Alabama, USA, 2017.
- [23] E. M. department, E.ON SE, 24 07 2019. [Online]. Available: <https://www.eon.com/en/about-us/media/press-release/2019/hydrogen-levels-in-german-gas-distribution-system-to-be-raised-to-20-percent-for-the-first-time.html>. [Zugriff am 22 03 2020].
- [24] J. F. Lučko and F. Hausser, *Mathematische Modellierung mit MATLAB: Eine praxisorientierte Einführung*, Heidelberg: Spektrum Akademischer Verlag, 2011.
- [25] S. J. Schäfer, „Dynamische Simulation zur thermodynamischen Analyse einer Wasserstofftankstelle,“ Technische Universität München, Munich, Germany, 2018.
- [26] H. D. Baehr and S. Kabelac, *Thermodynamik : Grundlagen und technische Anwendungen*, Berlin: Springer Vieweg, 2016.
- [27] R. J. A. R. A. B. M. G. Silbey, *Physical Chemistry 4th Edition*, New Jersey, USA: John Wiley & Sons, Inc., 2004.
- [28] N. Sakoda, K. Shindo, K. Shinzato, M. Kohno, Y. Takata and M. Fujii, „Review of the Thermodynamic Properties of Hydrogen Based on Existing Equations of State,“ *International Journal of Thermophysics* 31(2), p. 276–296, 2010.

- [29] J. Leachman, J. R. S. Penoncello and E. Lemon, „Fundamental Equations of State for Parahydrogen, Normal Hydrogen, and Orthohydrogen,“ *Journal of Physical and Chemical Reference Data* 38(3), p. 721, 2009.
- [30] B. Younglove, „Thermophysical properties of fluids. I. Argon, ethylene, parahydrogen, nitrogen, nitrogen trifluoride, and oxygen,“ *Journal of Physical and Chemical Reference Data*, 11(1), 1982.
- [31] G. K. M. Gstrein, „[Properties of Hydrogen,“ Institute for Internal Combustion, University of Technology Graz, Graz, Austria, 2004.
- [32] M. B. Atanas Pavlov, „Thermo Fluids - Linde-Hampson cycle,“ SysMo Ltd., 2018. [Online]. Available: <http://platform.sysmoltd.com/ThermoFluids/LiquefactionCycles>. [Zugriff am 2020 04 01].
- [33] P. Stephan, „Einstoffsysteme,“ Springer, Berlin, 2009.
- [34] „fxsolver.com,“ Equanalysis UG, 03 2020. [Online]. Available: <https://www.fxsolver.com/browse/formulas/Darcy+friction+factor+-+Haaland+equation>. [Zugriff am 30 03 2020].
- [35] „Essential Physical Modeling Techniques,“ The MathWorks, Inc., 2020. [Online]. Available: <https://de.mathworks.com/help/phymod/simscape/ug/essential-physical-modeling-techniques.html>. [Zugriff am 29 03 2020].
- [36] VDI-Wärmeatlas 11. Auflage, Düsseldorf: VDI-Gesellschaft Verfahrenstechnik und Chemieingenieurwesen, 2013.
- [37] P. Landolt, „Sonic Conductance for Everyone,“ Fluid Power Journal, 13 09 2015. [Online]. Available: <https://fluidpowerjournal.com/sonic-conductance-for-everyone/>. [Zugriff am 2020 04 03].
- [38] A. Faghri, Y. Zhang and J. Howell, Advanced Heat and Mass Transfer, City of Columbia, Missouri, USA: Global Digital Press, 2010.
- [39] R. Hugo, „Heat Transfer L1 p1 - Three Types of Heat Transfer,“ 07 09 2015. [Online]. Available: <https://www.youtube.com/watch?v=uEZWoi4ySpU>. [Zugriff am 2020 04 03].
- [40] M. Haider, Angewandte Thermodynamik: Skriptum zur Vorlesung, Vienna, Austria: University of Technology Vienna, 2015.
- [41] W. K. J. Polifke, Wärmeübertragung: Grundlagen, analytische und numerische Methoden, Munich, Germany: Pearso Munich, 2009.
- [42] E. D. Rothuizen, Hydrogen Fueling Stations - A Thermodynamic Analysis of Fuelling Hydrogen Vehicles for Personal Transportation, Lyngby, Denmark: Department of Mechanical Engineering, Technical University of Denmark, 2013.
- [43] Society of Automotive Engineers, *Fueling Protocols for Light Duty Gaseous Hydrogen Surface Vehicles*, Warrendale, PA, USA: SAE International, 12/2016.

- [44] N. H. Omdahl, Modeling of a Hydrogen Refueling Station, Trondheim, Norway: Department of Chemical Engineering, Norwegian University of Science and Technology , 2014.
- [45] J. Schneider, „U.S. DOE Webinar: An Introduction to SAE Hydrogen,“ U.S. Department of Energy, Fuel Cell Technologies Office, Washington DC, USA, 2014.
- [46] „Simulink Models,“ The MathWorks Inc., 04 2020. [Online]. Available: <https://de.mathworks.com/help/simulink/slref/simulink-concepts-models.html>. [Zugriff am 07 04 2020].
- [47] R. G. E. Franks, Mathematical Modeling in Chemical Engineering, New York, London, Sydney: John Wiley & Sons Inc., 1967.
- [48] „REFPROP Version 10,“ National Institute of Standard and Technology, 04 2020. [Online]. Available: <https://www.nist.gov/srd/refprop>. [Zugriff am 08 04 2020].
- [49] R. Privat, Jaubert and Jean-Noël, „Some guidelines to build a predictive thermodynamic model,“ in *Global Journal of Physical Chemistry, Volume 1, Issue 2* , École Nationale Supérieure des Industries Chimiques, Nancy, France, 2010.
- [50] K. J. Vidic, „Betankung & Kühlung - Zusammenfassung,“ Linde Hydrogen FuelTech GmbH, Vienna, Austria, 2019.
- [51] DIN 19226-4: Control Theory - Terms and Definitions of Control Systems, Berlin, Germany: German Institute of Standardization, 1994.
- [52] MathWorks Inc., „Compare Solvers,“ 04 2020. [Online]. Available: <https://de.mathworks.com/help/simulink/ug/compare-solvers.html>. [Zugriff am 16 04 2020].
- [53] AB, Ovako, „Material data sheet - Steel grade 34CrMo4,“ Ovako AB, 26 10 2016. [Online]. Available: https://www.google.com/url?sa=t&rct=j&q=&esrc=s&source=web&cd=5&cad=rja&uact=8&ved=2ahUKEwIU8cGJv_zoAhUKrosKHReUAWkQFjAEegQIBRAB&url=https%3A%2F%2Fsteelnavigator.ovako.com%2Fsteel-grades%2F34crmo4%2F&usg=AOvVaw32c4qt6x8bgB_WVm-vXCVI. [Zugriff am 22 04 2020].
- [54] New Mexico Institute of Mining and Technology, „Preparation instructions for a motor control laboratory project,“ Department of Electrical Engineering, NMT, 2013. [Online]. Available: http://www.ee.nmt.edu/~erives/308_13/Lecture24_S13.pdf. [Zugriff am 23 04 2020].
- [55] vivekbose.com, „Introduction to PID Controller With Detailed P,PI,PD & PD Control,“ 04 2020. [Online]. Available: <https://vivekbose.com/introduction-to-pid-controller-with-detailed-ppipd-pd-control>. [Zugriff am 23 04 2020].
- [56] H.-J. Bungartz, M. Buchholz, D. Pflüger and S. Zimmer, Modellbildung und Simulation: Eine anwendungsorientierte Einführung, Heidelberg: Springer Spektrum, 2009.
- [57] A. Jenkins, „Alicat Scientific,“ 2020. [Online]. Available: <https://www.alicat.com/achieving-responsive-and-stable-valve-control-with-pid-tuning/>. [Zugriff am 10 03 2020].

List of figures

Figure 1: Global secondary energy carriers' stakes in 2014 in Mtoe [3].....	1
Figure 2: Global secondary energy consumption between 1995 and 2014 in Mtoe [3].....	2
Figure 3: Observed changes in atmospheric greenhouse since 1750 [8].....	3
Figure 4: Comparison of specific energy versus volumetric density [10].....	5
Figure 5: Hydrogen production pathways from fossil and renewable sources [14].....	10
Figure 6: Gravimetric versus volumetric hydrogen densities of potential storage technologies or bonding partners [19].....	13
Figure 7: Aggregate states of hydrogen, depending on the relationship between density, temperature and pressure [2].....	14
Figure 8: Real gas factor Z of hydrogen, depending on pressure and temperature [2].....	21
Figure 9: T,s-diagram for equilibrium hydrogen for temperatures from 15 to 85 K [2].....	24
Figure 10: Process flow diagram of a basic Linde-Hampson cycle, used e.g. for hydrogen liquefaction [32].....	25
Figure 11: Open non-steady system with heat and work supply and discharge [25].....	27
Figure 12: Influence of various critical pressure ratios on Cv	
Figure 13: Influence of various critical pressure ratios on Cv at constant volumetric flow rates [37] at decreasing volumetric flow rates [37].....	32
Figure 14: Overview of the three major modes of heat transfer, [39].....	33
Figure 15: temperature profile of the heat transfer through a pipe wall [40].....	35
Figure 16: Simple sketch of direct compression fueling [42].....	37
Figure 17: Simple sketch of fueling through the usage of a pressure gradient [42].....	37
Figure 18: Basic process scheme of the commercially established multiple-stack system.....	38
Figure 19: Operating range of an H70-T40 reference parameter scenario [43].....	41
Figure 20: APRR boundaries and the pressure tolerance corridor [43].....	42
Figure 21: Look-Up Table example for the reference case according to SAE J2601 [43].....	43
Figure 22: Process scheme of the signal flow within communications fueling [43].....	43
Figure 23: Procedure scheme for the "Non-Com" case [44].....	44
Figure 24: Course of an APRR within the pressure tolerance corridor and cascade tank-switching events [43].....	46
Figure 25: Fueling pressure gradient versus time of a complete fueling cycle [45].....	47
Figure 26: Example of a physical component model of a basic gas system on the Slmscape GUI.....	51
Figure 27: Vector field of c_p as a function of pressure and temperature.....	52
Figure 28: Global GUI's view on the hydrogen fueling station's model.....	54
Figure 29: List of available domains and its assigned line styles.....	55
Figure 30: Cascade storage tanks, check valve, gate valve, gas properties block and solver configurations element, structured within the model's expectable flow direction.....	56
Figure 31: Sketch of an "ACF" unit [50].....	57
Figure 32: Pipe section "bank control", pipe section "dispenser line", pressure controller, heat exchanger and pipe section "dispenser" in the model's correct downstream flow direction.....	57
Figure 33: The "Mass & Energy flow rate sensor", "Pressure & temperature sensor" and "Thermodynamc properties sensor", concluding the gas flow unit together with the vehicle tank.....	58

Figure 34: Thermal port connects cascade storage tank 1 with the tank's heat transfer subsystem	58
Figure 35: Physical component model of the heat transfer between hydrogen of cascade storage tank 1, the tank's material layers and the ambient air	58
Figure 36: Central block elements of the control unit	60
Figure 37: Snapshot of the PID controller block's input window	61
Figure 38: Pressure controller and the conversion of the measured pressure-gradient into a Simulink feedback signal	62
Figure 39: Upper and lower pressure tolerance boundaries generated inside the yellow encircled subsystems of this unit's snapshot	63
Figure 40: Middle part of unit „tank switching mechanism“ and its logic block subsystems in an expanded pop-up view	63
Figure 41: The "switch case" block, transmitting integers in case of a match between input signal and its inherent "case" values	64
Figure 42: Close-up of a Set-Reset flip-flop and a corresponding assignment of an output integer value 1 with sustained "tilting stability"	66
Figure 43: Solver selection process of the "auto solver" method.....	68
Figure 44: Snapshot of the MatLab input window, providing initial values for the following Simscape simulation	69
Figure 45: An applicable MatLab code example for retrieving and printing an array of mass flow data inside MatLab	70
Figure 46: The corresponding cell array, containing the mass flow data	70
Figure 47: Positioning of the four working points inside the basic process scheme	71
Figure 48: Pressure levels of an H70-T40 non-com fueling procedure, utilizing three cascade storage tanks.....	73
Figure 49: Display of the tank switching mechanism's late actuation, resulting in high exploitation rates of the pressure gradient.....	73
Figure 50: Temperature development, simulated at the cascade tank outlets, and the inside of the vehicle tank	74
Figure 50: Progress of mass flow rate for an H70-T40 fueling and 5MPa initial vehicle tank pressure, using three cascade tanks	75
Figure 51: Density gradients, simulated inside of cascade tanks and the vehicle tank (initial pressure: 5 MPa).....	76
Figure 53: Convective heat flow rates between hydrogen flow and the components' innermost layers	77
Figure 54: Conductive heat flow rate through the components' steel or carbon fiber layers	78
Figure 55: Convective heat flow rates between outermost components' material layers and the environment.....	78
Figure 56: Conductive and convective heat flow rates through the material layers of the heat exchanger	79
Figure 57: Temperatures at the inlet, outlet and center of heat exchanger block.....	80
Figure 58: Temperatures inside of heat exchanger and pipe sections "dispenser line" and "dispenser"	81
Figure 59: Snapshot of the Simscape input mask of the ACF's "thermal mass" block for the aluminum layer	81
Figure 60: Model of the heat exchanger's "thermal domain" subsystem, showing the "target cooling temperature" block as the source of cooling supply	82

Figure 61: Temperatures at the inlet and outlet of pressure controller, together with inner vehicle tank temperature	82
Figure 62: Pressure at the inlet and outlet of pressure controller, together with inner vehicle tank temperature	83
Figure 63: Pressure levels of an H70-T40 non-com fueling procedure, utilizing three cascade storage tanks and an initial vehicle tank pressure of 40 MPa	85
Figure 64: Temperature development, simulated at the cascade tank outlets, and the inside of the vehicle tank	86
Figure 65: Progress of mass flow rate for an H70-T40 fueling and 40 MPa initial vehicle tank pressure, using three cascade tanks	87
Figure 66: Density gradients, simulated inside of cascade tanks and the vehicle tank (initial pressure: 40 MPa)	87
Figure 67: Convective heat flow rates between hydrogen flow and the components' innermost layers	88
Figure 68: Conductive heat flow rate through the components' steel or carbon fiber layers.....	89
Figure 69: Convective heat flow rates between outermost components' material layers and the environment.....	89
Figure 70: Conductive and convective heat flow rates through the material layers of the heat exchanger	90
Figure 71: Temperatures at the inlet, outlet and center of heat exchanger block.....	91
Figure 72: Temperatures inside of heat exchanger and pipe sections "dispenser line" and "dispenser"	91
Figure 73: Temperatures at the inlet, the actuating orifice diameter and the outlet of pressure controller.....	92
Figure 74: Pressure at the inlet and outlet of pressure controller, together with inner vehicle tank temperature for scenario 2	93
Figure 75: SOC percentages for fueling scenario 1 and 2.....	94
Figure 76: Pressure profiles of the cascade tanks and the vehicle tank in case of an outage of the heat exchanger	96
Figure 77: Temperature profiles of the inlet and outlet of the pressure controller, and the vehicle tank in case of an outage of the heat exchanger	96
Figure 78: Density profiles of the cascade tanks and the vehicle tank in case of an outage of the heat exchanger	97
Figure 79: Block positive direction of a "convective heat transfer" block	97
Figure 80: Convective heat flow rates between hydrogen flow and the components' innermost layers – case 1, outage of heat exchanger	98
Figure 81: Convective heat flow rates between hydrogen flow and the components' innermost layers – fueling scenario 1, heat exchanger supplies cooling power.....	98
Figure 81: Pressure profiles at the outlets of the cascade tanks, and the inside of the vehicle tank in case of a change of the control parameters	100
Figure 82: Temperature profiles at the outlets of the cascade tanks, and the inside of the vehicle tank in case of a change of the control parameters.....	101

List of tables

Table 1: Fuel delivery temperature categories per pressure classes 40
Table 2: List of utilized Simcape and Simulink block components 53
Table 3: Labelling the basic elements of the control unit according to DIN 19226-4 [51]..... 60
Table 4: Typical initial values of a passenger car fueling scenario 72
Table 5: Thermal conductivity coefficients applied for the material layers of the model 82
Table 6: Initial values of fueling scenario 2 85

Die approbierte gedruckte Originalversion dieser Diplomarbeit ist an der TU Wien Bibliothek verfügbar
The approved original version of this thesis is available in print at TU Wien Bibliothek.

